Low Cost Earth Sensor Based on Oxygen Airglow (AIRES)

D8 – Final Report

June 2008

Prepared by:

N. Scheidegger – EPFL- LMTS

H. Shea – EPFL - LMTS

E. Charbon – EPFL - LAP

E. Rugi-Grond – Oerlikon Space

- EPFL
Lausanne
Switzerland
- 29/08/2008
-

Record of revisions

ISS/REV	Date	Modifications	Created/modified by
1/0	20.02.2008	Initial Issue	EPFL-STI/IMM/LMTS
1/1	29.02.2008	Updated Document according to comments of ESA done at the FR	EPFL-STI/IMM/LMTS
1/2	5.05.2008	Simplified version of SPAD design section	EPFL-IC/LAP/AQUA
1/3	9.05.2008	Update to reflect comments from S. Airey prior to Final Review	EPFL-IC/LAP/AQUA
1/4	20.05.2008	Update to reflect comments from S. Airey at Final Review	EPFL-STI/IMT/LMTS
1/5	13.06.2008	Proton Testing Update	EPFL-IC/LAP/AQUA

CONTENTS

References

[1]   N. Scheidegger et al., "Earth Appearance Model at 762 nm", output of WP 1200 of the ESTEC Contract No 20267/06/NL/JA, 2007

[2]   "Statement of Work – Earth Sensing for FDIR Feasibility Assessment", ESA/TEC-ECC/104/2006

[3]   N. Scheidegger et al., "D2 – Filter Requirements", output of WP 1300 of the ESTEC Contract No 20267/06/NL/JA, 2007

[4]   Dr. E. Gubbini et al., "ES Study Preliminary Objectives Design", output of WP 1200 of the ESTEC Contract No 20267/06/NL/JA, 2007

[5]   L. Carrara et al., "D1- SPAD Design Repot" output of WP 1100 of the ESTEC Contract No 20267/06/NL/JA, 2007

[6]   N. Scheidegger et al., "D3 - Earth Vector Algorithm Design Report", output of WP 1200 and WP 4000 of the ESTEC Contract No 20267/06/NL/JA, 2008

[7]   R.G.H. Greer et al., "ETON 1: A data base pertinent to the study of energy transfer in the oxygen nightglow", Planet. Space Sci, 34: p. 771, 1986

[8]   Physics of the Aurora : Earth systems, http://meted.ucar.edu/hao/aurora/txt/x_menu.php, September 2006

[9]   The WINDII Science Page: http://www.windii.yorku.ca/science/science.html, September 2006

[10] C. McDade et al., "ETON 2: Quenching parameters for the proposed precursors of $O2(b1\sum g+)$ and $O(1S)$ in the terrestrial nightglow", Planet. Space Sci, 34: p. 789, 1986

[11] G.G. Shepherd, Y.-M. Cho, G. Liu, M.G. Shepherd, R.G. Roble, "Airglow variability in the context of the global mesospheric circulation", J. atmos. solar-terr. Phys., 2006

[12] H.R. Shea, "Reliability of MEMS (microsystems) for space applications", European Space Agency, (Special Publication) ESA SP (591), pp. 17-24., 2005

[13] H.R. Shea, "Reliability of MEMS for space applications", Proc. SPIE Int. Soc. Opt. Eng. 6111, 61110A, 2006

[14] H.R. Shea et al., "Effects of Electrical Leakage Currents on MEMS Reliability and Performance", IEEE Transactions on Device and Materials Reliability, Vol. 4, No. 2, p.198, 2004

[15] C. Niclass, M. Sergio, E. Charbon, "A Single Photon Avalanche Diode Array Fabricated on Deep-Submicron CMOS Technology", Design and Test in Europe (DATE), Mar. 2006.

[16] C Niclass, C. Favi, T. Kluter, M. Gersbach, E. Charbon, "A 128x128 Single-Photon Imager with on-Chip Column-Level 10b Time-to-Digital Converter Array Capable of 97ps Resolution", IEEE International Solid-State Circuits Conference (ISSCC), San Francisco, pp. 44-45, Feb. 2008.

[17] C Niclass, C. Favi, T. Kluter, M. Gersbach, E. Charbon, "A 128x128 Single-Photon Imager with on-Chip Column-Level 10b Time-to-Digital Converter Array", subm. IEEE Journal of Solid-State Circuits, April 25th, 2008.

1 ABSTRACT

This project has demonstrated the feasibility of a low-cost Earth sensor based on imaging oxygen airglow, allowing 0.4° accuracy from GEO under any illumination condition.

Available Earth Sensor (ES) are based on the measurement of the earth's infrared radiation to determine the vector to the Earth's centre. These designs provide excellent accuracies over a large field of view, but are often heavy, large, require cooling or temperature stabilization and are power hungry. In addition, the sensor concept for a LEO or GEO application ES differs significantly.

We have developed a novel ES concept for applications where milli-degree accuracy is not required, but where low-cost is essential and lower (about $1 - 5°$) accuracy is acceptable. Such a sensor could be used in new scenarios and to improve spacecraft reliability by providing a low-cost back-up sensor.

Our Earth Sensor concept is based on imaging atmospheric oxygen emission at 762 nm using highly sensitive detectors. In both night-time and daytime there is continuous emission at 762 nm due to oxygen recombination. Low-noise active pixel sensors (APS) or low-light detector based on arrays of single photon avalanche diodes (SPAD) enables the ES to operate at night and day, over a wide temperature range, with a very compact optical system (aperture of 8 mm, focal length of 11 mm) and no scanning elements. A modular design allows designing similar instruments using the same wavelength band, the same detector technology, the same optics, the same power and data interfaces and similar algorithms for GEO and LEO applications, thus reducing the development cost.

We have developed an Earth appearance model at 762 nm, which was used as input for the mechanical, optical and electric design of the Earth Sensor (conceptual design). In order to achieve a low-cost solution, simplicity and reduction of part count was a driving factor in the design trade-offs. Total mass for the GEO design is 845 g with a mean power consumption of 4 W. Algorithms were developed to determine the vector to the Earth from the images. A breadboard was built to display a simulated picture of the Earth under varying conditions, image those pictures at different temperatures with a radiation tolerant APS (LCMS), and verify the correct operation of the algorithms.

In addition to the conceptual design and breadboard level demonstration of key technologies, a novel detector chip was designed and fabricated: a radiation-tolerant array of single photon avalanche photodiodes (SPAD) build using conventional 0.35 μm CMOS technology. The chip was tested under proton and gamma irradiation, and operated with only minor changes in dark current after 30 krad TID.

Having shown the feasibility of such an Earth Sensor, this work concluded with a development plan to lead to a flight model.

2 INTRODUCTION

2.1 Scope

This document presents the work performed by the Microsystems for Space Technologies Laboratory (LMTS) at the EPFL and its subcontractors under ESA contract No 20267/06/NL/JA.

After a brief presentation of the project objectives and its management in chapter 2 and 3, the Earth Appearance Model is presented in chapter 4. The overall design of the AIRES earth sensor including its mechanical, optical, electrical design, as well as a detailed description of the Single Photon Avalanche Diodes (SPADs) and the earth vector algorithm are explained in chapter 5. A summary of all mass and power budgets is given in chapter 6, and chapter 7 concludes with the strategy for design, selection of components, manufacturing and verification, which shall lead to a Flight Model (FM) of the earth sensor.

2.2 Objectives

Low cost earth sensors currently do not exist on the market due to the lack of a suitable sensing concept. Their availability would allow earth sensors to be used in new scenarios and to improve system reliability by providing a low-cost back-up sensor which could be used for applications where neither milli-degree accuracy nor operation at high angular rates are required, but where low-cost is essential and lower (about $1 - 5°$) accuracy is acceptable.

The objectives of this project were to demonstrate the feasibility and reliability of using low cost detectors to sense the atomic oxygen airglow of the atmosphere from space and estimate the performance of a low cost earth sensor that uses this concept. A breadboard has been designed, manufactured and tested to confirm that this concept is viable.

2.3 Team

The team for the AIRES project is presented in TABLE 1, with a description of the function of each team member within this activity.

TABLE 1: AIRES PROJECT TEAM

Name	Company	Function within Project
H. Shea	EPFL-LMTS	Project management, breadboard design
N. Scheidegger	EPFL-LMTS	ES concept design, Earth Appearance Model, algorithm development, definition of filter requirements, breadboard test plan and testing
E. Rugi-Grond	Oerlikon Space	Project management for ES optics, development plan
E. Gubbini	Oerlikon Space	ES optics, filter design

Th. Weigel	Oerlikon Space	ES optics, filter design
E. Charbon	EPFL-AQUA	SPAD project management
L. Carrara	EPFL-AQUA	SPAD design and layout, SPAD testbed and electronics, SPAD testing

2.4   Background

2.4.1   Ecole Polytechnique Fédérale de Lausanne (EPFL)

2.4.1.1   EPFL description

The EPFL is one the leading engineering universities in Europe. Located in Lausanne, Switzerland it is listed among top-ten universities in Europe in all major rankings.

With an annual budget of over 400 million Swiss francs, it employs over 3,200 scientists and technicians with seven faculties and over 250 professors. The EPFL has as long track record of successful collaboration with the space industry, and has very broad experience in materials, electronics, mechanisms, solar cells, antennas and communication, and electro-optical systems.

Figure 1. Aerial view of the EPFL campus in Lausanne, Switzerland.

2.4.1.2   EPFL organization

The chart below (Figure 2) provides an overview of the organisation with the EPFL, and highlights the laboratory (LMTS) leading in this proposal and the laboratory (AQUA) developing the SPAD arrays.
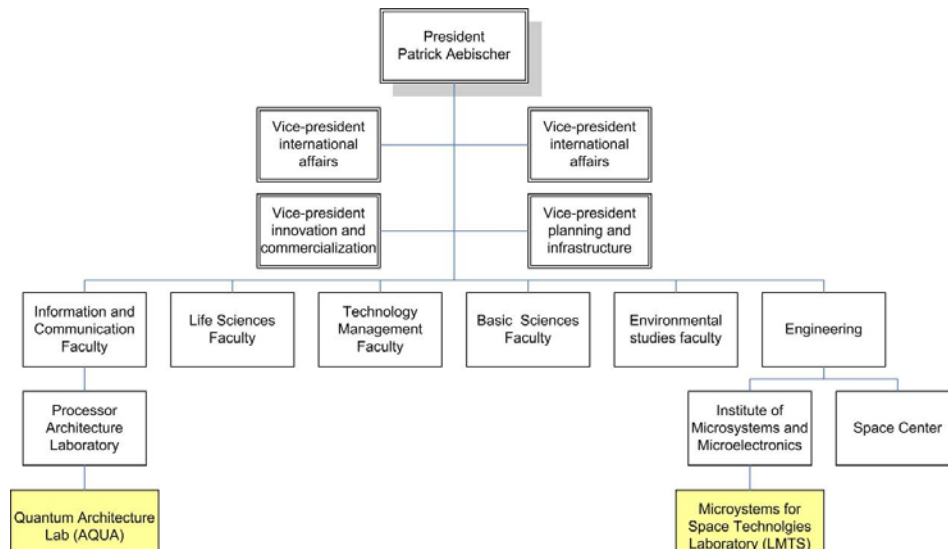
Figure 2: EPFL organisation.

2.4.1.3   Experience within EPFL

The EPFL has specific expertise in Microsystems (MEMS) with over 7 laboratories dedicated to Microsystems research, a dedicated center for microscopy, and a world-class clean-room dedicated to MEMS.

Through its many research activities in a broad range of domains such as engineering, material science, physics, chemistry, computer science the EPFL offers an unparalleled wide range of knowledge and in-depth understanding of MEMS technologies and analysis required to determine the radiation sensitivity of MEMS.

Microsystems for Space Technologies Laboratory (EPFL-LMTS)

The Microsystems for Space Technologies Laboratory (EPFL-LMTS) was founded in 2004 by Prof. H. Shea, previously with Bell Labs, Lucent Technologies where he led a group developing ultra-reliable microsystems and MOEMS-based optical switches (for example the ultra-stable zero-drift mirror shown in Figure 5).

The LMTS focuses on designing microsystems that can operate reliably while fulfilling the stringent requirements imposed on space borne instruments and systems. The motivation being to lower the cost of satellites while increasing their performance using micromachining technology.

Prof. Herbert Shea is a world renowned expert in MEMS reliability, with several publications in the field of Reliability of MEMS for Space [12] and [13], and on the effect of dielectric charging on electrostatic MEMS reliability and failures [14]. The staff in the LMTS combined decades of experience in microsystems design, fabrication, characterization, and analysis.

EPFL-LMTS activities

Ion propulsion based on array of microfabricated capillaries (10 µm diameter) with integrated extraction and acceleration electrode, using ionic liquids as propellants for high ISP thrusters.	**Figure 3: Micro-capillary arrays for ion propulsion.**
The LMTS is developing novel 'artificial muscle' type micro-actuators for space applications. These devices are microfabricated using ion-implanted polymers, and couple extremely high energy density with large percentage displacement.	**Figure 4: FEM model and micrograph of EAP actuators.**
EU-project e-CUBEs, in collaboration with ESA (Advanced Concepts Group) to develop mm^3 wireless sensor networks for space exploration, using microsystems technology	
The LMTS and the EPFL Space Center are leading the development of a university 1 kg nano-satellite (SwissCube), for launch in 2009. This satellite will observe nightglow and serves as rapid way to demonstrate the validity of novel technologies.	
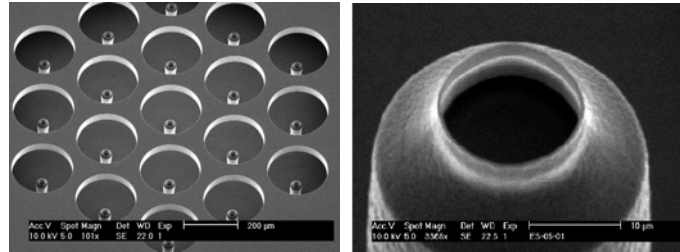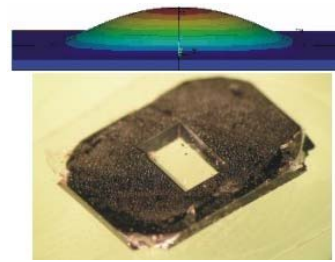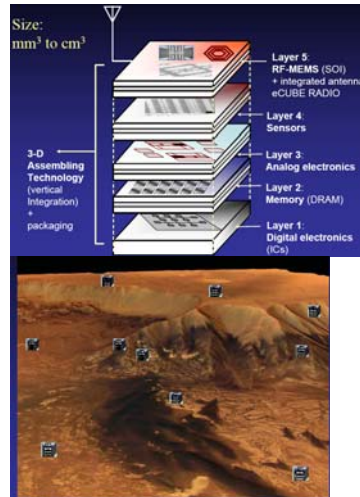
The LMTS signed contract # 19531 with ESA to develop a large port count MOEMS-based optical switch. The prime contractor is with Sercalo Microtechnology, other partners are the University of Neuchatel and Alcatel Space. The LMTS is responsible for MOEMS characterization drift control, and overall reliability.
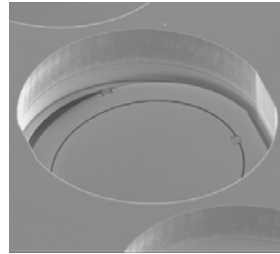
Figure 5: SOI MOEMS mirror co-developed by head of EPFL-LMTS while at Lucent Technologies. Similar drift-free (no exposed dielectric) design are being developed for ESA by IMT, Sercalo Microtechnology, and EPFL.

Quantum Architecture Group (EPFL-AQUA)

The Quantum Architecture Group (EPFL-AQUA), situated within the Processor Architecture Laboratory (LAP) at the EPFL's School of Computer & Communication Sciences, has as research mission to model and develop hardware/software systems based on quantum devices. It pursues two main research directions around the central theme of *CMOS quantum architectures*. The first relates to the modelling and design of low power, high performance 2D/3D imagers and detectors based on Single Photon Avalanche Diodes (SPADs) and other quantum devices. The second focuses on analysis algorithms and automation methodologies for the design of these imagers and of embedded computational/arithmetic units associated with them.

The EPFL-AQUA has developed highly sensitive arrays of Single Photon Avalanche Diodes (SPADs), and has built 3D cameras using these detectors to determine the time of flight of photons at each pixel. This 3D imager is capable of capturing the depth map of an arbitrary scene by means of a low-cost pulsed laser. The depth measurement is based on time-of-flight and it is performed independently in each pixel using a CMOS time-to-digital-converter (TDC). To reach millimetric accuracies an array of highly sensitive, ultra-low jitter single photon detectors and picosecond resolution TDCs have been integrated in CMOS technology. Since the scene is illuminated all at once by a cone of low power pulsed laser light, no mechanical scanning devices or expensive optical equipment are required.

This novel, yet low-cost detector technology, as well as the relevant algorithms, is directly applicable to this earth sensor study.
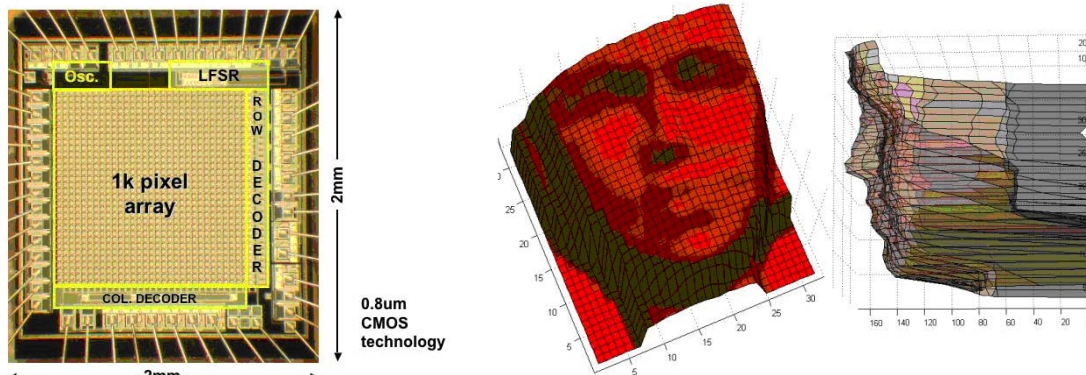
Figure 6: Imaging chip of single photon counters developed at the EPFL (left) and 3D reconstruction of a face using such a chip and time-of-flight techniques (right).

AQUA's researchers have been at the forefront in recent SPAD developments, that include scalable, massively parallel SPAD arrays and the migration of the technology to sub-micron and, most recently, deep submicron technologies. The advances achieved by the AQUA group are recognized as among the most successful in the current international effort to advance single photon detector technology. The competition includes MIT, Columbia University, Politecnico di Milano, University of Edinburgh, Cork University, etc.

The AQUA group has a clear roadmap for the future and a proven track record for the past, since the introduction of the first chip in 2003. Figure 7 shows the major steps in our roadmap that have always established a record at the time of publication. As an example, the design presented in [15] was awarded the record paper status at DATE (Design, Automation and Test in Europe Conference) in 2006.

We are continuing this trend in 2007 with the next-generation SPAD technology that will include the largest SPAD array ever reported and the first implementation of SPADs in 130nm. At the same time we are continuing our effort in ultra-low-power high-performance multi-processors that will provide the necessary processing power for a number of demanding imaging sensors in both time-correlated and high capture speed domains.
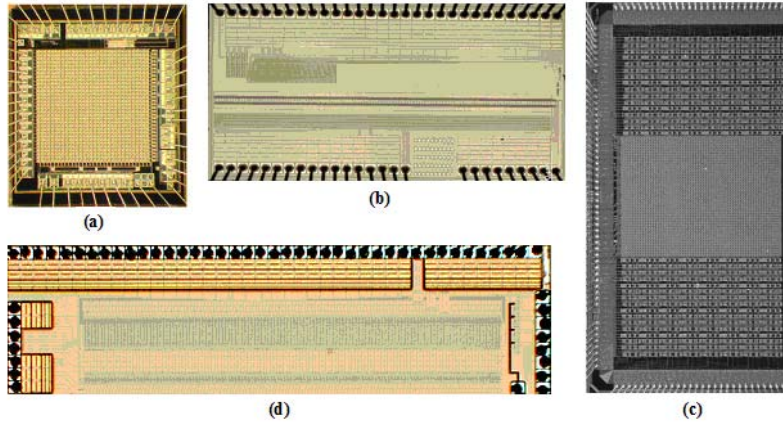
Figure 7: SPAD milestones at AQUA: a) 1st generation sensor with random access readout realized in 0.8μm CMOS technology; b,c) 2nd generation sensors realized in 0.8 and 0.35μm CMOS with event-driven readout technology; d) 3rd generation sensor with simultaneous readout.

2.4.2   Oerlikon Space

2.4.2.1   Oerlikon Space (OSZ) Company Description

Oerlikon Space is a company within the Oerlikon Group (see Figure 8) with more than 30 years of experience in the Space business in general and in particular in the design, manufacturing, testing and integration of spacecraft structures and complex systems. As a result of its broad experience, OSZ is an acknowledged leader in this field within the European Space community.

| **Figure 8: Oerlikon Group.** | **Figure 9: Oerlikon Space Premises.** |

OSZ continuously invests not only in new products but also in new or improved processes, manufacturing techniques and quality control procedures in order to ensure that it can continue to offer to its valued Customers reliable solutions at competitive conditions. Additionally, recognising the increasingly demanding programmatic constraints, OSZ has developed and refined its approach to project management and project implementation. The implementation of our projects and the relation with our Customers are geared toward problem solving and are based on our objective and fair as well as long-term partnership.

Registered name: Oerlikon Space AG
Registered address: Schaffhauserstrasse 580, CH 8052 Zürich
Registration Date: November 9, 1999
Number of employees: 320
Mailing Address: Schaffhauserstrasse 580, CH-8052 Zurich
Phone / Fax No.:   +41-1-306 2211 / +41-1-306 2910
Chief Executive Officer: Dr. Deich
Legal status: Private Limited Company

2.4.2.2   OSZ Company Organisation

The chart shown below (Figure 10) provides a general overview of the organisation within Oerlikon Space AG down to the Project Manager.
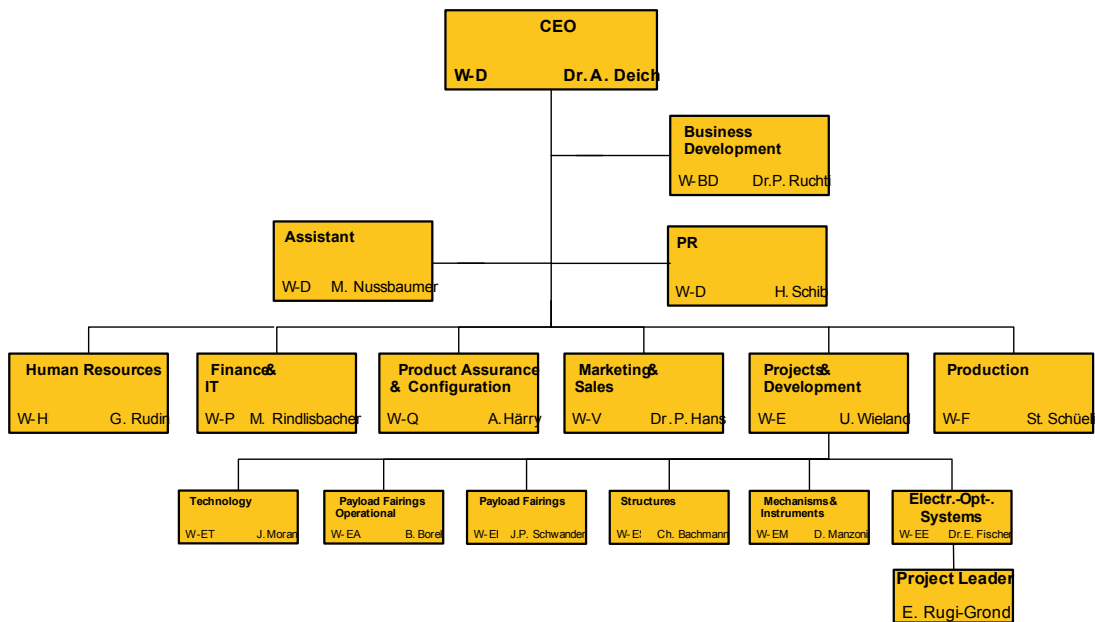
Figure 10: Oerlikon Space Organisation.

The entry of Oerlikon Space in the field of space technology dates back to 1964 when the European Space Research Organisation ESRO commissioned Oerlikon Space AG (former Contraves Space) to develop and build the structure, mechanisms and thermal control subsystem for their first scientific spacecraft ESRO-1. This contract marked the beginning of a continuous and successful evolution to what is currently the largest space company in Switzerland. Since then, Oerlikon Space has contributed to many missions for space in the fields of payload fairings, satellite structures and mechanisms and instruments for scientific research. The following section describes in more detail the company heritage specifically related to the low cost earth sensor project.

2.4.2.3   Experience within OSZ

OS entered into the field of mechanisms and electro-optical systems, including laser technology, more than two decades ago and has gained extensive experience within this domain. This experience has led to a world leading position in the development of the advanced optical terminals for satellite communication links. This position has been gained from the following ESA projects:

-   Short Range Optical Inter-Satellite Link demonstrator (SROIL) project.
-   Inter-Satellite Link Front-End (ISLFE) project.
-   Optical Crosslink (OXL) project.
-   Alp-Sat, consultancy contract
-   OGS, study of optical deep space communication application

In addition to its participation in projects dealing with instruments and structures for spacecraft's, OSZ has demonstrated its competence in the past and is currently working on several projects involving the engineering of electro-optical systems, such as:

-   MIPAS calibration system for ENVISAT1
-   IASI scan units for METOP
-   Electric Propulsion Thruster Orientation Mechanism for SMART1
-   Alignment TV cameras
-   Infrared Search and Tracking System
-   PRN Lidar
-   Star-Sensor Optics and Structure
-   Optical Ground Station Consultancy for OGS on Tenerife
-   High Stability Light Source (pump laser)
-   Core laser technology development

The OSZ team has in-depth systems engineering knowledge on electro-optical systems that is applicable to this project and retains the technical and technology base of key hardware. OSZ also has the managerial experience, the necessary skills and knowledge to complete this project within the technical requirements, financial targets and schedule limitations.

3 PROJECT MANAGEMENT

3.1 Structure

The project was divided in two main phases and several work packages as shown in Figure 11 and Figure 12. The EPFL was responsible for project management and coordination, earth sensor concept (except the optics), SPADs, and breadboard (except the optics). Oerlikon Space was responsible for the optics of the breadboard and the earth sensor, filter feasibility and performance, and development plan.

The work breakdown structure (WBS) shown in Figure 11 provided a systematic division of work and tasks related to the identified products, documents and services. It assisted the planning, monitoring of technical events, schedule control, collection and summarisation of project management information as well as evaluation of proposal changes.
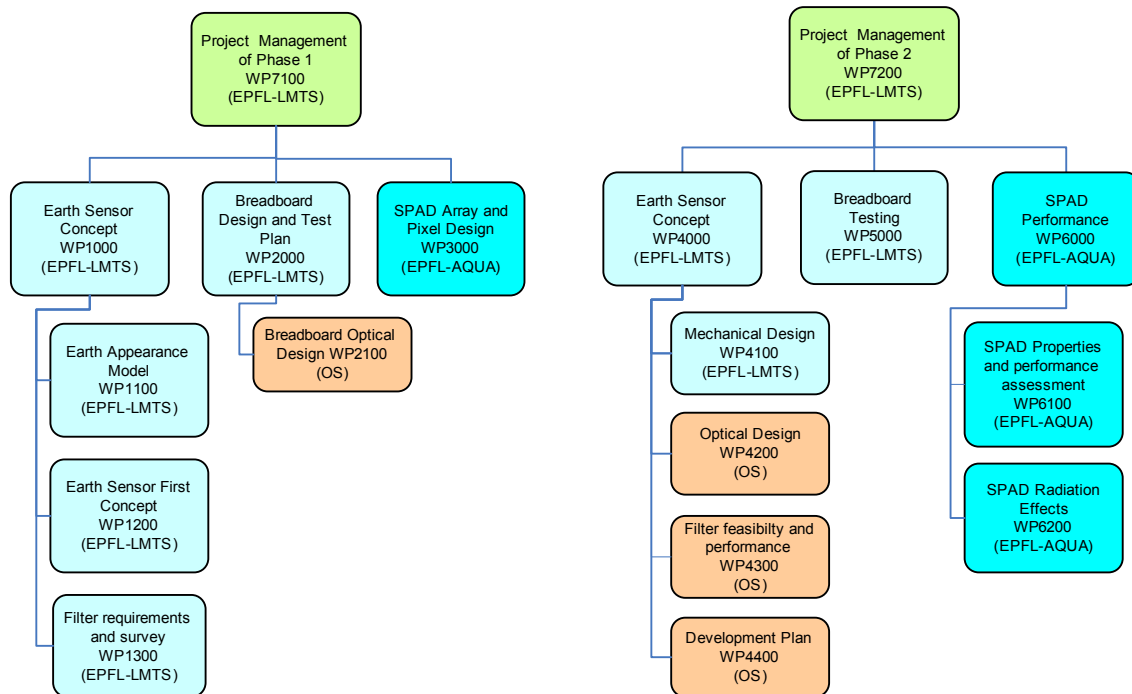
Figure 11: Work Breakdown Structure, showing WP titles and WP leaders.

Kick-off

Phase 1

WP 1100: Earth Appearance model
2 months

Develop Earth appearance model at night and day at oxygen line wavelenth from atmospheric oxygen, sunlight, moonlight, auroras, and man-made sources

WP 1200: Earth Sensor 1st Concept
3 months

Develop a first Design for an Earth Sensor based on Oxygen lines and SPADs

Derive Filter Requirements and perform Survey of existing solutions

WP 1300: Filter - 3 months

Design Breadboard and test plan

WP 2000: breadboard definition - 3 months

SPADs:
- Architectural design of array
- Pixel design
- Order test array

WP 3000: SPADs - 3 month

Mid Term Review

Phase 2

Develop Earth Sensor Concept:
- Algorithms
- Mechanical design
- Optical design
- Electronic design

WP 4100, 4200 & 4300: Earth Sensor Concept Design - 7 months

Build breadboard, and use it to validate the concept

WP 5000: Breadboard build and test - 7 months

SPAD:
- define Electrical design
- describe Electro-optical properties and models

WP 6100: SPAD Performance - 3 months

SPAD:
- radiation testing

WP 6200: SPAD Radiation tests - 4 months

Define development plan

WP 4500: Development Plan- 2 months

Final Review

Final Report

Figure 12: Study logic.

3.2   Schedule

The project kick-off was on 13.10.2006 and ended on June 30th 2008. The following table gives an overview of the scheduling of the main events:

TABLE 2: SCHEDULE OF THE AIRES PROJECT

Detector	Meeting	Purpose	Original Date	Actual Date
KOM	Kick Off Meeting	Requirement clarification,		13/10/2006

		contact negotiation and signature		
MTR	Mid Term Review	Presentation of study, preliminary conclusion	06/2007	13/07/2007
FR	Final Review	Presentation of study, preliminary conclusion	03/2008	29/02/2008
FP	Final Presentation	Presentation of project results	04/2008	30/6/2008

The main problems arising during the project were:

- The first version of the SPAD chips (RADHARD) was delivered with a delay of 40 days and could not be operated due to a mask error. A new version of the SPAD chips had to be designed. The second version of the SPAD array (RADHARD2) was designed and taped out in November 2007.

- Since the SPAD chip (RADHARD) was not ready in time for the planned algorithm tests, an alternative detector (LCMS) was used for most of the algorithm testing.

- Packaging and interfacing of the RADHARD2 chip took more time than expected. Radiation testing, performed in two phases (Co60 and Proton), was completed in March and May 2008, respectively.

Figure 13 shows the schedule of the project. The red bars are the original schedule, whereas the blue bars are the final schedule.

Low Cost Earth Sensor based on Oxygen
Airglow – Final Report
ESA Contract #20267/06/NL/JA
Issue: 1   Review: 5
Date: 29/08/08
Page: 19 of 88

Figure 13: Schedule (Gantt)

Low Cost Earth Sensor based on Oxygen
Airglow – Final Report

ESA Contract #20267/06/NL/JA
Issue: 1   Review: 5
Date: 29/08/08
Page: 20 of 88

4   EARTH MODEL

4.1   Airglow Emissions

4.1.1   Spectrum of Airglow Emissions
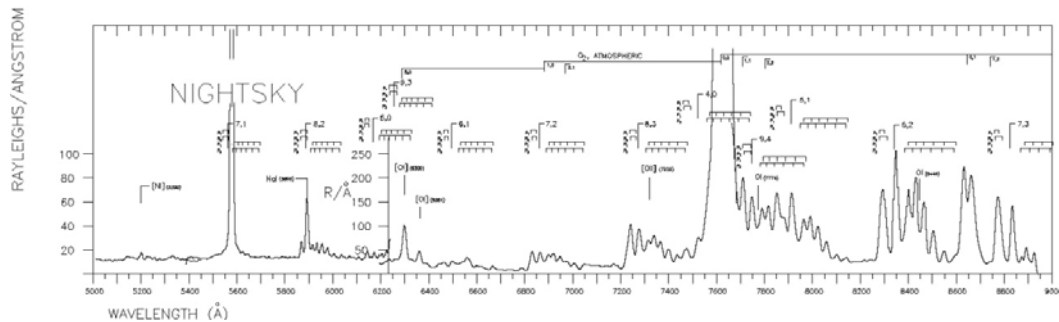
Figure 14: Limb measure of nightglow.
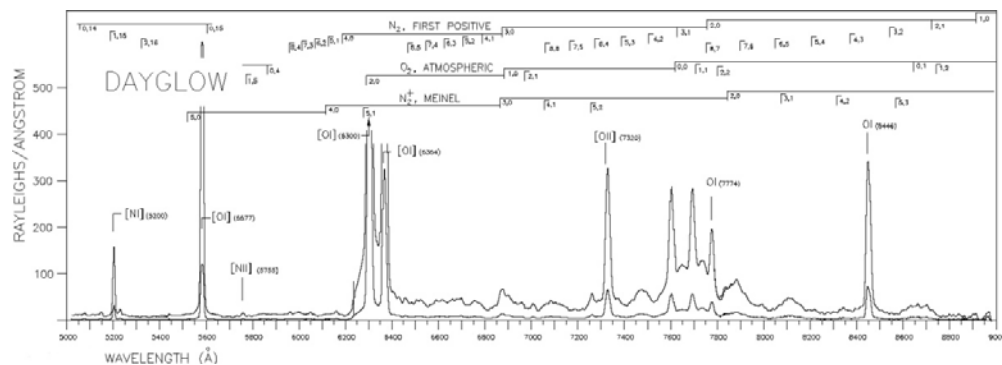
Figure 15: Limb measure of dayglow.

Atmospheric emissions in the wavelength band from 500 to 900 nm can be classified as: nightglow, dayglow and aurora. Although night- and dayglow are less luminous than an aurora, they are the only potential candidates for detection by an earth sensor because of their permanence. Figure 14 and Figure 15 show the airglow nighttime and daytime spectra between 500 and 900 nm. Emission is measured in Rayleighs [R] at limb. The most prominent feature, visible from earth, is the atomic oxygen O (^{1}S) green line at 557.7 nm, whereas the strongest airglow band, only visible from space, is the O_2(0-0) A-band at 762 nm. For these two wavelengths, aurora and dayglow originate from photodissociation, photo-excitation and excitation by fast electrons or ion recombination. The origin of the nightglow is oxygen atom recombination, where the oxygen atoms are created in the daytime by solar photodissociation of O_2 [10].

A number of studies exist on the temporal and latitudinal variability in the oxygen emissions in the 50 – 120 km region of the mesosphere and lower thermosphere. The main data on airglow emission were obtained with the Wind Imaging Interferometer (WINDII) and the High Resolution Doppler Imager (HRDI) on the UARS satellite and the Optical Spectrograph and

Low Cost Earth Sensor based on Oxygen
Airglow – Final Report
ESA Contract #20267/06/NL/JA
Issue: 1   Review: 5
Date: 29/08/08
Page: 21 of 88
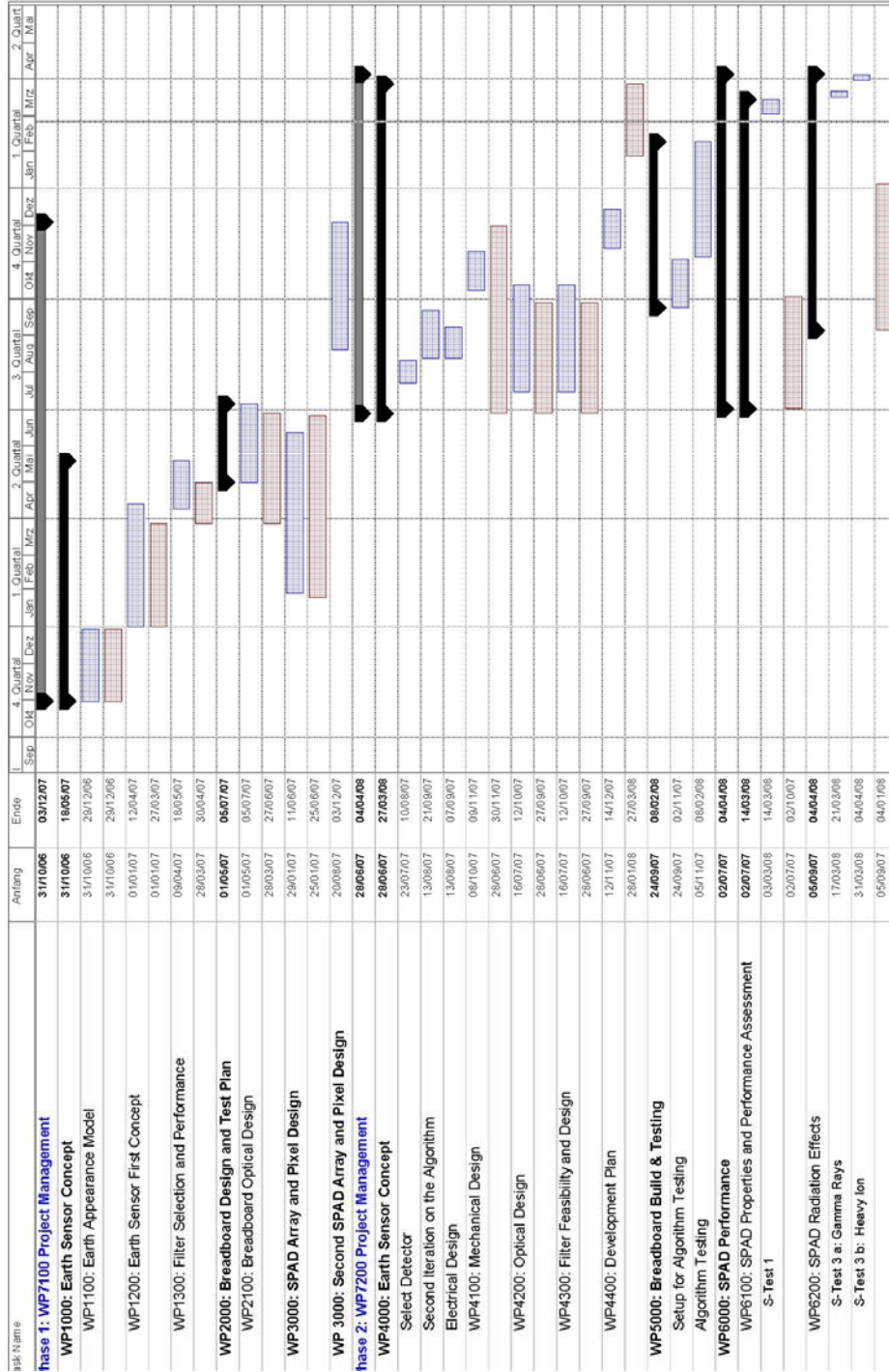
Infrared Imager System (OSIRIS) on the ODIN satellite. They provide a wide database on the airglow emission rates of the 557.7 nm line and the 762 nm band for different altitudes, local times and latitudes [11].

For space observations, the emission of the O_2(0-0) A-Band at 762 nm has several advantages compared to the 557.7 nm line. These emissions are stronger and less perturbed by background radiation or aurora effects. They provide a more constant and strong light source and hence the better basis for an earth sensor.

The 762 nm O_2(0-0) A-Band molecular oxygen band emits the airglow with intensities varying from 2 kR to 1.2 MR at zenith and 400 kR and 240 MR at limb (see TABLE 3). Limb emissions are 200 times stronger than zenith emissions due to the fact that the emissions brightness represents an integrated volume emission rate along the line of sight. Thus, images of the airglow will be characterized by a continuously increasing emission intensity towards the limb, a peak brightness at an altitude of 60 km during day and 95 km at night and a sudden drop of the emissions intensity when reaching the maximum altitude of airglow emission around 120 km. The emission of the O_2(0-0) A-Band is not visible form the ground because of the deep absorption by the dense lower atmospheric O_2 – layer at an altitude of 60 km. This is a significant advantage for space based observations since this layer will act as a filter for the rescattered emission by the earth due to sun- or moonlight. Thus, the main sources of perturbation in the airglow are auroras which emit weakly at 762 nm. Measurements of the 762 nm O_2(0-0) A-Band can be used to get information about the ozone profile, the temperature climatology for mesopause region or atmospheric winds.

TABLE 3: AIRGLOW OF THE O_2(0-0) A-BAND AT 762 NM [7],[8]

Airglow Emission	At zenith	At limb
At night [Rayleighs]	2 k – 10 k	400 k – 2 M
At day [Rayleighs]	120 k – 1.2 M	24 M – 240 M
Aurora perturbations [Rayleighs]	200 – 7 k	100 – 3.5 k

4.2   Earth Appearance Model at 762 nm

In order to determine the requirements on the SPAD detector array and the optical system, and to further test the earth vector determination and earth presence detection algorithm an Earth Appearance Model has been developed. This model simulates the appearance of the earth at 762 nm as seen from a satellite in a GEO and includes

- The minimum, maximum and mean airglow emissions at 762 nm
- Airglow intensity variations depending on the local solar time at zenith (LST)
- Aurora effects around the poles
- Perturbations due to the moon (direct reflection form the sunlight)

4.2.1   Assumptions

The Earth Appearance Model is based on several assumptions and is therefore not a precise simulation of the airglow. However, it allows estimating the variations in airglow intensities and designing a robust earth vector determination algorithm. The main assumptions are:

-   The satellite has an altitude of 36000 km
-   The aperture of the optics has a diameter of 10 mm
-   The perturbations due to the moon will locally saturate the detector
-   The Earth is an ellipsoid with a radius of 6378 km at the equator and a radius of 6357 km at the poles

4.2.2   Mathematical Concept

In order to simulate the image of the earth as it is seen from a satellite, a 3-D space relating each point to a certain local solar time, altitude and latitude has been built. The image can be calculated by integrating the volume emission rate along the line of sight of each point of the image as represented in Figure 16 to Figure 18 .
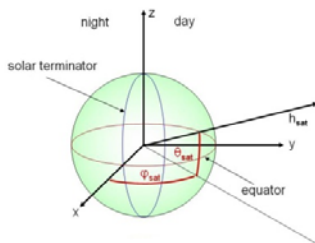
Figure 16: 3-D space relating each point to a certain local solar time at zenith, altitude and latitude.
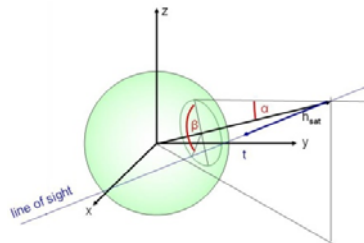
Figure 17: α and β: image parameters used to construct the image as seen form satellite.
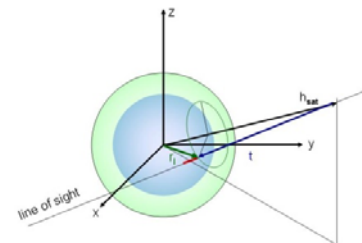
Figure 18: Construction of the image by integrating along the line of sight t.

An image is constructed according to the following algorithm:

1. Insert satellite vector in the 3-D airglow emission space, where

$$\varphi_{sat} = \frac{[local\_solar\_time - 6] \cdot \pi}{12}$$

$$\theta_{sat} = \frac{[latitude] \cdot \pi}{180}$$

$$r_{sat} = [altitude] + R_E$$

R_E : local radius of the Earth

altitude/latitude/local_solar_time (at zenith): parameters to characterise the position of the satellite during airglow observation

2. For each pixel of the image:

    a. calculate the corresponding parameters α and β

    b. determine the coordinates of the vector t which defines the line of sight

    c. integrate the volume emission intensity for each point of the line of sight with a resolution of 5 km

The output of the above described algorithm is given in Rayleigh. The effective photon flux on a single pixel of the detector can be calculated with the formula

$$\Phi_{pixel} = \Phi_{airglow} \frac{1}{4\P} 10^4 \cdot A_D \cdot^- \quad [\text{photons/s}^{-1}]$$

where A_D is the aperture of the telescope [m^2] and ω is the solid acceptance angle [sr]. As shown on the images here after, there will always be a signal emitted at the limb which is usable to calculate the earth vector.
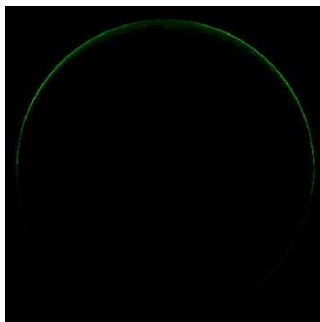
| Mean airglow emission at 24:00 LST | Mean airglow emission at 06:00 LST | Mean airglow emission at 12:00 LST |
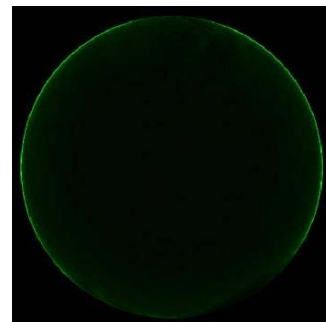
Figure 19: Signal emitted by the airglow as seen from a GEO for different local solar times at zenith.

4.2.3   Earth Model Graphical Interface

The graphical interface of the Earth Appearance Model is shown in Figure 20. It visualises the earth appearance at 762 nm as seen from a GEO as well as the intensity distribution of the airglow emission for two different pixel lines. The user of this interface can modify/choose different parameters, namely
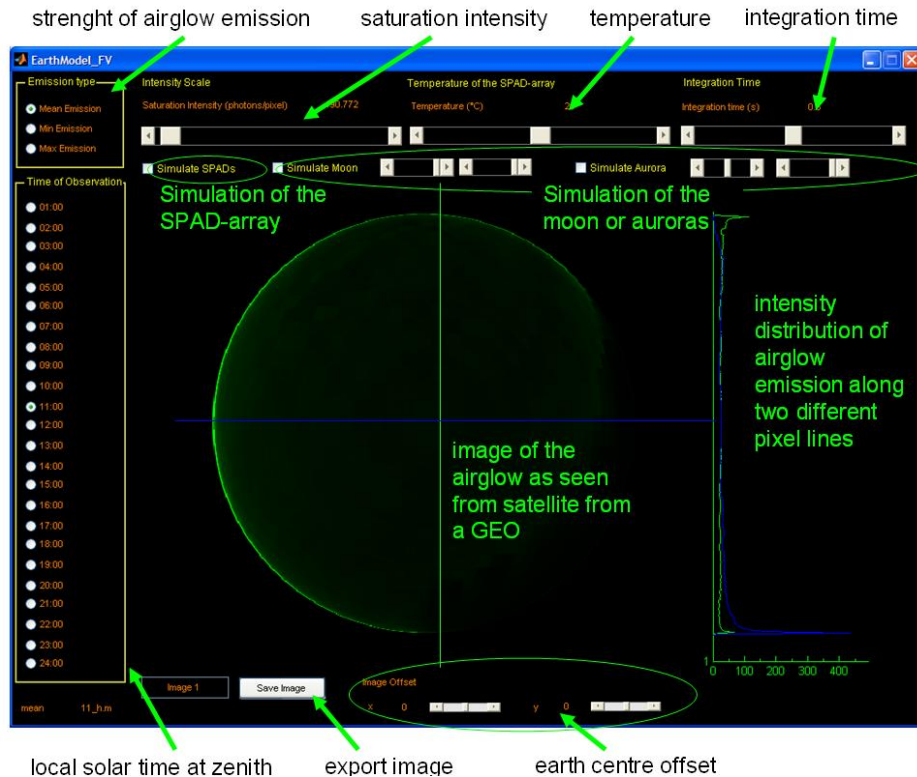
Figure 20: Earth model graphical interface.

- **the local solar time at zenith**

  Airglow intensity depends most of all on the solar irradiation. Hence, the earth appearance is strongly affected by the local solar time at zenith.

- **the strength of the airglow emission,**

  Airglow emissions are modulated by gravity waves, by atmospheric tides and by semi-annual, annual and longer-term variations as for example the solar cycle. However, their emission intensity remains within the given minimum and maximum emission intensity.

- **the simulation of the moon or auroras**

  Moon or auroras might perturb the algorithm used to determine the earth vector. Thus, they have been included in the Earth Appearance Model to test the robustness of the algorithm. However, auroras are visible only for a very low saturation and airglow intensity.

- **the earth centre offset**

  The centre point of the earth can be shifted to test the robustness of the algorithm if the earth is only partially within the FOV.

- **the saturation intensity**

The saturation intensity allows visualising the different intensities of airglow emissions and simulating a saturation of the detector array by adapting the intensity scale.

- **the simulation of the SPAD-array**

   The Earth Appearance Model was extended to simulate the airglow emissions as seen with the SPAD array by introducing a temperature dependency of the SPAD-noise (DCR) and a lower pixel resolution corresponding to the planned 128x128 array[1]. It allows analysing the impact of these parameters on the airglow observations and helps designing and testing the algorithms to determine the earth vector.

The user can furthermore export an image as *.tif and as *.m file. The file name can be specified by the use by inserting the corresponding text in the textbox on the left of the "Save Image" button.

---

[1] The Earth Appearance Model has a four times better resolution than the SPAD array.

5   EARTH SENSOR DESIGN

The earth sensor concept which is presented in this report is based on imaging atmospheric oxygen emission at 762 nm using highly sensitive detectors. In both nighttime and daytime there is continuous emission at 762 nm due to oxygen recombination. A low-light detector enables the ES to operate at night and day, over a wide temperature range, with a very compact optical system (aperture of 8 mm, focal length of 11 mm) and no scanning elements. A modular design allows designing similar instruments using the same wavelength band, the same detector technology, the same optics, the same power and data interfaces and similar algorithms for GEO and LEO applications, thus reducing the development cost. The main difference between the instrument used in a GEO or a LEO is the optical geometry: whereas a single tube design will be used in GEO, a triple-tube concept will be used for LEO to provide a larger FOV (Figure 22). For both geometries, the volume of the instrument will be minimized, its mass will not exceed 1.5 kg for a LEO- and 750 g for a GEO-instrument, and the power consumption will be less than 4 W. The goal is to design the instrument as simple and compact as possible. Using the visible band rather than the LWIR band offers several advantages including much lower cost detectors, no need for cooling, a more relaxed thermal design, simpler optics, no need for any scanning mirrors or choppers, higher sensitivity and hence low cost.

5.1   Unit overview and concept of operation

5.1.1   Geometrical Concept

The angular size of the earth differs significantly if it is seen from a LEO (100° to 160°, see Figure 21) or a GEO, where the earth's angular size is around 17°. This difference has an important impact on the conceptual design of the earth sensor and requires a modular instrument design: Whereas the same wavelength band, the same detector technology, the same optics, the same power and data interfaces and similar algorithms can be used for both orbit classes, a different optical geometry and a different mechanical design will be used for each application. While a "single-tube" design covering a FOV of 20° is best suited for GEO (Figure 6.B.), a "multiple-tube" concept will be used for LEO in order to provide the required FOV of 180° (Figure 6.A.).
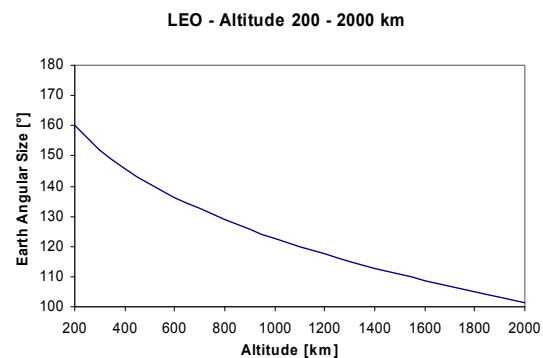
Figure 21: Angular size of the earth as seen from a LEO.

A. LEO   **B. GEO**
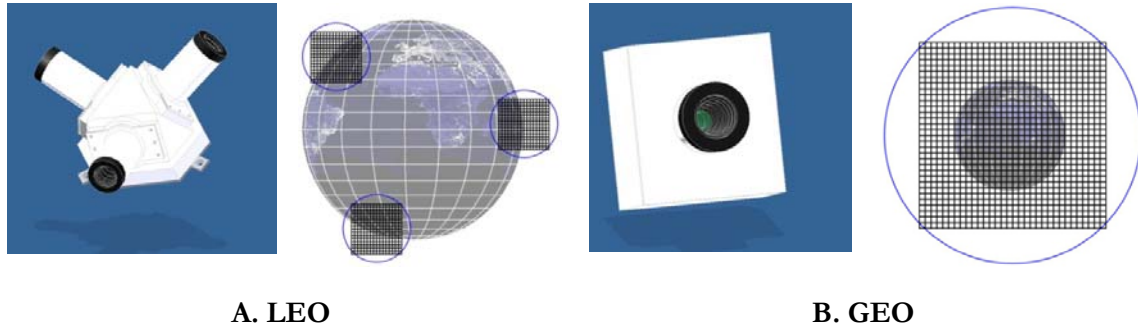
Figure 22: Earth Sensor configurations and geometries. The dark blue circles mark the telescopes FOV, whereas the black arrays indicate the view of the active sensor elements. A. LEO case at 2'000 km altitude: Three telescopes each with a sensor array and a 20° FOV are used. B. GEO case at 36'000 km altitude: One telescope only, with a FOV of 20° and one detector array.

5.1.2   Operational Description of the Earth Sensor "AIRES"

The task of an earth sensor is to determine the earth vector (vector pointing from the satellite to the earth centre) in order to define the orientation and the approximate distance of the satellite with respect to the earth. For the AIRES instrument, this task will be accomplished by taking a picture of airglow emissions, a permanent photoluminescence phenomenon occurring at an altitude of about 80 km [1], and determining the earth vector though image processing.

The operational flow of the AIRES instrument is represented in Figure 23 and is expected to include an acquisition, a tracking and a standby mode. As represented with the black arrows, the ES can go from any mode into acquisition or standby mode at any time. The only mode, which needs an initialisation phase (done with the acquisition mode) is the tracking mode. The main difference between acquisition mode and tracking mode is the size of the space defining possible position of the earth centre and thus the required processing time and the reliability of the ES output. Each mode is briefly described hereafter. The detailed operation flow of the image processing algorithm for the acquisition and tracking mode is described in [6].

Figure 23: Operational Flow of the AIRES earth sensor.

Acquisition mode

In *acquisition mode* the ES determines the earth vector based on a single measurement without taking into account previous observations. For this mode, the image processing algorithm (Image processing 1) is characterized by a larger space of possible position of the earth centre. The

Low Cost Earth Sensor based on Oxygen
Airglow – Final Report

ESA Contract #20267/06/NL/JA
Issue: 1   Review: 5
Date: 29/08/08
Page: 28 of 88

processing time required to determine the earth vector is highest for this mode (see paragraph 5.7.2.1 for more details).
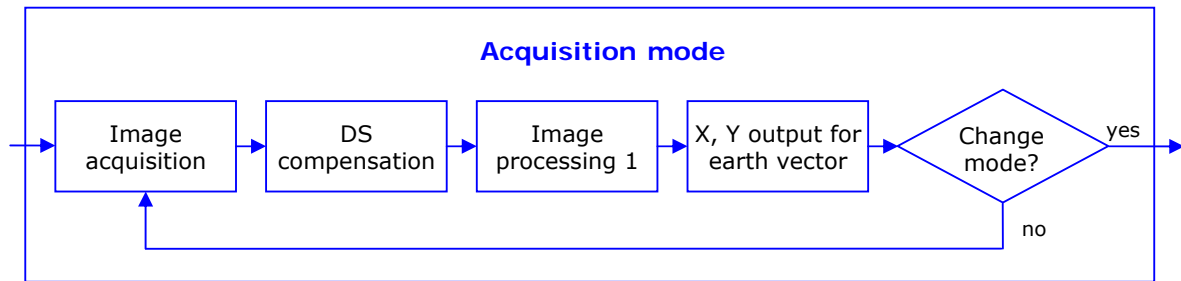
Figure 24: Operation flow during acquisition mode.

Tracking mode

In *tracking mode* the ES determines the earth vector based on the last measurement and previous X and Y outputs. The approximate position of the earth centre is known from previous measurements. Since the satellite movement is expected to be low (max rotation of 3°/s, max speed 7.8 km/s for LEO application and 0.4°/s, respectively 3.1 km/s for a GEO application), the new position of the earth centre will be close to its position during the previous measurement and the space defining the possible position of the earth centre is therefore smaller during this mode of operation. The image processing time is expected to be smaller for this mode (see paragraph 5.7.2.2 for more details).
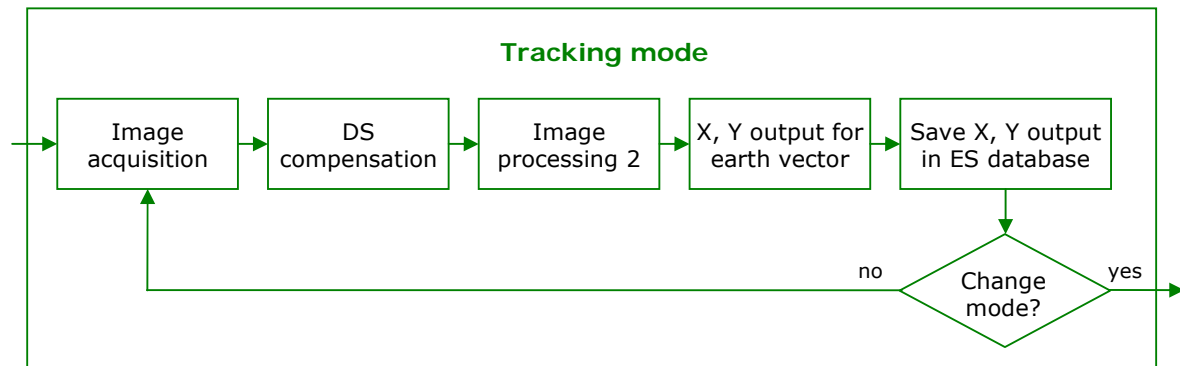
Figure 25: Operation flow during tracking mode.

Standby mode

During *standby mode* all components of the ES which are not required for communication with the satellite are turned off and no determination of the earth vector is performed. This mode is used whenever the detector is blinded by the sun or if the earth vector determination is not required (if the sensor is used as back-up sensor for instance) and allows significantly reducing the power consumption of the instrument.

Low Cost Earth Sensor based on Oxygen
Airglow – Final Report

ESA Contract #20267/06/NL/JA
Issue: 1   Review: 5
Date: 29/08/08
Page: 29 of 88
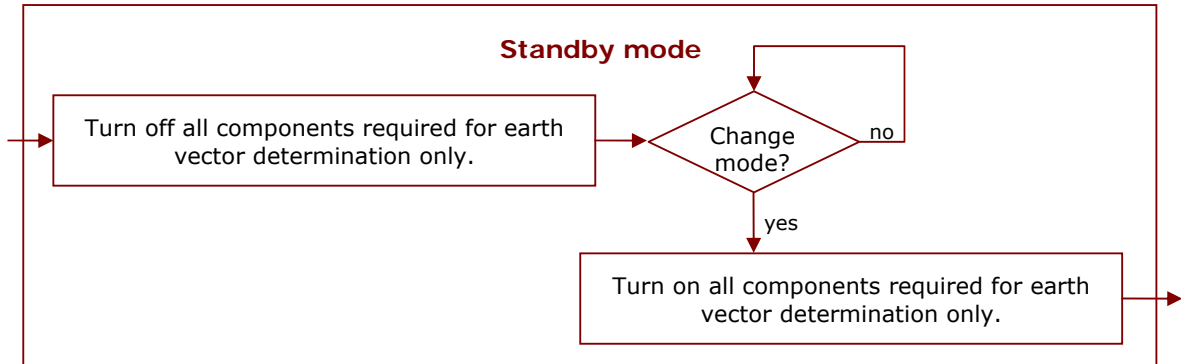
Figure 26: Operation flow during standby mode.

5.1.3   Preliminary   Definition   of   the   Required   Telemetry   and Telecommands

The main telecommands used to control the AIRES ES are listed in TABLE 4. The execution of each command will be performed after the image processing step ("Image processing 1" or "Image processing 2") has been completed and before a new image is captured.

TABLE 4: AIRES TELECOMMANDS

Function	Description
AIRES_SM	Specifies that the ES should go into *standby mode*.
AIRES_AM	Specifies that the ES should go into *acquisition mode*.
AIRES_TM	Specifies that the ES should go into *tracking mode*. If the instrument is in *standby mode*, when this command is received, 3 measurements are done in *acquisition mode* before going to *tracking mode*.

Whenever the AIRES ES is turned on after being shut down, the instrument goes into *standby mode* and waits for further telecommands.

If the ES instrument is in *acquisition mode* or *tracking mode*, its telemetry, described in TABLE 5, is sent to the satellite after each image processing step via RS422.

TABLE 5: AIRES TELEMETRY

Parameter	Description	Size
X	X-coordinate of the calculated earth vector	8 bits [TBC]
Y	Y-coordinate of the calculated earth vector	8 bits [TBC]

		Low Cost Earth Sensor based on Oxygen Airglow – Final Report
AIRES	EPFL / oerlikon components	ESA Contract #20267/06/NL/JA
		Issue: 1 Review: 5
		Date: 29/08/08
		Page: 30 of 88

CS	Confidence signal, parameter which describes the reliability of the calculated earth vector	8 bits [TBC]
S	Sun blinding flag, activated if a major part of the detector is saturated	1 bit
E	Earth presence flag, activated if the earth is within the FOV	1 bit
T	Temperature of the detector	8 bits [TBC]

5.2   Mechanical Design

5.2.1   AIRES Instrument for GEO Applications

Figure 27 to Figure 29 show the instrument for a GEO application. Its main parts are a single optical "tube", a mainboard, a DC/DC-board[2] and a housing protecting and stabilising the optics and the electronics of the earth sensor. An estimation of the mass of the different components of the overall GEO instrument is given in TABLE 16, a more detailed analysis on the components of the optics is given in TABLE 15, whereas a rough estimation of the instrument's dimensions is given in Figure 28.

It is still preliminary design of the ES and further design iterations are required to find the optimal solution. Some improvements are likely possible on the thermal and mechanical stability of the ES as well as on its mass, these will be addressed during a subsequent detailed design phase.
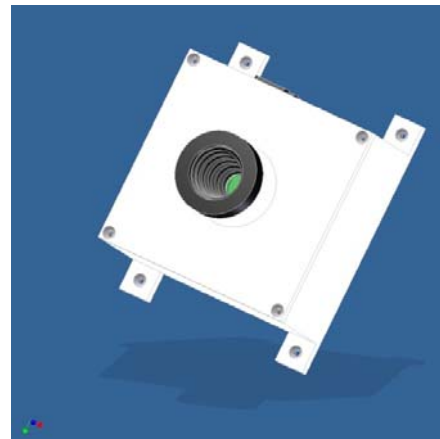
Figure 27: Single-tube configuration of the AIRES instrument for GEO applications.

---

[2] See section 5.5 for more information on the electronic design.

Low Cost Earth Sensor based on Oxygen
Airglow – Final Report
ESA Contract #20267/06/NL/JA
Issue: 1   Review: 5
Date: 29/08/08
Page: 31 of 88
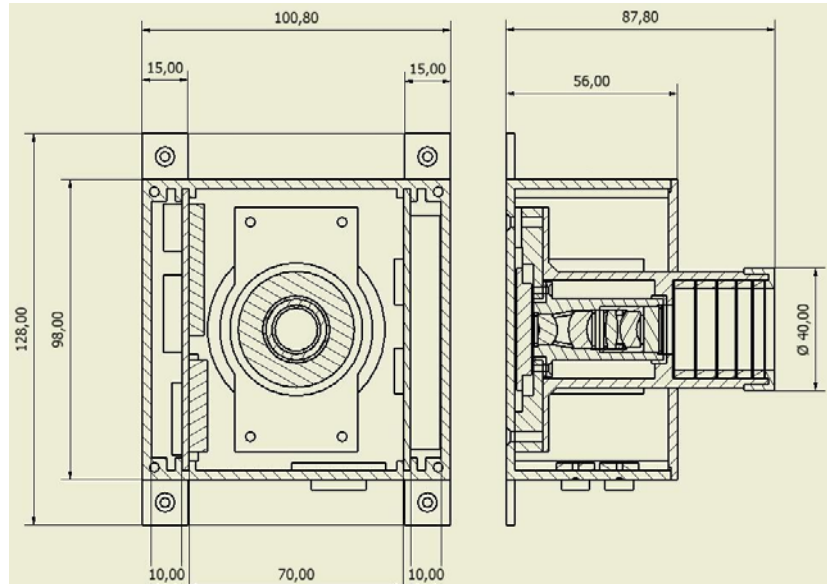
Figure 28: Rough dimensions for the AIRES instrument for GEO applications.
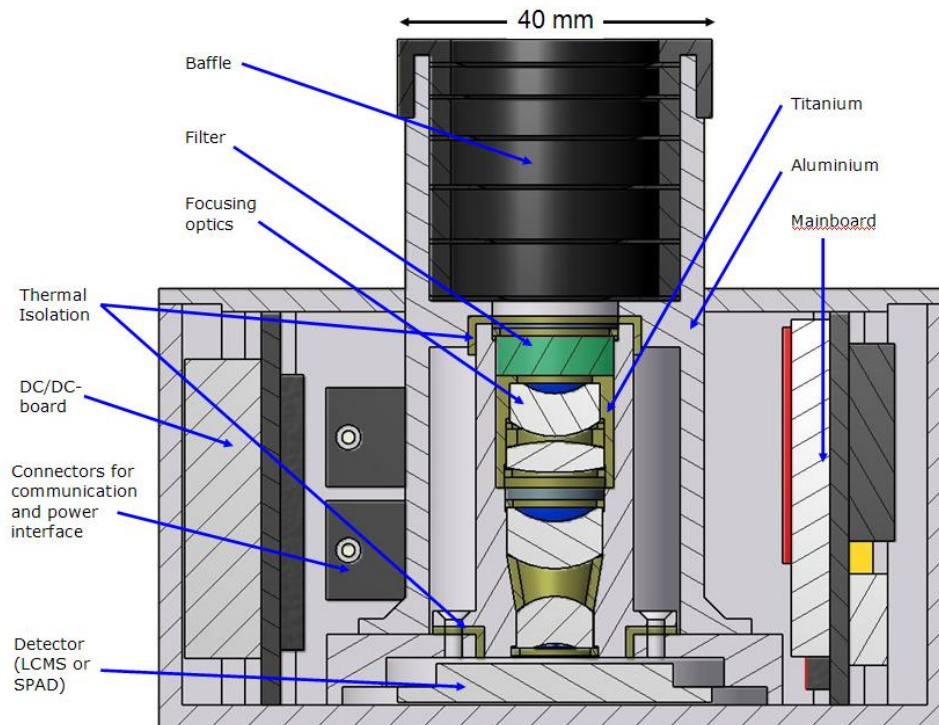
Figure 29: Cut through the preliminary design of the AIRES instrument for GEO applications.

5.2.2   AIRES Instrument for LEO Applications

The ES instrument for LEO applications includes three "tubes", each equipped with its own optical system, detector and detectorboard. The box holding the single motherboard has a different geometry due to the "triple-tube" configuration. As for the GEO instrument, the mechanical design is in a preliminary phase and has to be optimised.
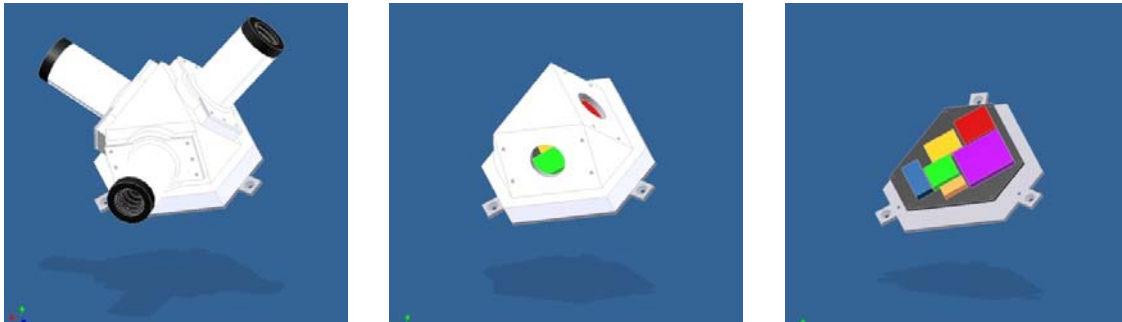
Figure 30: Triple-tube configuration of the AIRES instrument for LEO applications.
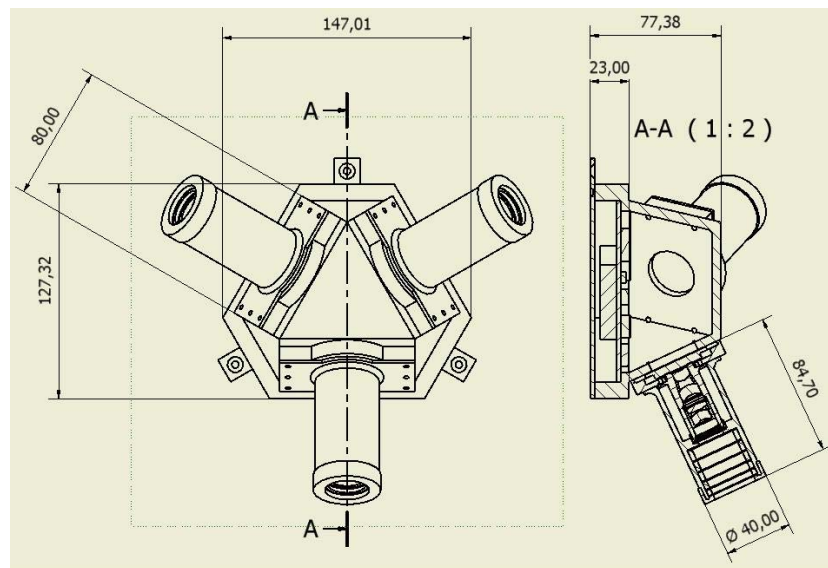
Figure 31: Rough dimensions of the AIRES instrument for LEO applications.

5.3   Optics

Since the key objective of this earth sensor concept is to design a low recurring cost instrument, the optical system of the ES has to be as simple as possible, but still guarantee good results. The advantage of this procedure is that the optical system is much simpler, hence much lower cost and could be used with any detector (APS, CMOS, CCD). However, if microlenses are used to

improve the fill-factor of the detector, as it would be required for the SPAD-array, the overall optical efficiency might significantly be degraded (estimated efficiency of the optical system and the microlenses (OE x FF) of 8.3%, compared to an estimated efficiency of 50% if the optical system is optimised for the microlenses).

5.3.1   Requirements on the Optical System

The requirements on the optical system are summarised in TABLE 6 and allow identifying which optical design might be suited for the AIRES application: A large FOV and a small focal length correspond to an optical system with a small F/# (0.87 – 1.3, depending on the targeted FOV). Possible systems are therefore Cooke triplet, double Gauss, Petzval or a paraxial layout. Since the optical system has to be as simple (and thus cheap) as possible, a paraxial design based on the Petzval system has been chosen for the ES.

TABLE 6: REQUIREMENTS ON THE OPTICAL SYSTEM

Parameter	Specification	Final Design
Working Wavelength	762 nm	762 nm
Total FOV	20 – 30 °	20 °
FOV per pixel	< 0.3 °	0.16 °
Aperture Ø	≥ 8 mm	8 mm
Focal Length		10.88 mm
Pixel Pitch	≥ 30 µm	30 µm
Detector Size	3.84 mm x 3.84 mm	3.84 mm x 3.84 mm

The final design is shown in Figure 33. It consists of four lenses whereof three are meniscus lenses with medium radius of curvature and one is a biconvex lens. The system is free of vignetting. The aperture stop is placed in front of the first lens in order to limit the size of the lenses. However, an aperture stop which is placed closer to the detector would provide a better straylight blocking. The total length of the system is 35.3 mm. The materials used for the lenses are F2G12, LAK9G15 and SF6G05 which are radiation insensitive.

It is important to note that the presented optical design shows the minimum required optical surface and does not correspond to the final size of the lenses. Indeed, the diameter of the lenses might have to be increased to reduce straylight on the detector.

Low Cost Earth Sensor based on Oxygen
Airglow – Final Report
ESA Contract #20267/06/NL/JA
Issue: 1   Review: 5
Date: 29/08/08
Page: 34 of 88

Surface #	Surface Name	Surface Type	Y Radius	Thickness	Glass	Refract Mode	Y Semi-Aperture
Object		Sphere	Infinity	Infinity		Refract	O
Stop		Sphere	Infinity	2.1000 ᵛ		Refract	4.0000 O
2	L1F	Sphere	-6.8888 ᵛ	5.4449 ᵛ	F2G12_SCHOTT	Refract	4.1280 O
3	L1B	Sphere	-9.4411 ᵛ	0.6000 ᵛ	AIR	Refract	5.9061 O
4	L2F	Sphere	20.9764 ᵛ	3.8920 ᵛ	LAK9G15_SCHOT	Refract	6.4629 O
5	L2B	Sphere	-34.5871 ᵛ	6.5032 ᵛ	AIR	Refract	6.3609 O
6	L3F	Sphere	-7.8797 ᵛ	4.4852 ᵛ	LAK9G15_SCHOT	Refract	5.2947 O
7	L3B	Sphere	-9.7133 ᵛ	3.4411 ᵛ	AIR	Refract	6.2994 O
8	L4F	Sphere	7.5698 ᵛ	6.0000 ᵛ	SF6G05_SCHOTT	Refract	5.0297 O
9	L4B	Sphere	7.5496 ᵛ	2.8565 ᵛ	AIR	Refract	2.9187 O
Image		Sphere	Infinity	0.0000	AIR	Refract	1.8430 O

Figure 32: Detailed design of the optics for the AIRES ES.
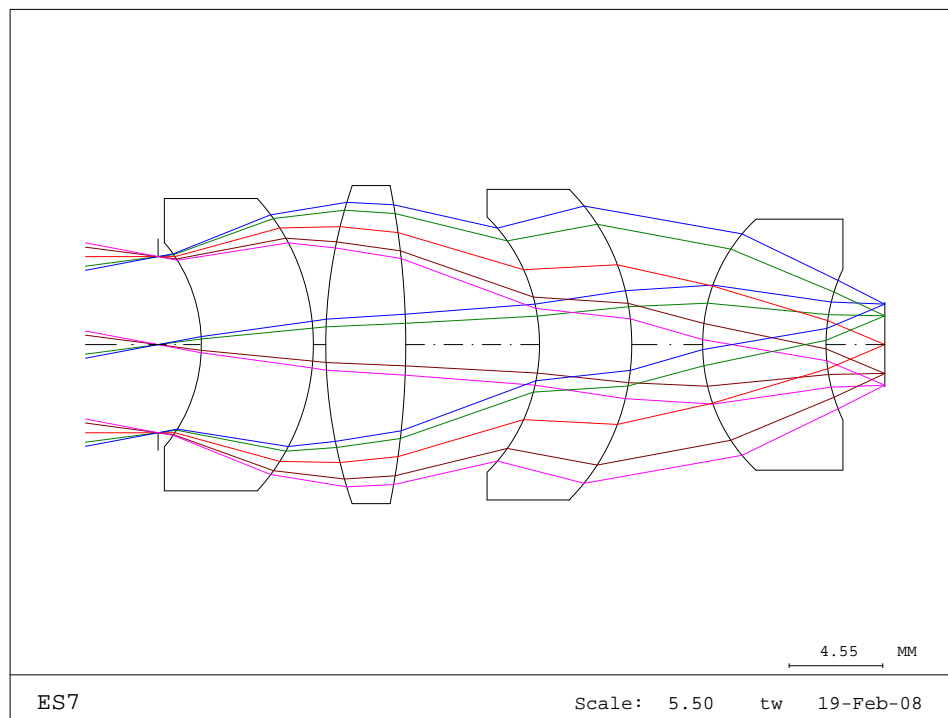
Figure 33: Final design for the AIRES optics.
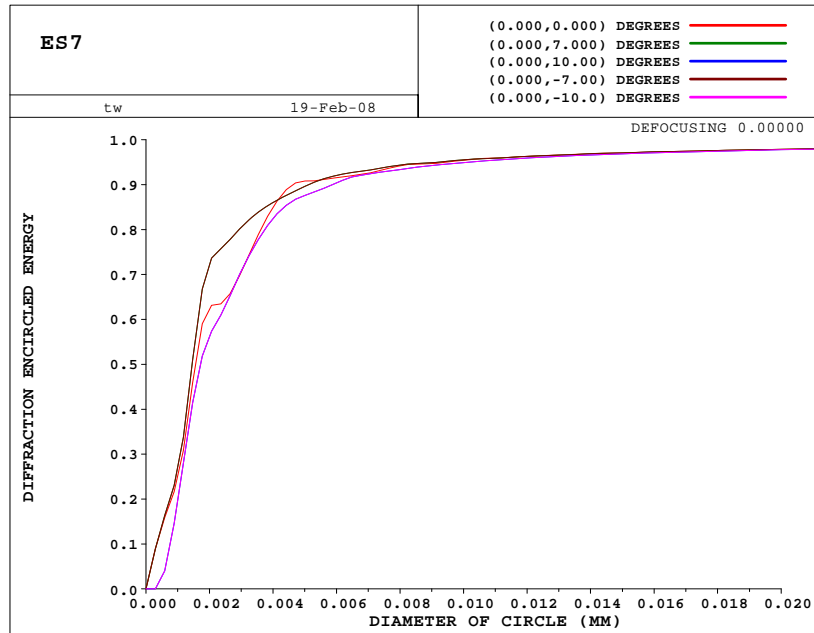
Figure 34: Encircled energy of the final design for the AIRES optics.

5.4   Filter

5.4.1   Filter Requirements

The filter function for the ES sensor is to restrict the incoming light to the airglow wavelength as well as to protect the sensor in case of direct boresight pointing at the sun. The requirements for the filter are listed below.

TABLE 7: REQUIREMENTS ON THE FILTER

Mirror coating	Specification
Coated surface dimension (active)	Ø9 mm (TBC)
Operating wavelength	760-765 nm
Incident medium index	Vacuum
Angle of Incidence	0 – 10°
Transmission	[0.75,0.85] @ 759 – 773 nm $<10^{-5}$ outside
Incident light polarisation status	Unpolarised
Coating defects (acc. To ISO 10110 part 7)	5 / 5 x 0.1 (TBC), L 2x0.025 (TBC, or less)
Coating Surface quality	scratch / dig 20 /40
Operation Temperature	-40° C to +70° C
Non-Operation Temperature	-100° C to +100° C

Durability requirements	Qualification of the coating shall be achieved/demonstrated wrt: • Humidity • Radiation [30 Krad] • Cleanability • Thermal conditions
Abrasion resistance	MIL-C-675C, Section 4.5.11
Thermal cycling	MIL-C-48497A, Section 4.5.4.1
Humidity resistance	MIL-C-675C, Section 4.5.8
Adhesion	ECSS-Q-70-13A or equivalent

The filter has a 14 nm band-pass centred at 760-765 nm. The transmission should be larger than 0.75 for angles of incidence up to 10° angle, while in the outer spectral range a broad band blocking is required.

The required filtering function is shown in Figure 35.
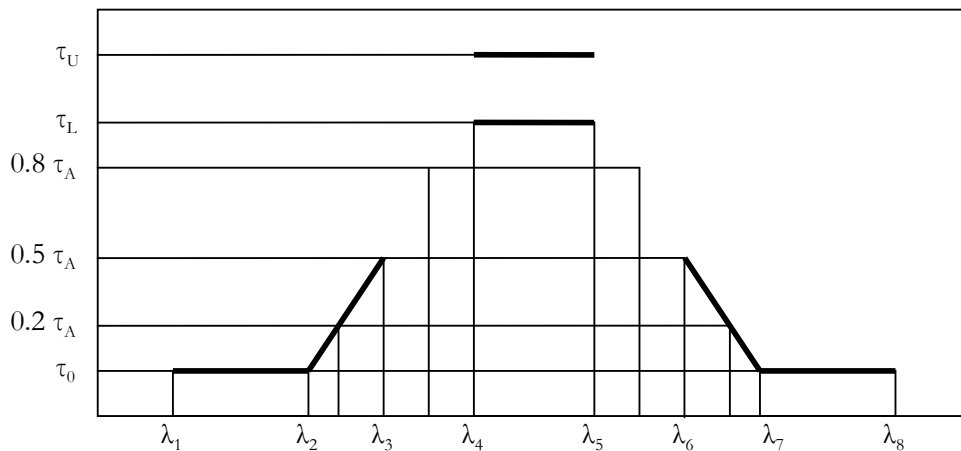
Figure 35: Filtering function of the filter for the earth sensor application.

λ_1 = 100 nm	$\lambda_2 \geq$ 749 nm	λ_3 = 754 nm	λ_4 = 759 nm
λ_5 = 773 nm	λ_6 = 778 nm	$\lambda_7 \leq$ 783 nm	λ_8 = [1500] nm

τ_U = 0.85	τ_L = 0.75	τ_A = 0.5·(τ_U+ τ_L) = 0.8	τ_0 = 0.00001
0.8 τ_A = 0.64	0.5 τ_A = 0.4	0.2 τ_A = 0.16	

5.4.2   Filter Design

The performance of the filter required for the earth sensor application can be achieved by combining three filter layouts. The suggested filter design includes

- A Fabry-Perot filter with two HH cavities. It provides a narrow bandpass filtering centered at 762nm, with a bandwidth of 14 nm and a transmission of 75 - 80 % within the

band. Its transmittance behavior over the whole spectrum is shown in Figure 43 (green curve).

- An induced transmission filter with two silver layers, each with a thickness of 40 nm. This filter is responsible for the blocking on the side of longer wavelengths (red curve in Figure 43)

- A RG630 (TBC) color glass for UV blocking on the side of shorter wavelengths (blue curve). The actual glass still has to be determined.

Each of these filters is briefly described hereafter.

5.4.2.1   Narrow Bandpass Filter

In order to achieve a 14 nm bandwidth, there is no other solution known than a Fabry-Perot-Resonator. The resonator consists of a layer (called the cavity) with an optical thickness D which is a multiple of $\lambda/2$. On both sides of the cavity there is a partial transmitting reflector.
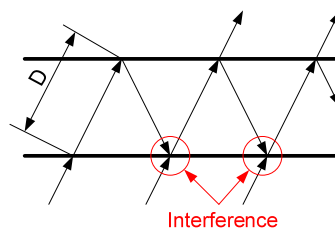
Figure 36: Schematic representation of a Fabry-Perot resonator.

The reflectors keep the main fraction of the light inside the cavity. The reflected light interferes with the incoming light after being reflected on each side of the cavity. Since there are many reflections involved, only light with a wavelength with constructive interference ($2D=\lambda$, 2λ, 3λ) in a narrow band is able to propagate through the filter.

Design of the Partial Reflectors

Dielectric layer stacks with alternating high (H) and low (L) refractive index are used for the partial transmitting reflectors as shown in Figure 37. One layer has an optical thickness of $\lambda/4$, where λ corresponds to the central wavelength.
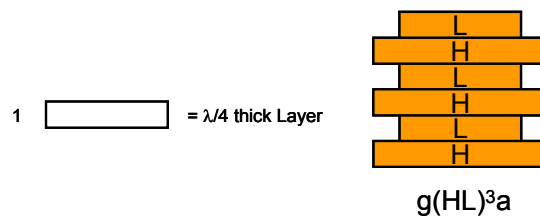
Figure 37: Example of a multilayer filter built with 3 combinations of High and Low materials.

General Design of a Fabry-Perot Cavity

The Fabry-Perot consists of a cavity with a thickness of λ/2, with two partially transmitting reflectors on each side. The performance of the Fabry-Perot is tuned by the reflectivity and transmission of the two reflectors, i.e. the number of layers and the materials that are used. There are two basic configurations which differ in the refractive index of the λ/2-cavity layer.
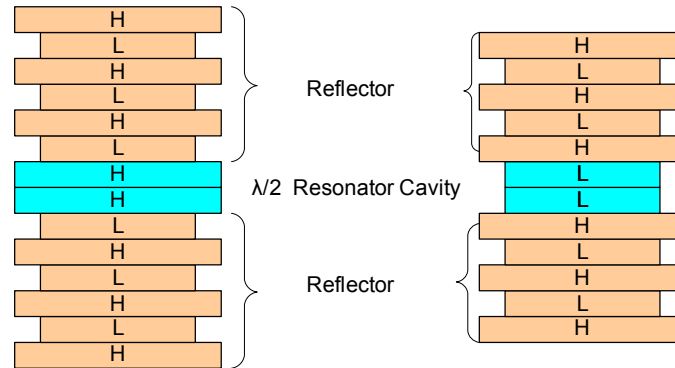
Figure 38: Basic configuration of the Fabry-Perot cavity with the central λ/2-cavity and two reflecting layers stacks on both sides. The cavity layer can have either high (H) or low (L) index.

Performance of the Bandpass Filter

The bandpass filter which fitted the best the requirements of the AIRES project and was therefore selected for this application comprises two cavities and has the following configuration:

$$(HL)^2 \, 2H \, (LH)^2 \, L \, (HL)^2 \, 2H \, (LH)^2$$

with   - L film = SiO_2 (n_L=1.45406)
        - H film = Ta_2O_5 (n_H= 2.12127)

The overall performance of the Fabry-Perot filter is shown in Figure 39. Since the blocking introduced by the reflectors has a limited bandwidth, supplemental filters are required. Hence, a red and blue blocking filter (described in paragraph 5.4.2.2 and 5.4.2.3) are added to the filter assembly.

Low Cost Earth Sensor based on Oxygen
Airglow – Final Report

ESA Contract #20267/06/NL/JA
Issue: 1   Review: 5
Date: 29/08/08
Page: 39 of 88
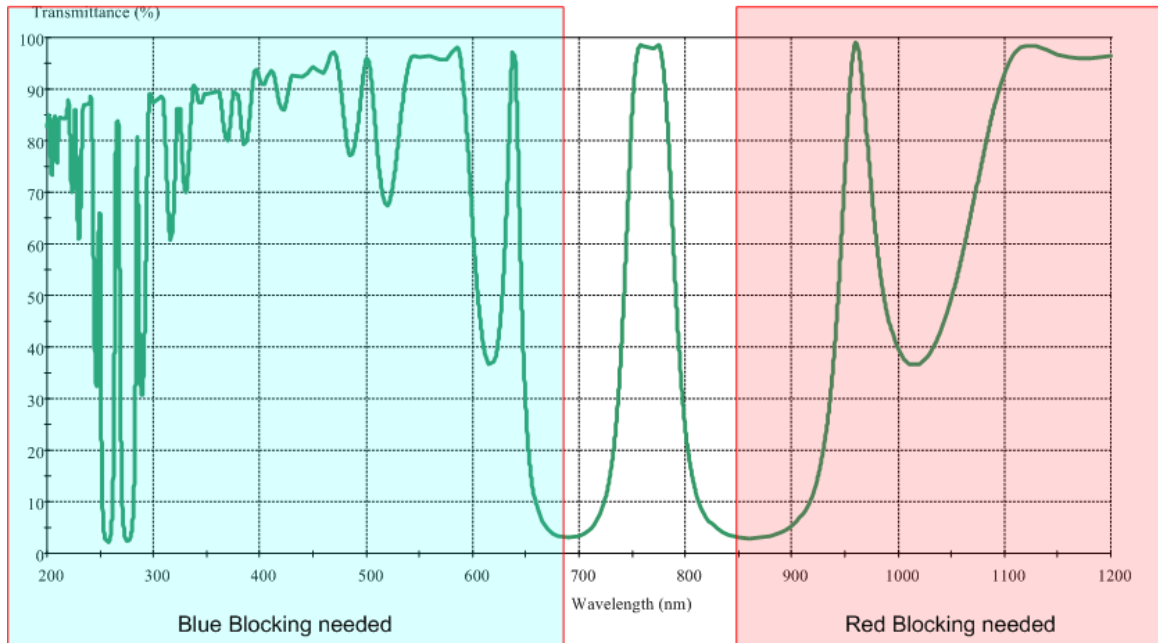
Figure 39: Transmittance curve of the interference filter chosen for the narrow band-pass. For blocking the light in the IR and the UV regions, two separate solutions are necessary.

5.4.2.2   Induced Transmission Filter (Red Blocking Filter)

An effective way for blocking light consists of adding a metal or semiconductor layer. Metal layer have been chosen for the AIRES application, since they are simpler to implement. They provide a high attenuation in light transmission over a large bandwidth.

The structure of the suggested induced transmission filter is outlined in Figure 40. Two silver layers with a thickness of 40 nm (red) and separated by 2H layers, have been inserted between two (HL)² stacks. As for the previous filter, the dielectrics consist of SiO_2 and Ta_2O_5. A matching layer (green) connects the metal layer and the (HL)², respectively the 2H, and increases the transparency of the metal layer.

The performance of this filter is shown in Figure 41. It provides a transmission of 85 % in the operation band and under 0.001 % for higher wavelengths.

Figure 40: Induced transmission filter with 2 x 40 nm Silver.
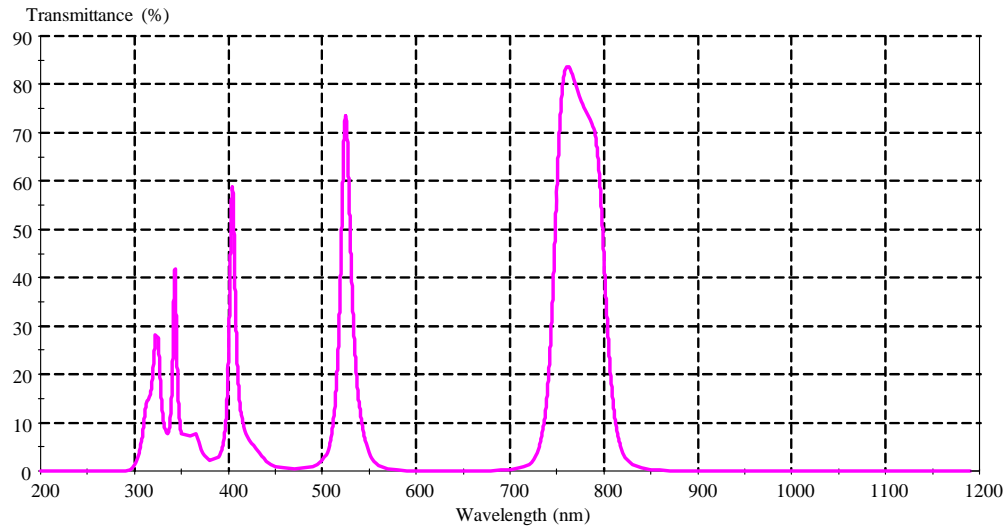
Figure 41: Transmission performance of the induced transmission filter with 2 x 40 nm silver.

5.4.2.3   Color Glass Filter (Blue Blocking Filter)

The transmission of a color glass filter is homogeneously suppressed over all wavelength smaller than the cut-on wavelength which is given by the glass number. Thus, a filter with a cut-on wavelength close to the targeted filter bandwith (i.e. RG 695 or RG 715) seem to be appropriate for the AIRES application.

However, the steepness of the cut-on edge of a color glass filter is affected by radiation as shown in Figure 42. Furthermore, its transmission might also be reduced. Thus, several filter samples of different RGxxx glasses have to be tested under a radiation dose of 1 Mrad to determine which is the best suited glass filter for the AIRES application. The RG630 has been chosen for the current filter design.
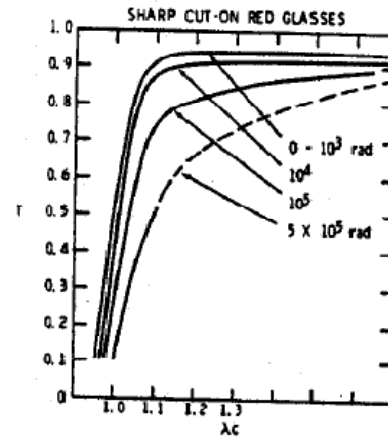
Figure 42: Transmittance curve versus λ_c (cut-on wavelength) for several radiation doses.

5.4.3   Final Filter Performance

The transmittance curve over the whole spectrum resulting from the presented filter combination is given by the black curve in Figure 43 and Figure 44 for an angle of incidence of 0°, respectively 10°.
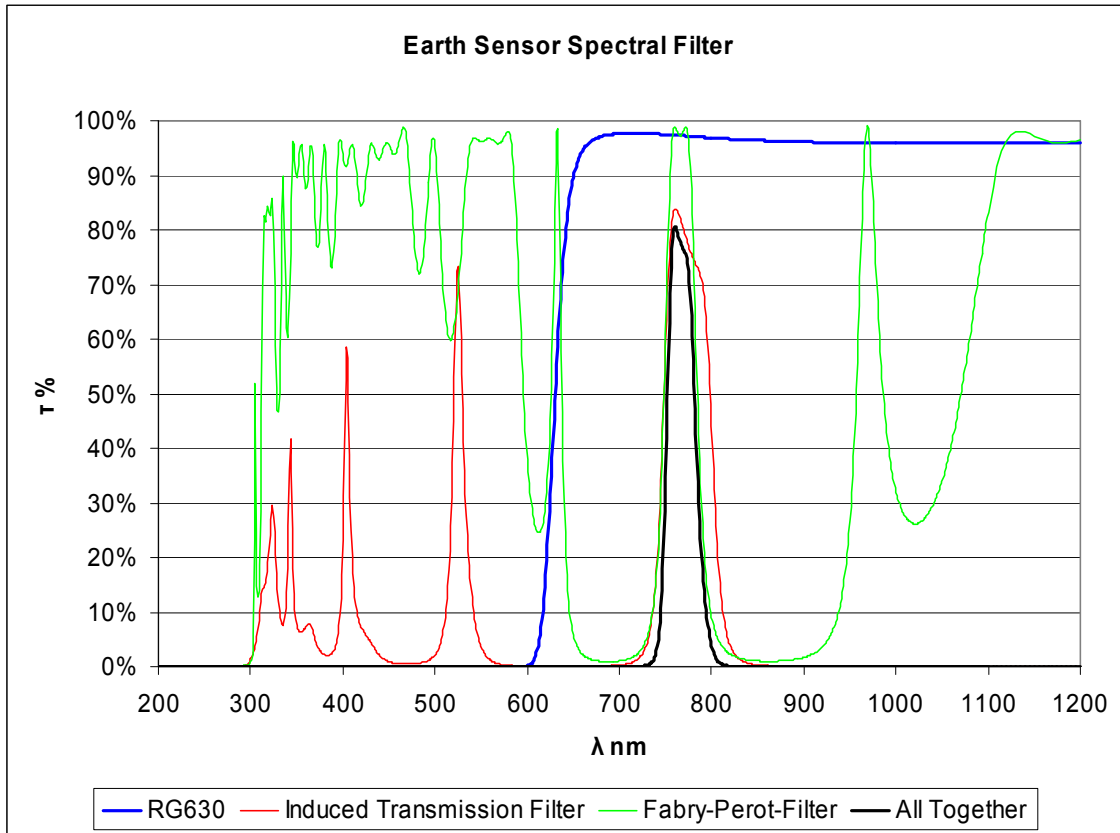
Figure 43: Transmittance of the final solution for the earth sensor spectral filter. The black curve is the result of the combination of the induced transmission filter (red curve), the Fabry-Perot (green curve) and the RG630 color glass (blue curve).
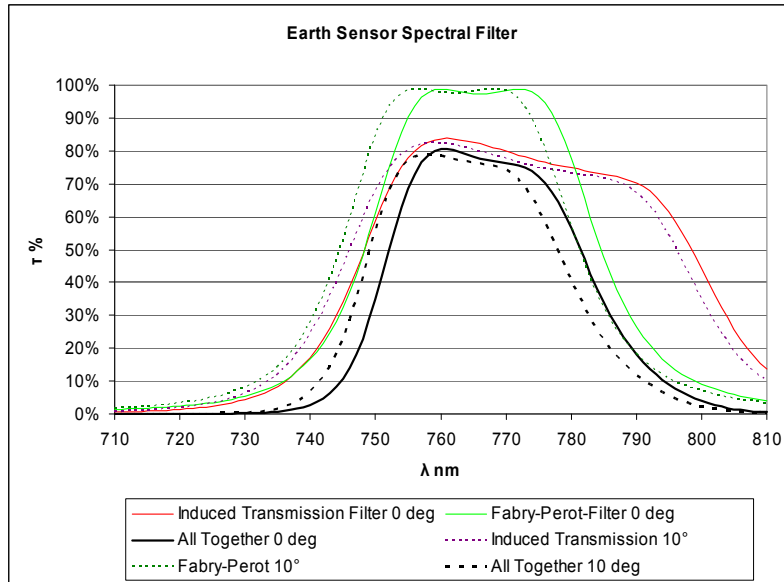
Figure 44: Transmittance of the earth sensor spatial filter for normal (straight lines) and 10° (dashed line) incidence of the light.

The blocking is shown in Figure 45 and corresponds to <-50dB on the side of shorter wavelength (except for a single peak at 640 nm, which might be avoided if glass with a higher cut-on wavelength was chosen). On the side of longer wavelength, the blocking is between -40 dB and -50 dB.
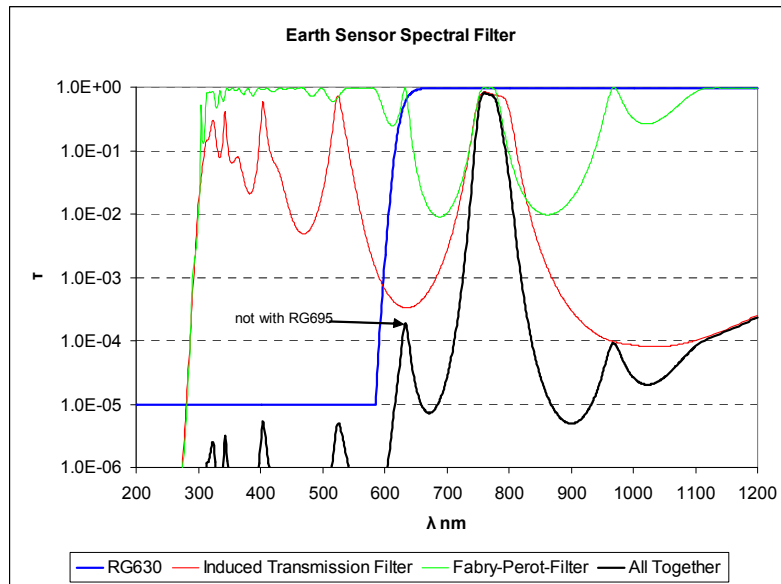
Figure 45: Blocking performance of the composite filter.

5.5   Electrical Design

The preliminary design of the electronic circuit of the ES is shown in Figure 47. Its main components are

- a detector (e.g. SPAD for the baseline design) which captures images of airglow emissions,
- an FPGA which runs the SPADs (this component may not be required if another detector such as LCSM is used instead of the SPAD),
- a microprocessor which controls and reads the detector, performs data analysis and image processing, and provides the ES telemetry to the satellite bus,
- a serial data interface to link the data interface of the ES to the satellite bus,
- a ROM to store the ES software,
- a RAM, mostly used for image processing,
- an oscillator which generates the reference clock,
- a DC/DC-Converter and voltage regulators to provide the required power supply to all other components.
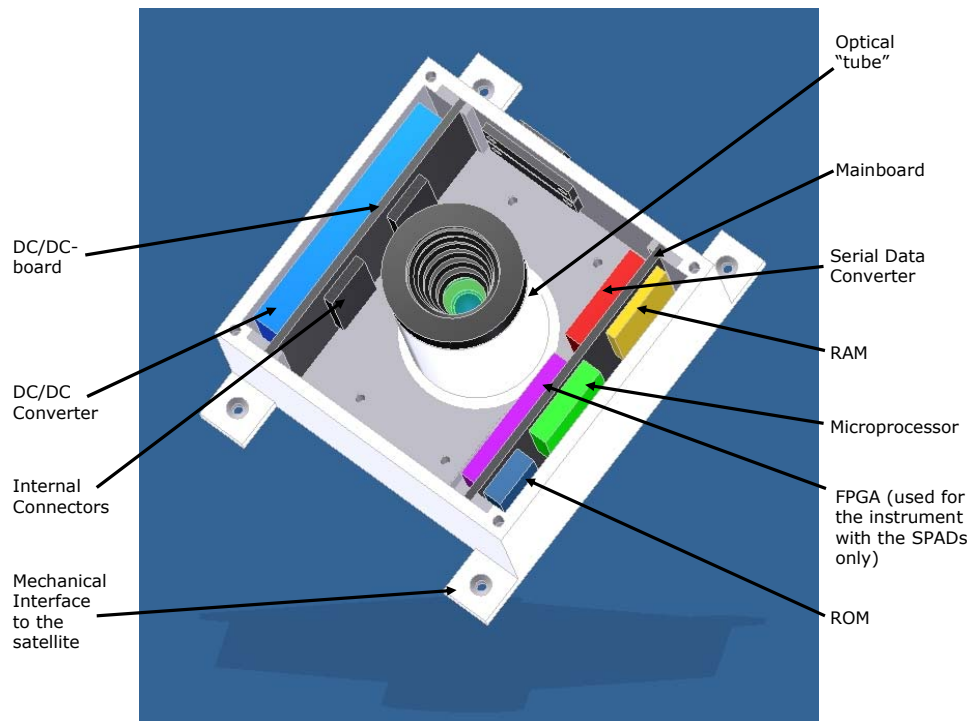
Figure 46: Placement of the electronics in the AIRES instrument for GEO applications.

Since the power interface provided by the satellite may vary, the DC/DC-Converter has to be easily replaceable. Thus it has been put on a separate PCB for the ES design for a GEO application. An estimation of the power consumption of the main components of the ES is given in TABLE 18 whereas a rough sizing and mass budget is given in TABLE 17.

**Low Cost Earth Sensor based on Oxygen
Airglow – Final Report**

ESA Contract #20267/06/NL/JA
Issue: 1   Review: 5
Date: 29/08/08
Page: 44 of 88
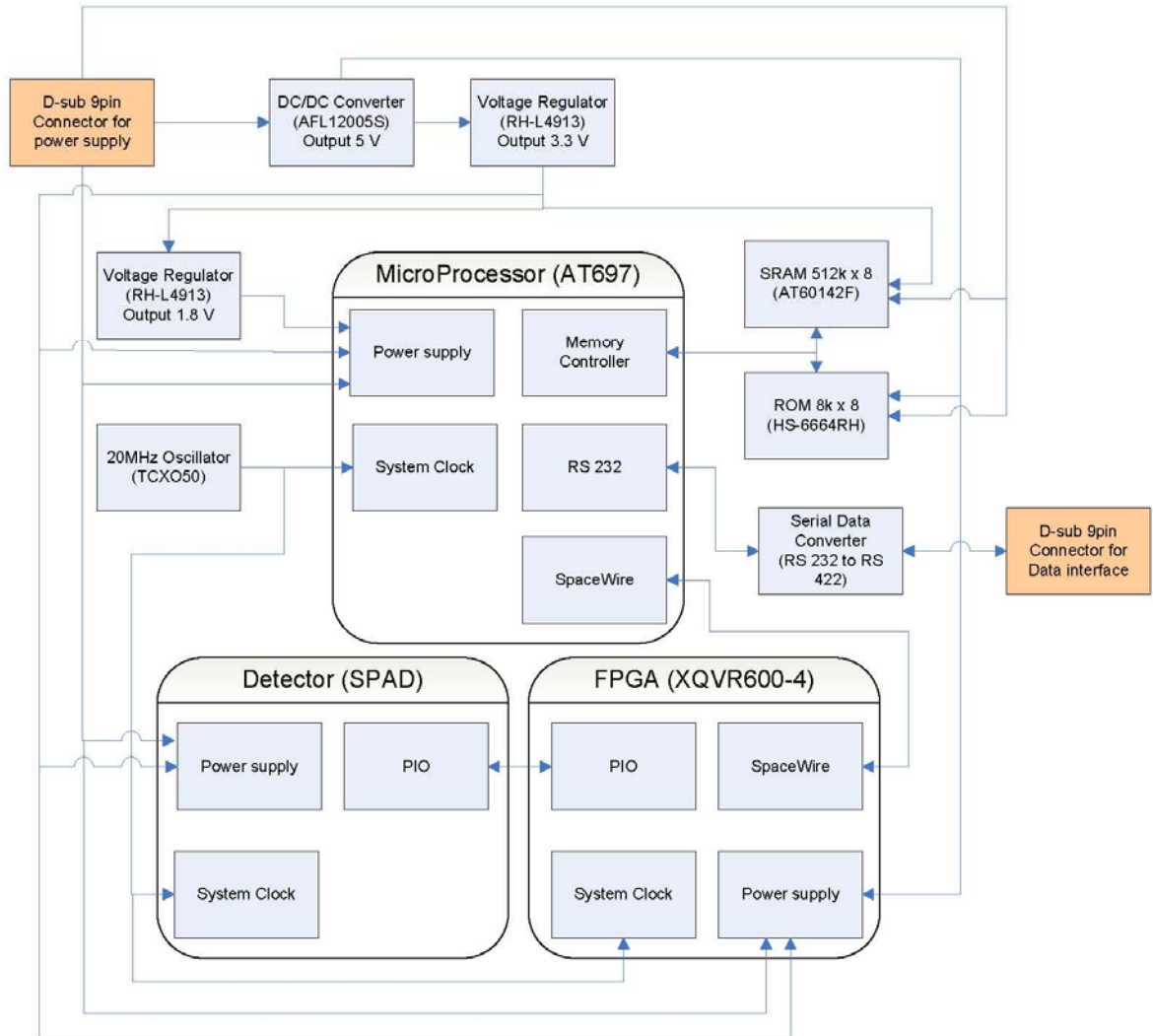
Figure 47: Preliminary design of the electronic circuit for the ES.

5.6   Single-Photon Avalanche Diode (SPAD)

5.6.1   The Single-Photon Avalanche Diode

5.6.1.1   SPAD Operation and Physical Principle

Sensors based on solid-state Avalanche Photo Diodes (APDs) have been proposed decades ago to simultaneously achieve high sensitivity and dynamic range, and low timing uncertainty. In APDs, carriers generated by the absorption of a photon in the p-n junction, are multiplied by impact ionization thus producing an avalanche. APDs can reach timing uncertainties as low as a few tens of picoseconds, thanks to the speed at which an avalanche evolves from the initial carrier pair forming in the multiplication region.

An APD is implemented as photodiode reverse biased near or above breakdown, where it exhibits optical gains greater than one. When an APD is biased below breakdown it is known as *proportional or linear* APD. It can be used to detect clusters of photons and to determine their energy. When biased above breakdown, the optical gain becomes virtually infinite. Thus, with a relatively simple ancillary electronics, the APD becomes capable of detecting single photons. The APD operating in this regime, known as Geiger mode of operation, is called *single-photon avalanche diode* (SPAD).

In 2003 the integration of linear and Geiger mode APDs in a low-cost CMOS process has become feasible. PEB prevention is accomplished forcing the electric field everywhere to be lower than that on the planar multiplication region, where it should be uniform.

Figure 48 shows some of the most used structures. In a) the n+ layer maximizes the electric field in the middle of the diode. In b) a lightly doped p- implant reduces the electric field at the edge of the p+ implant. In c) a floating p implant locally increases the breakdown voltage. With a polysilicon gate one can further extend the depletion region (gray line in the figure). The figure also shows a 3D cross-section of b) including a p-substrate and an n-well isolation.
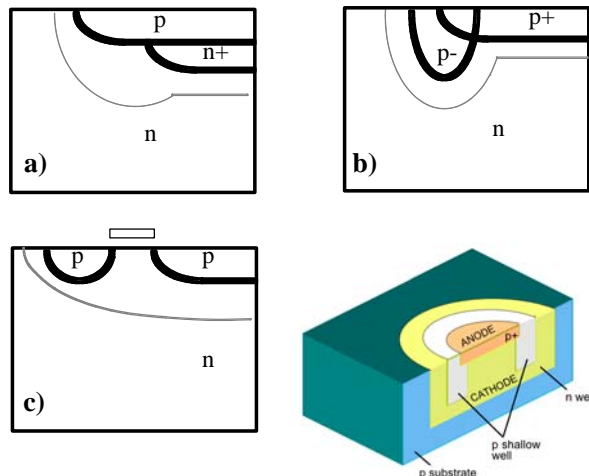
Figure 48: Techniques for prevention of premature edge breakdown (PEB) in planar processes.

Modern imaging processes provide several lightly doped implants at three or more depths. Thus, an optimal layer combination (p+/p-/n-well) generally exists that can yield a good trade-off between timing uncertainty and noise. However, care should be used so as to avoid full depletion of the well and punch-through's between shallow tubs and substrate. Buried layers should also be used with care to prevent punch-through across the n-well.

The operation principle of a SPAD operating in passive quenching and passive recharge (as implemented in this project) is described as follows. Upon detection of a photon, an electron-hole pair is generated in the substrate near or at the depletion region of the pn junction. With a certain probability, known as photon detection probability (PDP), one of the two carriers will trigger an avalanche. The avalanche current will cause a drop in the voltage across the diode. This is generally accomplished via a ballast resistor placed on the anode or the cathode of the diode as shown in Figure 48. The detection of the avalanche can be accomplished by measuring the voltage across the ballast resistance or the current across a low- or zero-resistivity. Pulse shaping may be performed using a comparator or, as in this project, a properly designed inverter. In these cases, excess bias voltage V_e satisfies the equation $V_e = |V_{OP}| - V_{bd}$, where V_{bd} is the true breakdown voltage. The resistances can be implemented in polysilicon or using the non-linear characteristics of a biased PMOS or NMOS [15],[16].

Proportional APDs can potentially be read out using a conventional scheme similar to CMOS APD architectures. SPADs on the contrary, generate a digital pulse for each detected photon. To avoid missing photon counts, a pixel-level counter or time discriminator can be used. However, large counters are not desirable due to the fill factor loss and/or extra time required to perform a complete readout. A partial solution to this problem is the reduction of the counter resolution (ultimately 1 bit), requiring more frequent readouts and/or lower saturation. Another solution is to access every pixel independently but sequentially using a digital random access scheme.

5.6.1.2 SPAD Main Parameters

CMOS APDs are characterized by means of the same parameters of conventional photodiodes, except for an optical gain higher than one. APDs operating in Geiger mode on the contrary require a specific set of parameters.

Fill Factor

Due to the geometry of guard rings for PEB prevention, in SPADs the fill factor may be as low as 1%. Using modern readout techniques, fill factors of up to about 9% have been demonstrated. We have also demonstrated a fill factor reclaim ratio of 15 using commercial microlense arrays.

Dead Time

In passive quenching/recharge devices dead time is generally dominated by the recharge time, about 30-50ns, and it varies a few percentage points across the array as a function of temperature and process variability. This results in mild saturation non-uniformity and time variability.

Timing Jitter

In integrated SPADs jitter is limited from below by geometry and process technology considerations. In arrays of significant size, jitter generally degrades from 50ps to as much as several hundreds of picoseconds due to electrical path and electrical supply ripple. Techniques derived from memory design, such as non rail-to-rail readout and shielding should be exploited.

Photon Detection Probability

The sensitivity is characterized in SPADs by the photon detection probability (PDP) and it is the overall probability that an impinging photon triggers a digital pulse. PDP is dependent on temperature and excess bias voltage. A good pixel-to-pixel uniformity is generally observed. Based on on-going research, we expect that deep-submicron SPADs achieve up to 40-50% PDP. In more advanced deep-submicron processes, the multiplication region will move to the surface and will be thinner. Thus, sensitivity in shorter wavelengths will be reinforced.

Dark Count Rate

As mentioned earlier, DCR is a function of detector area. It is also a function of temperature and excess bias voltage. On a large chip, DCR may vary widely from a minimum of a few Hertz to a few kilohertz. Generally, noisy pixels are less than 1% of the array, depending upon the distribution of traps across the chip and the overall quality of the process. Hence, it is always a good practice to foresee means to shut off pixels either temporarily or permanently, depending on applications.

Afterpulsing

Afterpulses are the result of secondary avalanches related to earlier photon detections. In active recharge schemes, a minimum recharge time needs to be allocated to allow for single-photon detectors to recover from an avalanche, thus keeping afterpulsing probability below a threshold. Fewer impact ionizations and fewer traps can reduce this time.

Crosstalk

Crosstalk can be optical and electrical. In optical crosstalk, luminescence released by an avalanche elsewhere may cause avalanches. In electrical crosstalk, a carrier generated elsewhere may trigger avalanches. The techniques for preventing optical crosstalk include optical shields between pixels. Electrical crosstalk is strongly reduced insulating the multiplication region, for example, with a well. The drawback of this approach is the reduction of fill factor and/or the increase of overall pitch.

5.6.2   Imager Chip Concept and Mode of Operation

The core of the chip consists of an array of 128x128 pixels each of which contains a Single Photon Avalanche Diode and its control electronics. The content of the array can be read out using a rolling shutter approach as depicted in Figure 49.

The 128 rows of pixels are sequentially activated by an address decoding system. The currently addressed row gets the right to write its content onto the output bus while all other rows are electrically disconnected.
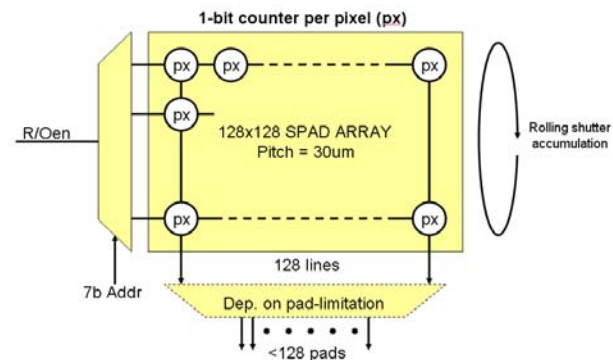
Figure 49: Diagram of the system's architecture.

Figure 50 shows the readout scheme of a single row.
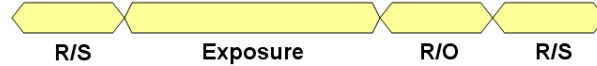
Figure 50: Basic steps of a row's single readout sequence.

The sequence of operations needed to correctly read out a single row of pixels consists of reset, exposure, and readout. After an initial reset cycle, all the rows are sequentially read out ad then reset. The integration time thus becomes the time interval between two consecutive resets of the same row multiplied by the number of exposures.

The chip can be operated in two different modes, namely Time-Uncorrelated Photon Detection (TUPD) and Time-Correlated Single Photon Counting (TCSPC).

5.6.2.1   Time-Uncorrelated Photon Detection Mode

In this operation mode pixels act as event-driven 1-bit in-pixel memory cells. The cells may be electrically set and reset independently on the pixel-by-pixel basis. A photon can only set an in-pixel memory cell. The output of the in-pixel memory cell, when polled by the appropriate command signals, is transferred to the exterior of the array by pulling down the voltage level of the column. Detecting this low level and recording the information is a responsibility of downstream electronics. See the sub-section 5.6.4 devoted to the pixel for implementation details.

5.6.2.2   Time-Correlated Single Photon Counting Mode

In this mode the in-pixel memory cell is bypassed and the detector is directly connected to its output line. The detector will respond with a voltage pulse every time it detects a photon, thus allowing for real time measurement on photons arrival times and time-of-flight applications.

5.6.3   Design Requirements

The main requirements on the SPADs for AIRES are summarised in TABLE 8.

TABLE 8: REQUIREMENTS ON THE SPAD FOR THE AIRES APPLICATION

Parameter	Specification	Final Design
Technology	0.35um CMOS	0.35um CMOS
Array size (sqpixels)	128 x 128	128 x 128
Size of the active spot of a pixel	6 – 9 µm	6.4 µm
Pixel pitch	≥ 30 µm	30 µm
Integration time	< 0.05 s (LEO)	0.02 s (LEO)
	< 0.5 s (GEO)	0.5 s (GEO)
Fill-factor	≥ 0.035	0.035
Photon detection probability	≥ 0.04	-
Maximum number of counts per pixel and second	≥ 6400 counts/pixel/s	-
DCR (time varying component)	< 17 Hz at 23 °C	-
DCR (Median)	280 Hz	-

5.6.4   Pixel Implementation

5.6.4.1   Architectural Description

This section describes the electronic circuit which has been integrated inside the pixel. The function of each block will be highlighted and the effect of the input signals on the behaviour of the pixels will be explained.
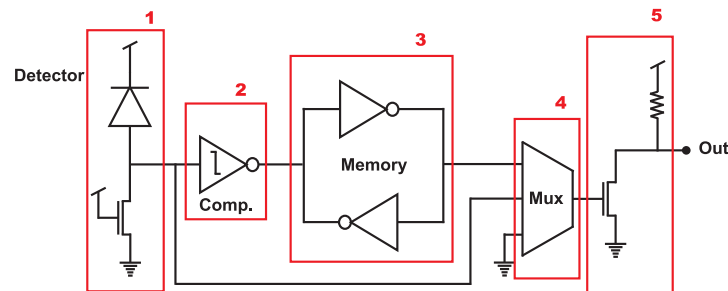
Figure 51: Block diagram of the pixel.

Figure 51 shows the block diagram of the pixel. Each block is briefly described hereafter.

1. The diode representing the SPAD must be reverse biased above breakdown. The SPAD must also be connected to a resistive device whose task is to quench the avalanches that are triggered by photon impacts. This device has been indicated by a transistor.

2. The comparator stage senses the spike pulse generated by the SPAD's anode and produces a clean digital pulse. Secondly, it provides an insulation layer that shields and protects the anode. This shielding is very important because additional capacitances or injected charges at this node could dramatically degrade the overall performance of the detector.

3. The 1-bit memory block has been designed to have an event-driven set state and an independent reset. The trigger that sets the memory is the high-to-low signal produced by the comparator. Then the memory stays in its set state to flag that at least a photon has been detected. The reset of the cell is issued by an external signal (not shown here).

4. The output multiplexer switches from TUPD mode to TCSPC. TUPD mode is selected if the output stage is driven by the signal produced by the memory block, while TCSPC mode is selected if the output stage is directly driven by the detector. This stage also offers the option to disconnect the pixel from the output line, thus implementing a very simple bus mastering system.

5. The output stage must be able to drive the output line and to send the pixel's content to the chip's periphery via a pull down transistor.

5.6.4.2   Pixel Schematic

Details on the pixel schematic design can be found in the SPAD design report.

5.6.4.3   Circuit Operation

The pixel is controlled by five external signals.

- MOD1 selects TUPD mode.

- MOD2 selects TCSPC mode.

- OEN disconnects the pixel from the output bus.

- RS and RSN handle the reset of the memory block and they are always each other's complement.

The following table summarizes the pixel's operating modes. The table shows how the control switches are configured in each mode. The state XX denotes a "don't care" condition.

MODE	M11 (MOD1)	M12 (MOD2)	M13 (OEN)	M10 (RS)	M4 (RSN)
TUPD	ON	OFF	OFF	OFF	ON
TUPD (reset)	ON	OFF	OFF	ON	OFF
TCSPC	OFF	ON	OFF	XX	XX
OFF	OFF	OFF	ON	XX	XX

5.6.4.4   Parasitics

Parasitics were assessed, details can be found in the SPAD Design Report.

5.6.5   The Implementation of the Chip

5.6.5.1   Chip Block Diagram

Figure 52 represents a block diagram of the entire chip. The input stage is made of an address decoding system and a control signal generator. These two blocks share the responsibility to read the commands of the user and control the detector array accordingly.

The output stage is made of a multiplexer that connects the 128 output lines of the detector array to the 64 output pads.
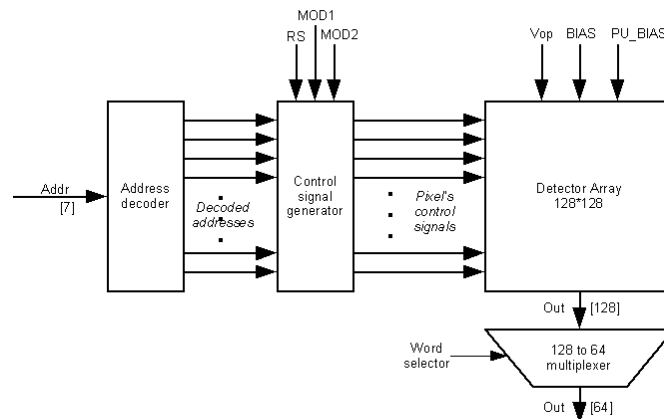
Figure 52: Chip block diagram.

Input Decoder.

The address decoding system is implemented as a simple 7 to 128 decoder. The complete decoder is implemented by hierarchical interconnection of 3 to 8 decoders with enable signals. This stage is designed so that only the pixel row corresponding to the input code is addressed. In this way each 7 bit code uniquely represents each row of pixels and allows its activation.

Control Signal Generator

The pixels have some special requirements on the control signals. Failing to meet all requirements will hinder the functionality of the pixel and possibly lead to permanent damage. In order to avoid unwanted combinations of the pixel's control signals, a simple array of 128 row controllers has been implemented.

Each controller reads three user controlled signals (MOD1, MOD2 and RS, all active low) and the output line of the decoder corresponding to its row and generates the complete set of signal for its row's pixels. The behaviour of the controller is summarized below.

- If the row is not addressed, then the block will disconnect the row from the output bus.

- If the row is addressed and just MOD1 is asserted (low), then all the row's pixels are put in TUPD mode.

- If the row is addressed and just MOD2 is asserted (low), then all the row's pixels are put in TCSPC mode.

- If the row is addressed and just RS is asserted (low), then all the row's pixels are reset.

- If the row is addressed and no one among the control signals is asserted (low) or more than one is asserted (low), then just OEN will be kept asserted to disconnect the row from the output bus.

- Anyway, the controller will guarantee that RS and RSN will always be each other's complement.

The power supplies of the output buffers are not connected to the global VDD and GND signals. They can be tuned externally in order to calibrate the high and the low voltage level of each control signal.

Sensor Array and Output Multiplexer

The sensor consists of an array of 128x128 pixels. The rows of pixels are driven by the controller that is described in the previous section. Each of the 128 output lines has been equipped with a PMOS pull up transistor placed outside of the array. This transistor is the electrical counterpart of each pixel's output transistor. The output bus is then sent to a 128 to 64 multiplexer. This component has bee designed to be as simple as possible. Both signal N and signal N+64 ($0 \leq N \leq 63$) are connected to the same output pad. Access control is guaranteed by the presence of three state buffers.

Three additional bias lines contribute to the circuit's controllability.

- V_{OP}. This is the voltage that must be applied to every SPAD's cathode to bias them in Geiger mode. A tolerance of 10% is imposed upon this voltage.

- **BIAS**. This is the voltage applied to the quenching transistor's gate. It affects the circuit's performance by acting on the characteristics of the avalanche and its control.

- **PU_BIAS**. This voltage is applied to the pull up transistors of the output lines and ultimately controls the resistance of the component.

Bypass Integrated Capacitors

An array of MOS transistors used as capacitors and connected between VDD and GND has been integrated. The array provides a total capacitance of 2nF and it should be enough to mitigate eventual voltage ripples or small drops on the power supplies. MOS transistors were chosen in order to take advantage of the high capacitance across the thin gate oxide.

5.6.6   Pixel and Chip Layout.

5.6.6.1   Pixel Layout

Figure 53 shows an overview of the pixel's layout. Its design had to satisfy some application-specific critical requirements that heavily affected the final implementation of the system. The most critical requirements were the fixed pitch, the fixed detector size, the required FOV of at least 45 degrees, the design rules set, and the radiation insensitiveness that is required for space applications.

More details on these requirements can be found in the SPAD Design Report.
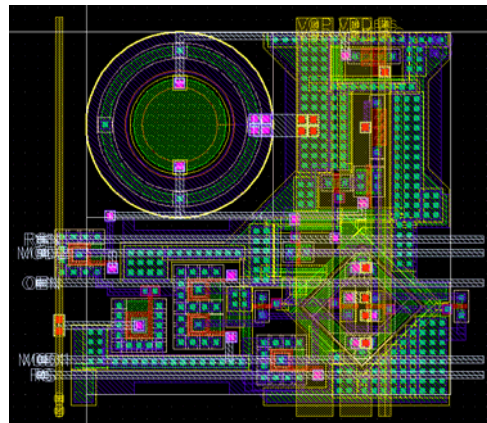
Figure 53: The layout of the pixel.

Low Cost Earth Sensor based on Oxygen
Airglow – Final Report

ESA Contract #20267/06/NL/JA
Issue: 1   Review: 5
Date: 29/08/08
Page: 53 of 88
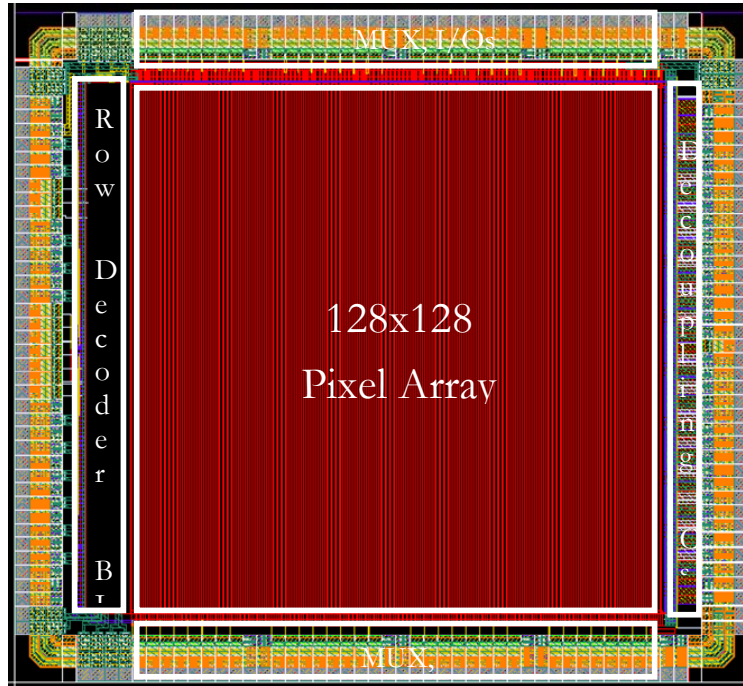
5.6.6.2   Chip Layout

Figure 54: Sensor chip layout.

5.6.7   Timing Diagrams

The following figures show the functional diagrams of the input/output ports of the sensor chip.

In TUPD mode it is necessary to implement the complete readout sequence that is shown in the following picture. Simulations performed on the model of the pixel show that the reset pulse should start at least 10ns after the application of the address. The minimum pulse duration has been estimated to 20ns. Every other signal should not be time critical. The minimum working period is dictated by the peripheral pads and by the detector's dead time. This time is sufficiently large to accommodate the setup and hold time of every signal in the circuit.
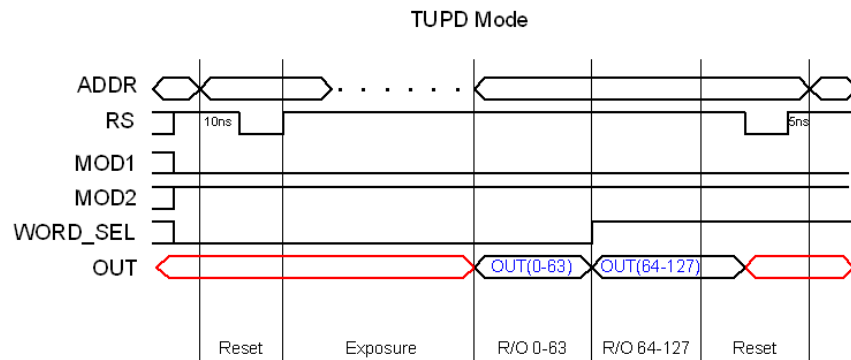
Figure 55: Diagram of TUPD mode.

The reset signal is unused in TCSPC mode. In this mode the delay introduced by the output multiplexer during the commutation of WORD_SEL has been estimated to be approximately 5ns.
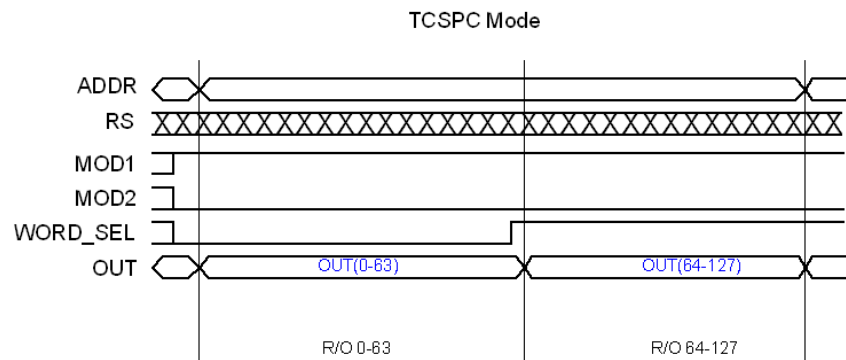
Figure 56: Diagram of TCSPC mode.

5.6.8   RADHARD2 Addendum

The design of RADHARD2 was influenced and inspired by the design of RADHARD. Indeed, the differences between the two designs were minimised, especially in those functional areas where RADHARD proved to perform well. This chapter does not present the complete design, for details, we refer to the RADHARD design document. The remainder of this chapter identifies the main differences between the two designs. A short summary of these differences can be found hereafter.

Array size

RADHARD2 features a sensor matrix of 32x32 pixels instead of 128x128. The down-scaling of the sensor was driven both by total cost considerations and by the simplicity of read and control operations that such a small array can provide. All other design requirements and constraints (including the pixel pitch) remained untouched.

Test pixel

A test pixel has been implemented outside the array. This test pixel is provided with voltage probes to read the logic values of every relevant internal node. These probes are directly connected to dedicated output pads for easy inspection.

Enhanced pixel controllability

1-bit memory cells in RADHARD2 are individually settable and resettable. A double addressing scheme (row-wise and column-wise) has been implemented to grant complete read/write access to each of the 1024 memories in the array.

Control and readout scheme

The control and readout scheme have been simplified. The input stage is now clocked and buffered to guarantee that the input signals are applied to the array synchronized and with the

correct timing. The output multiplexer has been removed due to the lower number of output lines. In RADHARD2 all the lines are directly connected to dedicated output pads.

5.6.8.1   RADHARD2 pixel design

The RADHARD2 pixel design is basically a rework of the RADHARD pixel. Only three modifications were made:

1. The transistors of the output block were rewired so as to limit the detrimental effects of a potential leakage of the output enable device. Now the pixel selector device and the output transistor are connected in series.

2. A 2-transistors branch is added to the input of the memory cell. Those transistors implement the individual set of the memory. In order to avoid current leakage on that branch, both transistors were implemented as radiation-hardened Gate All Around devices.

3. The NMOS input comparator has been replaced with a simpler pull-down branch that provides the same functionality and prevents the inefficiencies that are inherent in NMOS inverters (static power, asymmetric edges, …).

The aforementioned modifications have been highlighted in the schematic capture shown in Figure 57.
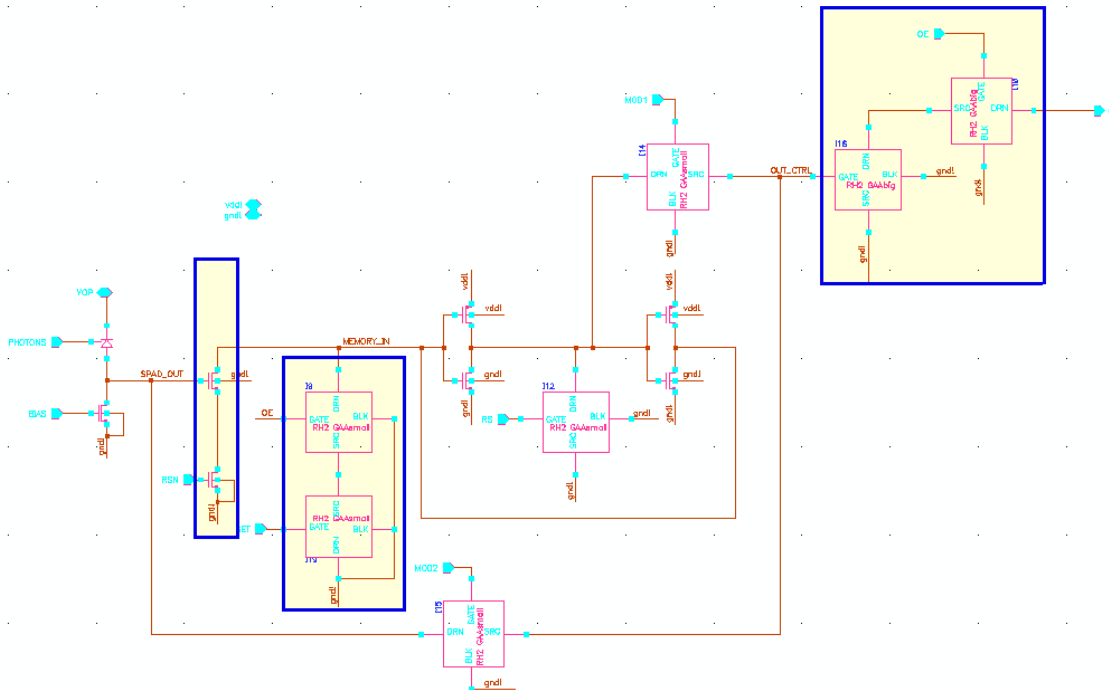
Figure 57: RADHARD2 pixel schematic.

The GAAsmall and GAAbig component used in this schematic are just utility models that have been defined in order to encapsulate the radiation-hardened Gate All Around transistors.

Low Cost Earth Sensor based on Oxygen
Airglow – Final Report

ESA Contract #20267/06/NL/JA
Issue: 1   Review: 5
Date: 29/08/08
Page: 56 of 88

The layout view of the pixel follows the same criterion of similarity and consistency with RADHARD. Some minor modifications were made to optimize and clean up the layout. An example is the design and implementation of an octagonal NWELL. This shape allowed us to ease the placement and routing of devices, and to maximize the distance between the NWELL and each SPAD (a major source of trouble among all the design rules).

Figure 58 is a representation of the layout of the RADHARD2 pixel. Minor modifications in the routing proved to be necessary due to the presence of an additional signal line (the pixel selector for the memory set operation) and a rethought device placement.
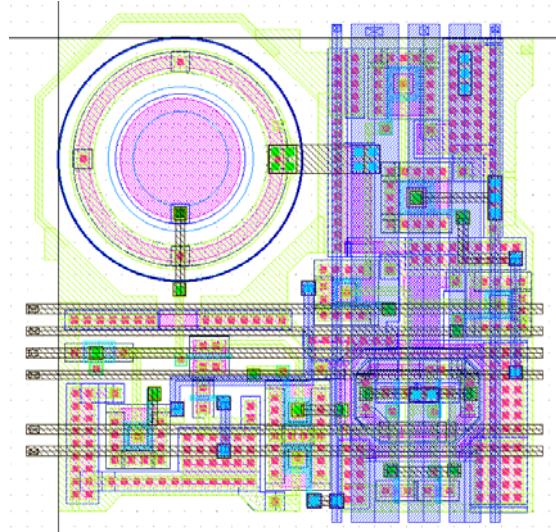
Figure 58: Layout of the RADHARD2 pixel.

5.6.8.2   Input and output interface

The input stage has been slightly modified in order to reflect the new dimension and protocol of the chip and to take advantage of some design improvements. RADHARD2 input stage is made of 3 consecutive blocks:

1. A 5-to-32 address decoder with enable signal that determines which row of pixels should be currently active.

2. A flip-flop stage to buffer the output of the decoder. This stage is useful to insulate the following stages from the eventual glitches that the decoder may produce when switching from one address to another.

3. A signal generator stage that produces the row reset and row enable signals according to user's preferences (i.e. the reset flag and the output of the corresponding flip-flop).

The design of the decoder took advantage of the same hierarchical structure that was implemented in RADHARD. The flip-flop stage is a simple array of flip-flops that buffers the output of the decoder. The signal generator is very simple, but it may deserve a short explanation. Its task is to generate the reset signal that erases the memories embedded in the current row's pixels, the complement of the reset signal (whose purpose is inherited from RADHARD), and the pixel output enable signal. It is designed to be balanced (all signal paths present the same number of logic stages) and to provide enough current to be able to drive the portion of the pixel array that falls under its control.

A second 5-to-32 decoder with enable signal (plus flip-flop stage) has been implemented to perform column selection. The combined action of the two decoders allows the setting of the memory of the currently addressed pixel. The output stage has been completely removed. All the 32 output lines of RADHARD2 pixel array could fit in the pad ring, so no output multiplexer or access control system is needed anymore. Every output line is directly connected to a dedicated output pad. This reflects directly on the readout scheme, as it's not necessary anymore to perform a two-step acquisition to get the data of a single row of pixels.

5.6.8.3   Signal list and operation protocol

The only peculiarity that distinguishes the set of I/O signals of RADHARD2 from the set of I/O signals of RADHARD is that in the new chip all the signals are active high.

5.6.9 General Performance

RADHARD2 was tested prior and after irradiation. An annealing phase was also performed and the chip was tested after that phase. TABLE 9 lists all salient parameters for this design. The chip was tested at a range of temperatures from -40 to 40ºC. The breakdown voltage was determined in this range of temperatures so as to enable us to extract the value of Ve from VOP.

Parameter	Specification	Final Design
Technology	0.35um CMOS	0.35um CMOS
Array size (sqpixels)	32 x 32	32 x 32
Size of the active spot of a pixel	6 – 9 µm	6 µm
Pixel pitch	≥ 30 µm	30 µm
Integration time	< 0.05 s (LEO)	0.02 s (LEO)
	< 0.5 s (GEO)	0.5 s (GEO)
Fill-factor	≥ 0.035	0.035
Photon detection probability	≥ 0.04	0.05
Maximum number of counts per pixel and second	≥ 6400 counts/pixel/s	833,000 counts/pixel/s
DCR (time varying component)	< 17 Hz at 23 °C	-
DCR (Median)	280 Hz	140 Hz

TABLE 9. performance summary for RADHARD2.

The fastest readout cycle we tested was 1.2µs, however, higher speeds may be attainable with alternative motherboards and/or higher power dissipation. The median DCR was lower than expected and did not vary significantly across dies and after irradiation.

Figure 59 shows a plot of the average PDP of RADHARD2 in the visible spectrum. The response tracks very closely the performance reported in [17].

TABLE 10 lists the behavior of the breakdown voltage before and after Gamma irradiation and proton bombardment.
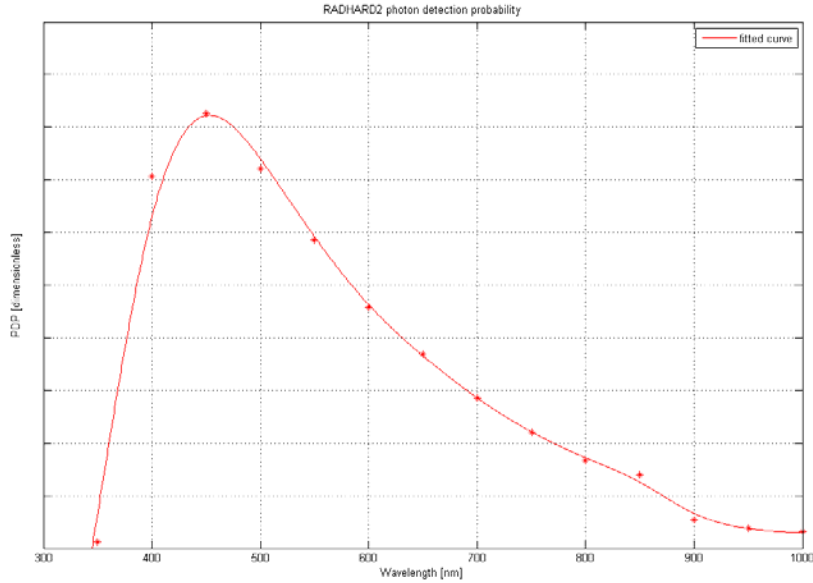
Figure 59. PDP as a function of wavelength.

Mode	-40C	-20C	0C	+20C	+40C
Pre-Gamma	19.08	19.12	19.40	19.42	19.67
Post-Gamma	18.84	18.94	19.12	19.42	19.64
Pre-proton (11MeV)	18.80	18.95	19.05	19.21	*19.12*
Post-proton (11MeV)	18.01	18.52	18.87	19.27	19.78
Pre-proton (60MeV)	18.66	18.74	18.90	19.25	*19.07*
Post-proton (60MeV)	18.51	*18.45*	18.70	19.03	19.14

TABLE 10. Breakdown voltage evolution.

5.6.10 Gamma Radiation Testing

The chip was irradiated in the ESA ESTEC Co60 facility for 3 days to reach a total dose of 42kRADs (H_2O). While PDP and breakdown voltage remained unchanged across the chip, the DCR median increased by 8% at the end of the irradiation. Figure 60 shows a plot of the evolution of the DCR median over the entire irradiation period.
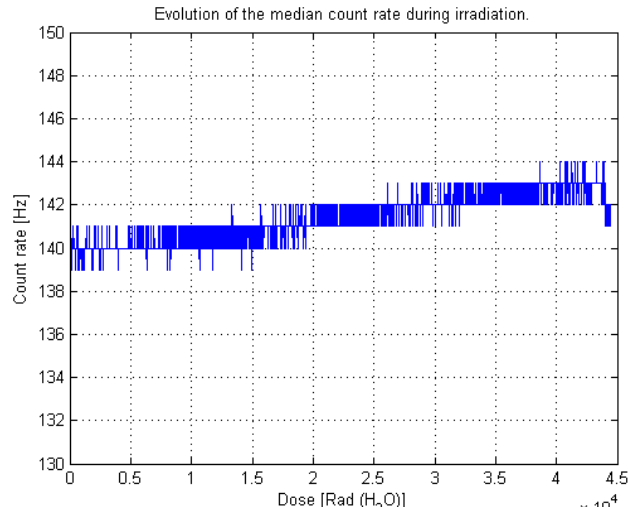
Figure 60. Median DCR during gamma irradiation.

After irradiation the chip was annealed for 5 days at 125°C at LMTS facility in Neuchâtel. While no significant improvement was observed in the median, the worst performing pixels returned to pre-irradiation DCR. The sensor daughterboard was equipped with a C-mount box so as to enable us to image real scenes. Figure 61 shows the setup built at EPFL BM workshop.

Figure 61. C-mount setup for RADHARD2.

5.6.11 Proton Bombardment

Two unirradiated chips were bombarded with a proton stream at the Paul Scherrer Institut (PSI) in Villigen, Switzerland. The chips were exposed for 50 minutes to 11 MeV and 60 MeV proton beams, respectively. The stream was estimated by PSI to be about 2×10^7 p/cm^2/s, hence the total dose per chip was higher than 6.0×10^8 protons. The session was completed in one day on 10/05/2008, while PSI rules required that the chips be left on the premises until radiation levels

could reach safe levels. This required 4 days for the chip bombarded at 11MeV (chip released on May 14th) and 3 weeks for the chip bombarded at 60MeV (chip released on May 30th).

Tests were conducted before and after bombardment. The median and mean DCR was monitored during bombardment. Figure 62 shows a plot of the DCR median evolution during the experiment for 11MeV. The median DCR increased from 140Hz (before bombardment) to 7.8kHz (at the end of the session). Note that at times the DCR falls to near zero as the readout circuitry briefly failed to function properly. The causes of this behavior are being investigated.

After bombardment the chip was annealed for 5 days at room temperature. While no significant improvement was observed in the median, the worst performing pixels returned to pre-bombardment DCR levels.
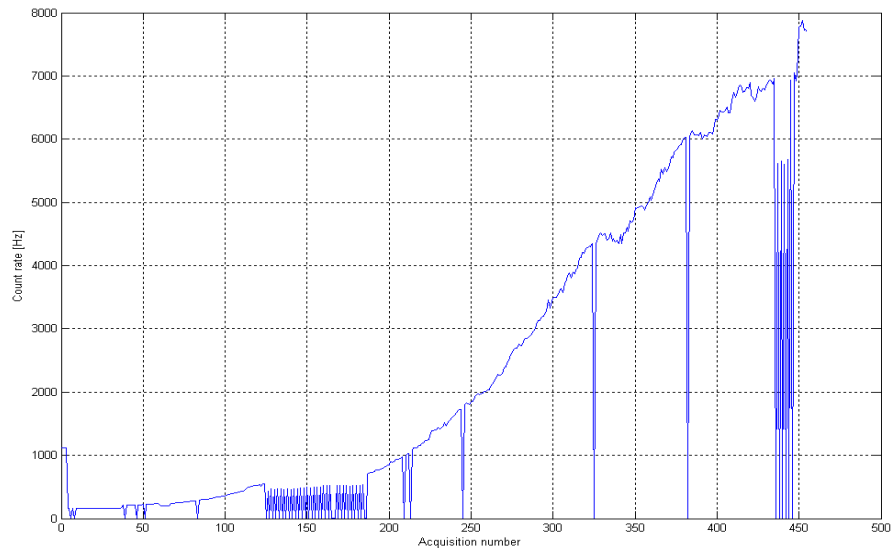
Figure 62. Median DCR during proton bombardment at 11MeV.

Figure 63 shows a plot of the DCR median evolution during the experiment for 60MeV. The median DCR increased from 140Hz (before bombardment) to 10kHz (at the end of the session). Note that at times the DCR falls to near zero or exceeds the scale as the readout circuitry briefly failed to function properly. The causes of this behavior are being investigated.

After bombardment the chip was annealed for 20 days at room temperature. While no significant improvement was observed in the median, the worst performing pixels returned to pre-bombardment DCR levels.
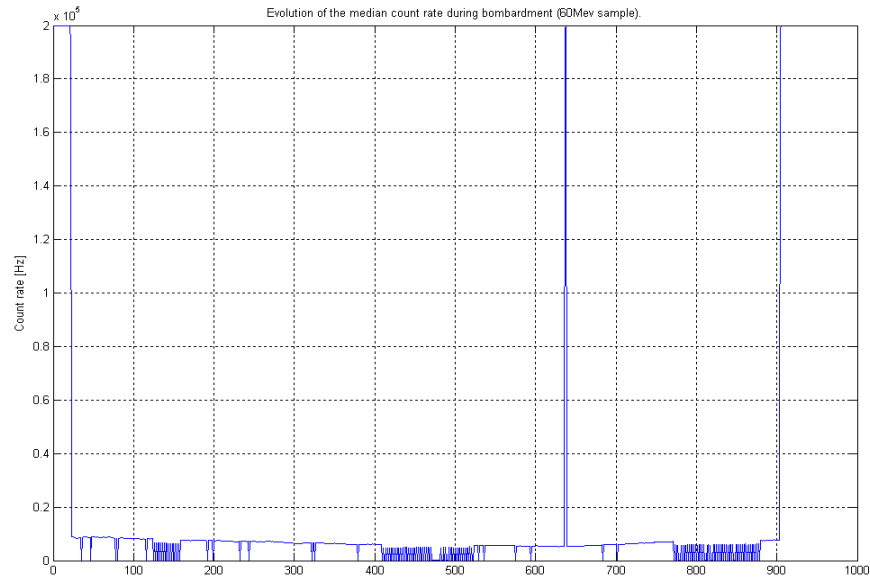
Figure 63. Median DCR during proton bombardment at 60MeV.

5.7   Algorithm

The function of the algorithm is to determine the earth vector with images of the airglow. It consists of two main phases:

- the pre-processing phase, where different filters can be applied to the raw image in order to increase the visibility of the interesting features

- the segmentation phase, where the pre-processed image is analysed and the earth vector is extracted.

5.7.1   Image Pre-Processing

The main objective of the image pre-processing is to suppress information that is not relevant to the specific image analysis task in order to reduce the processing load and increase the accuracy of the segmentation algorithm. It is an improvement of the image data that enhances those image features important for the image segmentation. In our applications, the image pre-processing filters the noise due to dark signal and detects edges. The three different steps of image pre-processing are described in paragraph 5.7.1.1 to 5.7.1.3.

5.7.1.1   Thresholding

The first pre-processing step consists of thresholding the raw image. It reduces the amount of data to be processed by compressing the dynamic range and noise: Since the pixels capturing airglow emission at limb and most of the pixels capturing airglow at zenith will be saturated, a simple threshold can be applied to the image to reduce a big part of the noise. This threshold defines all values that do not correspond to a saturated pixel as black (0) and all other pixels as white (1). The images before and after thresholding are presented in Figure 64.

(a)   (b)
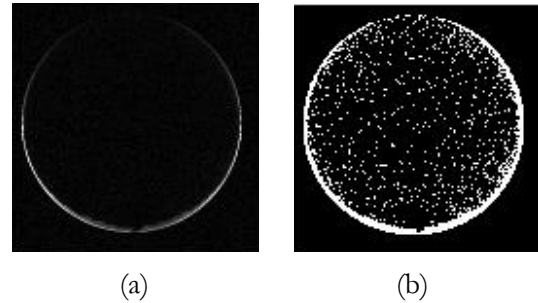
Figure 64: (a) Raw image of the airglow. (b) Image after thresholding.

5.7.1.2   Smoothing filter

The second step of the image pre-processing phase consists of smoothing the image in order to suppress image noise and to further reduce the amount of data to be processed. The implemented smoothing algorithm is called erosion and thins out light structures: as soon as all pixels in the neighbourhood (N^*) of a central pixel are dark, the central point becomes dark as well.

Figure 65: Neighbourhood of a pixel.

The neighbourhood of a pixel has been defined as shown in Figure 65. The filter has been chosen because of its simplicity. Figure 65 shows the effect of the implemented 3 x 3 erosion filter.

$$g_e(x^*, y^*) = min\left\{g_i(x, y)/(x, y) \in N^*\right\}$$

(a)   (b)
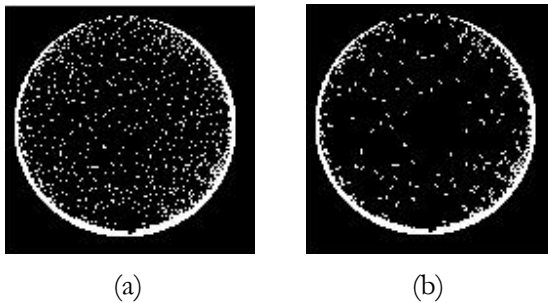
Figure 66: (a) Image after thresholding. (b) Image after erosion.

5.7.1.3   Intensity gradient filter

The last step of the image pre-processing algorithm increases the visibility of those features which help determining the earth vector, namely the limb of the earth. Thus, an edge detection algorithm is applied. The implemented edge detection filter is based on the Canny method which finds edges by looking for local maxima of the gradient which is calculated using the second derivative of a

(a)   (b)

**Low Cost Earth Sensor based on Oxygen
Airglow – Final Report**

ESA Contract #20267/06/NL/JA
Issue: 1   Review: 5
Date: 29/08/08
Page: 63 of 88
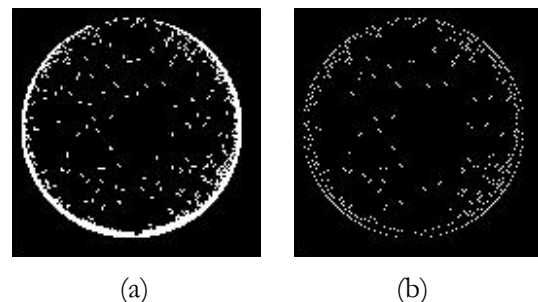
Gaussian filter. The effect of the Canny method is
shown in Figure 67.

**Figure 67: (a) Image after erosion. (b) Image after
edge detection with Canny filter.**

5.7.2   Image Segmentation

The task of the image segmentation phase is to
analyse the processed image data in order to find
the image parts that have the strongest correlation
with a circle (which is the object of interest our
application). The main issue for circle fitting
algorithms is the robustness against the occurrence
of artefacts, i.e. a number of points in the input not
belonging to the earth limb. The reason for these
artefacts may be noise, the moon, straylight or
detector defects. Another important issue are CPU
and memory needs for computation.

(a)   (b)
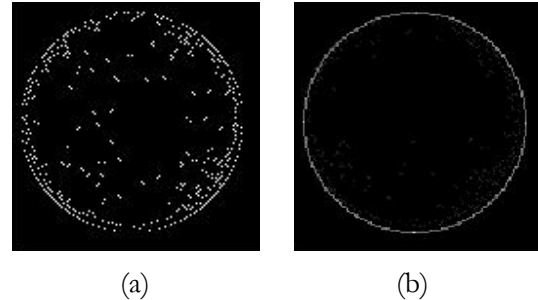
**Figure 68: (a) Image after edge detection with
Canny filter. (b) Image after Segmentation with
the Hough transform.**

The implemented curve fitting algorithm is based on the Hough algorithm, which provides a very
simple and effective method for centre finding since it is not too sensitive to imperfect data or
noise.

The task of the Hough transform is to find a bright circle of unknown radius r in the pre-
processed image as shown on the right side of Figure 68. The method starts with a search for
bright image pixels; for each of these pixels found, a locus of potential centre points of the circle
associated with it can be determined. Such a locus of potential centre points forms a circle with a
radius r_i as demonstrated in Figure 69. If the loci of potential circle centres are constructed for all
bright pixels identified in the pre-processed image and for all possible radius within the radius
range of interest, the frequency with which each pixel of the image space occurs as an element of
the circle-centre loci can be determined. As seen in Figure 69.c the true centre of the circle being
sought is represented by the pixel with the highest frequency of occurrence in the circle-centre
loci.
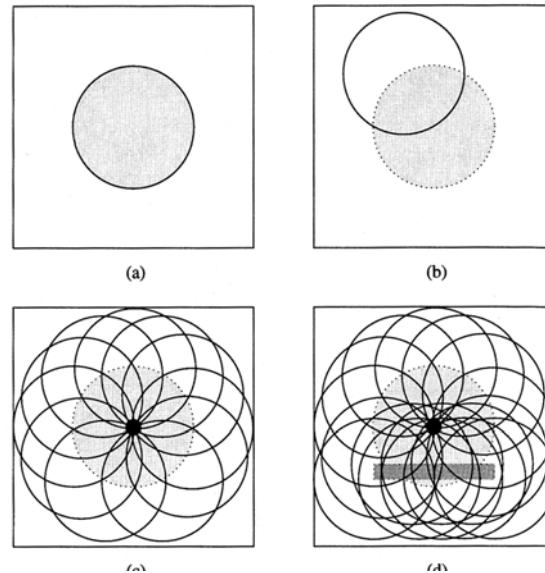
Figure 69: Hough transform for circle detection: (a) Pre-processed image. (b) For each pixel on the circle, a potential circle-centre locus is defined by a circle with radius r_i and centre at that pixel. (c) The frequency with which image pixels occur in the circle-centre loci is determined – the highest frequency pixel represents the centre of circle (marked by •). (d) The Hough transform correctly detects the circle (marked by •) in the presence of incomplete circle information and overlapping structures.

Since for the earth acquisition phase neither the radius nor the position of the circle centre to search for is known a-priori, a huge accumulator array would be required to cover the whole zone of interest of the algorithm with just one iteration with the Hough algorithm. However, since the memory used on the ES instrument shall be as small as possible, an adaptive Hough algorithm, going from large to narrow scale is much more advantageous. Hence, the image segmentation algorithm has been split in two phases: the acquisition phase and the tracking phase.

5.7.2.1   Acquisition Phase

In *acquisition phase* the ES determines the earth vector based on a single measurement without taking into account previous observations. For this mode, the image processing is characterized by a bigger space of possible positions of the earth centre and the algorithm performs thus more iterations[3] with the Hough algorithm. The implemented iteration steps of the Hough algorithm are depicted in Figure 70. In order to allow for positions of the centre of the Earth that are outside the FOV of the detector, the accumulator array (i.e., Earth Center coverage area) used for the Hough algorithm covers twice the FOV of the detector of the ES. The processing time required to determine the earth vector in this phase takes more than 500 ms, and the desired update rate is 2 Hz, which is why a much faster tracking mode is used after initial acquisition.

---

[3] There are 3 iterations with the Hough algorithm in the implemented algorithm.

Low Cost Earth Sensor based on Oxygen
Airglow – Final Report
ESA Contract #20267/06/NL/JA
Issue: 1   Review: 5
Date: 29/08/08
Page: 65 of 88

5.7.2.2   Tracking Phase

In *tracking phase* the ES determines the earth vector based on the last measurement and previous X, Y outputs. The approximate position of the earth centre is known from previous measurements. Since the satellite movement is expected to be low (max rotation of $3°/s$, max speed 7.8 km/s for LEO application and $0.4°/s$, respectively 3.1 km/s for a GEO application), the new position of the earth centre will be close to its position during the previous measurement and the space defining the possible position of the earth centre is therefore smaller during this mode of operation. Thus, there will be one iteration with the Hough algorithm only and the image processing time is low enough to provide a new earth vector calculation every second as required (see Table 4 for a more detailed analysis on the algorithm run time for tracking phase). The Hough algorithm covers 12.5% of the FOV of the ES and a radius range of 1.5 pixels with a resolution of 0.5 pixels.

TABLE 11: **EARTH CENTER SEARCH COVERAGE AREA AND RESOLUTION
OF THE HOUGH ALGORITHM FOR THE 3 ITERATION STEPS DURING
ACQUISITION PHASE**

Algorithm iteration #	Area of coverage of the Accumulator Array (=Earth Center coverage area)	Resolution of the Accumulator Array
1	2 x FOV of the detector = 256 pixels radius range = 24 pixels	8 pixel
2	1/2 x FOV of the detector = 64 pixels radius range = 6 pixels	2 pixel
3	1/8 x FOV of the detector = 16 pixels radius range = 1.5 pixels	0.5 pixel
Total coverage of the Hough algorithm for the acquisition phase	2 x FOV of the detector = 256 pixels radius range = 24 pixels	0.5 pixel

Raw Image	Threshold	Erosion	Mexican Hat	Canny	Hough	
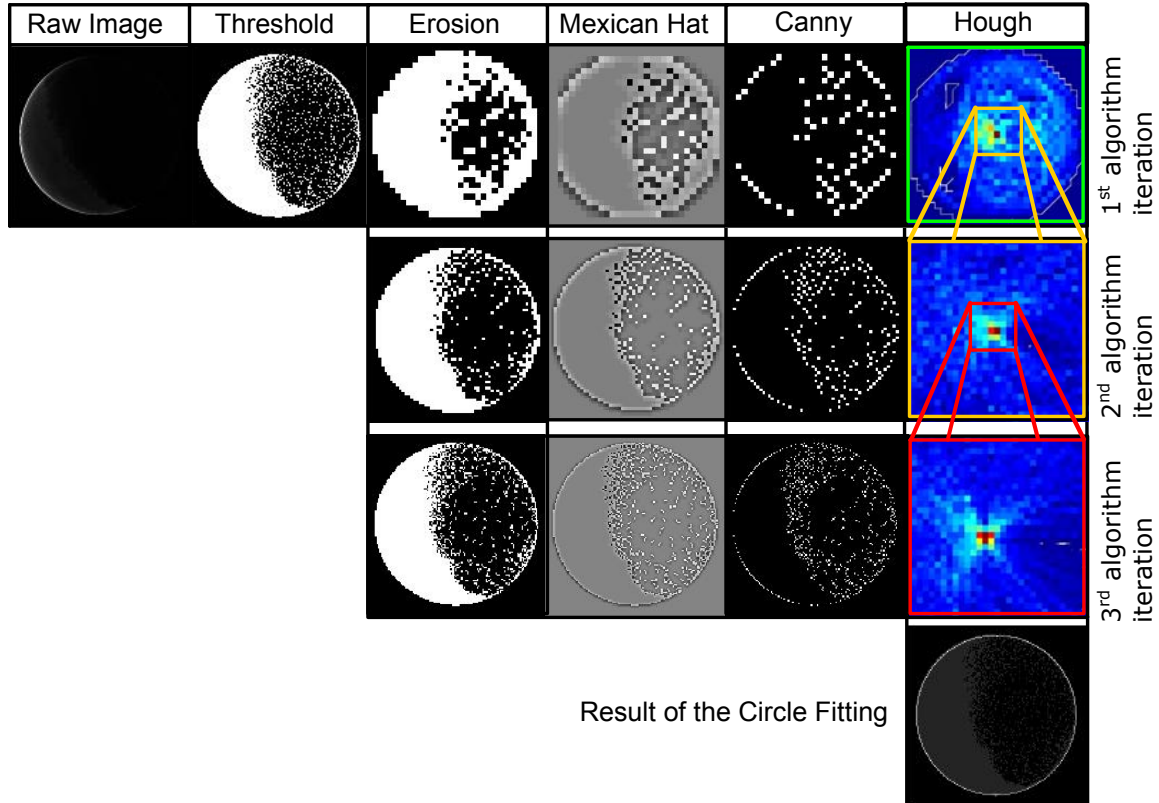
Figure 70: Iteration steps of the Hough algorithm for the acquisition phase.

5.7.3   Earth Presence Detection and Sun Blinding Recognition

As required in [1], an earth presence detection and a sun blinding recognition have been included in the algorithm. A simple way to do this is described below.

5.7.3.1   Sun Blinding Recognition

If the detector is blinded by the sun, there will be a much higher photon flux on the detector and more pixels will be saturated. The analysis of the percentage of the image which is saturated provides a simple way to identify if the sun affects the image and can be done before running the earth vector algorithm.

5.7.3.2   Earth Presence Detection

The Hough algorithm is the most robust during the first iteration step of the acquisition phase, since in this iteration the area in which the algorithm might find the earth centre covers all possible positions if the earth is within the FOV of the detector. Thus, the earth presence detection should be based on this iteration step only. If after the first iteration, an evident

maximum has been found, the earth presence flag can be activated. The level of confidence of this maximum has to be chosen carefully: whereas a high confidence level does not allow an earth presence detection if the airglow signal is too weak, an low confidence level activates the earth presence flag with random noise as well. A good compromise still has to be found.

5.8   Breadboard Testing

5.8.1   Test Objectives

An evaluation of the most promising algorithm was done in order to test the robustness of the earth sensor and to verify the following specifications:

TABLE 12: REQUIREMENTS ON THE ES ALGORITHM

Req. No	Description
F1	The earth sensor shall have the following capabilities: - Acquisition of earth by identification of its presence in the FOV. - Measurement of earth centre vector in two orthogonal directions. - Recognition of blinding by sun.
F2	The output of the ES shall be the X, Y position of the earth centre within the FOV, an earth presence flag and a sun blinding flag.
F3	The ES shall be capable of operating in the following orbits: - LEO with an orbital height varying between 200 and 2000 km - GEO with an orbital height varying between 35000 and 45000 km
P2	In GEO, the ES X, Y outputs measurements shall have a random error (noise) of less than 2.5 degrees 2 sigma. *Goal shall be 0.6 degrees 2 sigma.*
P3	The ES bias and long term stability in X and Y shall be less than 3 degrees over temperature and lifetime. *Goal shall be 1 degree.*
E1	The ES shall operate nominally with a mounting interface plane temperature set point in the range -30 to 40 degrees C. *Sensor will be mounted outside the s/c, nominally facing the earth.*

The performance metrics of the algorithms which have been tested are:

- Acquisition of earth by identification of its presence in the FOV
- Recognition of blinding by sun
- Angular accuracy of the X, Y output
- Stability in X, Y over temperature

The algorithm performance was tested as a function of the saturation intensity (image thresholding prior to erosion) and of the temperature of the detector.

The success criteria for the algorithm testing were:

- a mean error < 4.5 pixels (corresponding to a total error of 0.6°) for all measurements with the earth completely within the FOV

- a mean error < 19.5 pixels (corresponding to a total error of 2.5°) for the measurements with the earth only partially within the FOV

- an earth presence detection without failure

5.8.2   Breadboard Description

The breadboard consists of four main parts:

1. a computer displaying the earth appearance at 762 nm on a LCD display, operating the detector control electronics,

2. an optical system (including a filter and blocking lenses) to attenuate, to transmit and to focus the signal provided by the LCD display on the detector-array,

3. a detector-array and its control electronics to capture the image of the LCD display and to transmit the SPAD or APS output back to the computer.

4. an external computer running the image processing algorithms
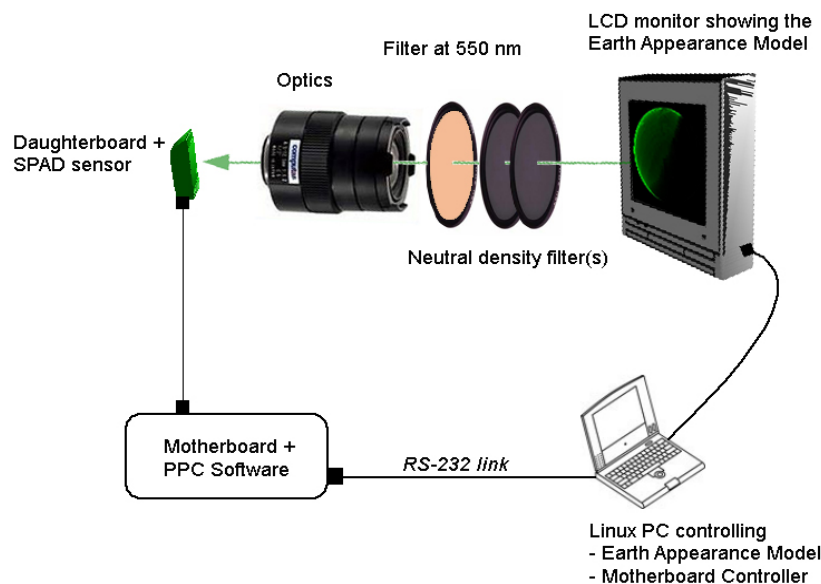
Figure 71: Schematic of the breadboard showing key elements

Detector choice: the algorithm testing was initially planned to be done with a custom-made 128 x 128 pixels SPAD array. However, in parallel with the development of such a detector array, a careful system study showed that a low noise APS detector such as the LCMS can provide better overall performance. Since the LCMS is the most promising candidate for the detector for this Earth Sensor, and since the 128x128 SPAD array was not available when expected, the LCMS was used as the detector in this breadboard to validate the algorithms, using only the central 128x128 pixels.

5.8.3   Raw Image Data and Image Pre-Processing

The test images are shown in Figure 72 and represent an observation of the airglow under the circumstances described in TABLE 13.

TABLE 13: TEST IMAGES USED FOR THE ALGORITHM TESTING

Parameter	Targeted Test Steps
Test image 1	min. airglow signal at night, earth centred, altitude 45000km
Test image 2	max. airglow signal at day, earth centred, altitude 45000km
Test image 3	mean airglow signal at twilight, earth centred, altitude 45000km
Test image 4	min. airglow signal at night, earth not centred, altitude 45000km
Test image 5	max. airglow signal at day, earth not centred, altitude 45000km
Test image 6	max. airglow signal at twilight, earth not centred, altitude 45000km
Test image 7	min. airglow signal at night, earth centred, altitude 35000km
Test image 8	max. airglow signal at day, earth centred, altitude 35000km
Test image 9	max. airglow signal at twilight, earth centred, altitude 35000km
Test image 10	min airglow signal at night, earth partially outside of the FOV, altitude 35000km
Test image 11	max airglow signal at day, earth partially outside of the FOV, altitude 35000km
Test image 12	max airglow signal at twilight, earth partially outside of the FOV, altitude 35000km

Images acquired with the LCMS at a temperature of 20°C

| Test image 1 | Test image 2 | Test image 3 | Test image 4 |

Test image 5	Test image 6	Test image 7	Test image 8
Test image 9	Test image 10	Test image 11	Test image 12
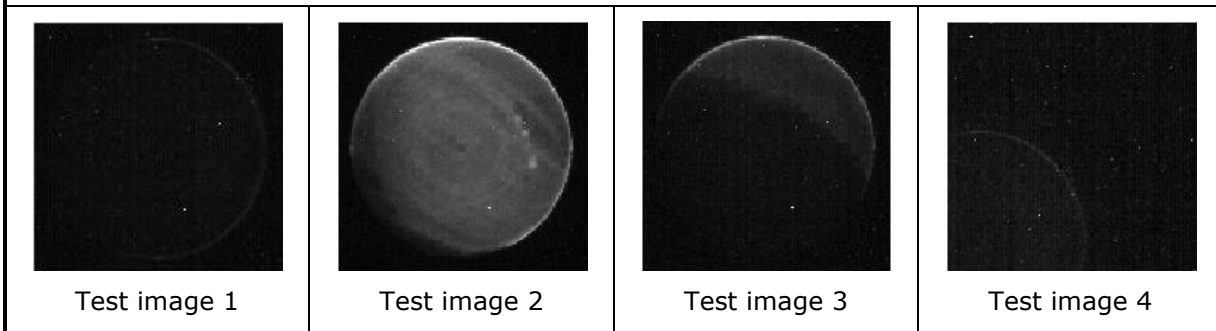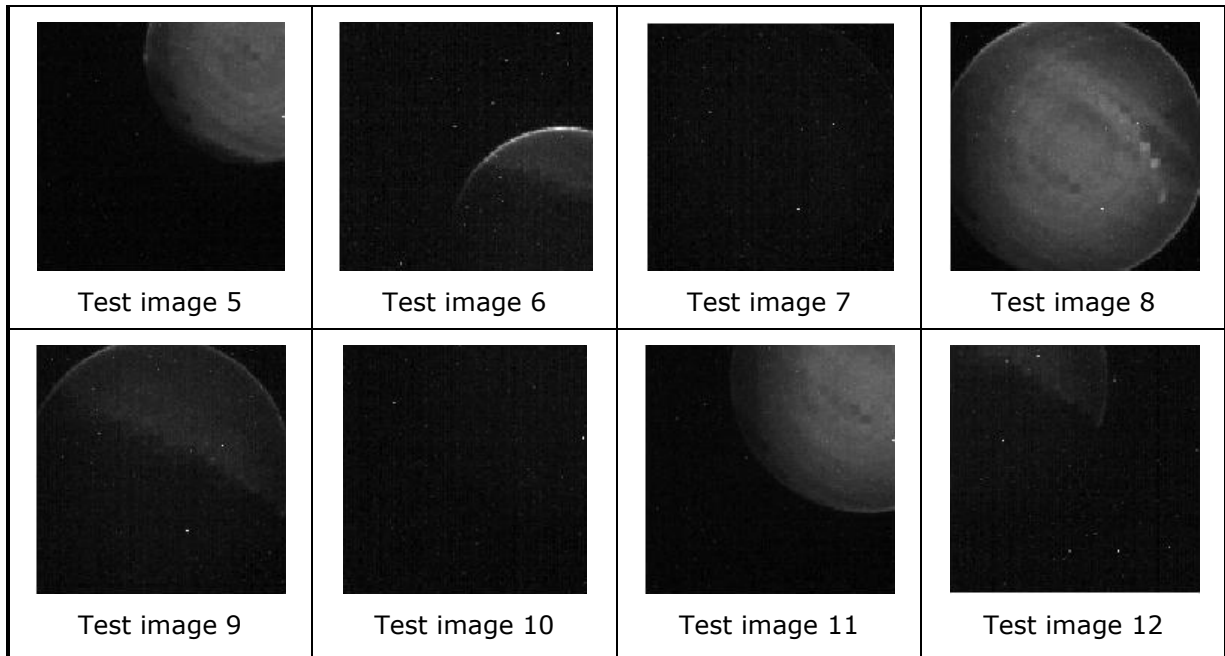
Figure 72: Images acquired at 20°C with the LCMS detector in order to test the earth center finding algorithm under different circumstances.

5.8.4   Test Results for the Algorithm Testing

As shown in Figure 73, the algorithm performed well on images of the airglow taken from a satellite altitude of 45000 km. With exception of the image with minimum airglow signal at night for a sensor temperature of 60°C and an earth that is partially outside of the FOV, the algorithm can successfully determine the earth vector if the image threshold is chosen correctly.

Indeed, earth presence could successfully be detected for all images at all threshold levels for which the earth vector could be determined with an error under 20 pixels. A first step, as shown in Figure 73, is to find the best operating parameters for the algorithm, principally the threshold. Then the breadboard performance can be assessed. A good algorithm performance can be achieved with a threshold level of 50 LSB at 20°C and 40°C, and of 70 LSB at 60°C. The results of the algorithm testing with these parameters are given in TABLE 14.

After fixed pattern noise reduction, we find good agreement between the simulated performance and measured performance on the breadboard.

Test images with the earth completely within the FOV of the detector	Test images with the earth partially outside of the FOV of the detector

Performance of the algorithm at 20°C

Performance of the algorithm at 40°C

Performance of the algorithm at 60°C
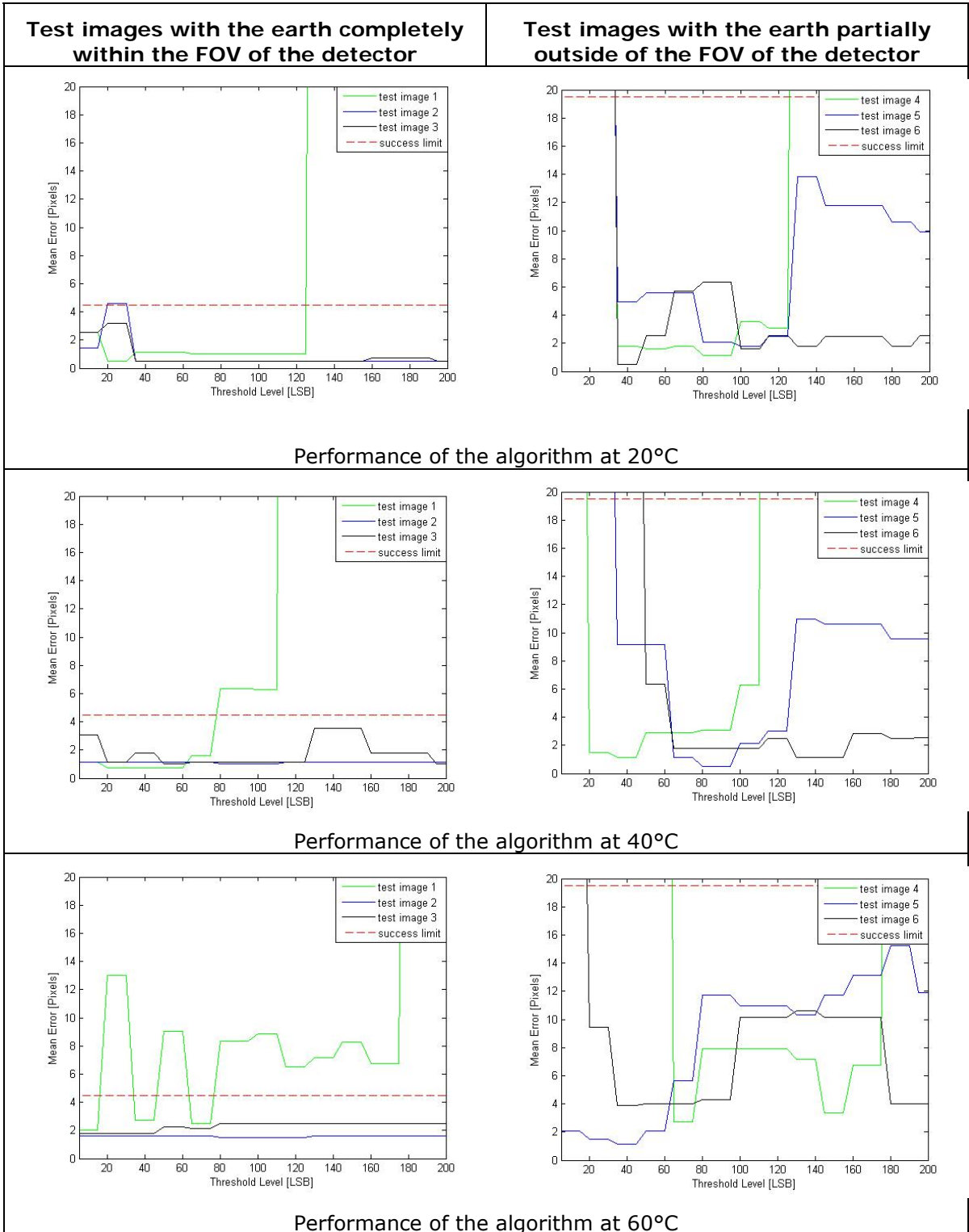
Figure 73: Results of the algorithm testing with the LCMS detector, removing fixed pattern noise, for a satellite altitude of 45000 km. The mean error is plotted vs. the threshold level used in the algorithm, and

Low Cost Earth Sensor based on Oxygen
Airglow – Final Report
ESA Contract #20267/06/NL/JA
Issue: 1   Review: 5
Date: 29/08/08
Page: 72 of 88

the dashed horizontal lines represent the accuracy goal. Successful operation of the algorithm requires having the curves (corresponding to different test images) being below the dashed lien for some value of the threshold level.

The precision of the algorithm is slightly lower if airglow is observed from a satellite altitude of 35000 km. At lower altitude, the airglow signal on a single pixel is weaker and hence more difficult to separate from detector noise. Since the LCMS has a better resolution than the SPAD array[4] (0.13°/pixel instead of 0.16°/pixel), an array of 128 pixels x 128 pixels can not detect the whole earth circumference, even if the earth is centred within its FOV. (Note: we are not taking advantage of the higher resolution of the LCMS here since the system was designed for a 128x128 SPAD array. Overall performance could be improved by redesigning the system for the LCMS detector)

TABLE 14: RESULTS OF THE ALGORITHM TESTING WITH THE LCMS AND A FIXED THRESHOLD FOR THREE TEMPERATURES AND 12 TEST IMAGES

Temperature	Test Image	Earth Presence Flag	Sun Blinding Flag	Error		Test Result	
				[pixel]	[°]	Earth Presence Detection	Earth Vector Determination
20°C	1	1	0	1.1	0.14	Passed	Passed
	2	1	0	0.5	0.06	Passed	Passed
	3	1	0	0.5	0.06	Passed	Passed
	4	1	0	1.6	0.20	Passed	Passed
	5	1	0	5.6	0.71	Passed	Passed
	6	1	0	2.5	0.32	Passed	Passed
	8	1	0	0.7	0.09	Passed	Passed
	9	1	0	> 20	> 2.5	Passed	Failed
	11	1	0	7.1	0.90	Passed	Passed
	12	0	0	> 20	> 2.5	Failed	Failed
40°C	1	1	0	0.7	0.09	Passed	Passed
	2	1	0	1.1	0.14	Passed	Passed
	3	1	0	1	0.13	Passed	Passed
	4	1	0	2.9	0.37	Passed	Passed
	5	1	0	9.2	1.16	Passed	Passed
	6	1	0	6.3	0.80	Passed	Passed
	8	1	0	1.5	0.19	Passed	Passed
	9	0	0	> 20	> 2.5	Failed	Failed
	11	1	0	6.7	0.85	Passed	Passed
	12	0	0	> 20	> 2.5	Failed	Failed
60°C	1	1	0	2.5	0.32	Passed	Passed
	2	1	0	1.6	0.20	Passed	Passed
	3	1	0	2.1	0.27	Passed	Passed
	4	1	0	2.7	0.34	Passed	Passed

[4] The algorithm has been designed for a SPAD-array of 128 pixels x 128 pixels.

5	1	0	5.7	0.72	Passed	Passed
6	1	0	4.0	0.51	Passed	Passed
8	1	0	1.1	0.14	Passed	Passed
9	1	0	> 20	> 2.5	Failed	Failed
11	1	0	7.1	0.90	Passed	Passed
12	0	0	> 20	> 2.5	Failed	Failed

5.8.5   Conclusion Algorithm Testing

The earth vector determination algorithm performed well on the targeted test images captured with the LCMS. Indeed, even without correction for Fixed Pattern Noise (FPN), the targeted precision of 4.5 pixels with images completely within the FOV of the detector, and of 19.5 pixels for images with the earth partially outside of the FOV can be guaranteed for **all** images taken from a satellite altitude of 45000 km, except for the minimum airglow signal at a detector temperature of 60°C. This is an acceptable restriction, since the ES should not have a high temperature when observing nightglow.

A simple solution to increase the performance of the earth vector determination algorithm is to increase the FOV of the LCMS by taking into account the response of a bigger part of the array (e.g. 256 pixels x 256 pixels). We found it was necessary to correct for FPN in order for the observed performance on the breadboard to agree with the simulated performance. FPN reduction can easily be implemented and allows significantly increasing the robustness and the performance of the earth presence detection algorithm and the earth vector determination algorithm.

Low Cost Earth Sensor based on Oxygen
Airglow – Final Report
ESA Contract #20267/06/NL/JA
Issue: 1   Review: 5
Date: 29/08/08
Page: 74 of 88

6 BUDGETS

The following mass, power and run time budgets apply, unless explicitly stated otherwise, to both types of detector considered: LCMS or SPAD array.

6.1 Mass Budgets

TABLE 15: MASS BUDGET FOR A SINGLE "TUBE" OF THE AIRES INSTRUMENT

Parameter	Quantity	Mass per Unit
Support Structure for Focusing Optics	1	30 g
Baffle	1	115 g
Focusing Optics + Filter	1	15 g
Detector Board	1	10 g
Margin (5%)	1	10 g
Total mass		180 g

TABLE 16: MASS BUDGET FOR THE AIRES INSTRUMENT FOR GEO APPLICATIONS

Parameter	Quantity	Mass per Unit
Tube	1	180 g
Housing and Shielding	1	385 g
Mainboard	1	105 g
DC/DC-Board	1	85 g
Connectors and Cables		50 g
Margin (5%)		40 g
Total mass		845 g

TABLE 17: MASS BUDGET FOR THE AIRES INSTRUMENT FOR LEO APPLICATIONS

Parameter	Quantity	Mass per Unit
Tube	3	540 g
Housing and Shielding	1	760 g
Mainboard (Including DC/DC-Converter)	1	200 g
Connectors and Cables		100 g
Margin (5%)		80 g
Total mass		1680 g

Low Cost Earth Sensor based on Oxygen
Airglow – Final Report
ESA Contract #20267/06/NL/JA
Issue: 1   Review: 5
Date: 29/08/08
Page: 75 of 88

6.2   Power Budget/Memory and Run Time Estimation

TABLE 18: POWER BUDGET FOR THE AIRES INSTRUMENT

Element	Power Consumption [W]	Duty Cycle [%]	Mean Power Consumption [W]
Microprocessor	1	100	1
ROM 8k x 8	0.075	0	0
RAM 512k x 8	0.65	20	0.13
Detector	0.23	50	0.12
FPGA[5]	1.23	50	0.62
Serial Data Converter	0.2	100	0.2
Oscillator 20 MHz	0.1	100	0.1
Other Components	0.5	100	0.5
DC/DC Converter 100V to 5V		100	0.6
Margin (20%)			0.7
Total			4.0

TABLE 19: ESTIMATION OF THE MEMORY AND THE RUN TIME REQUIRED FOR THE ALGORITHM

Process	Memmory need [kbits]	Run time [ms]
Image store (pre-binarisation),	262.1	-
Image store (post binarisation)	16.4	0.4
Sun Blinding Recognition	0.1	1.4
Erosion	16.4	17.4
Edge detection filter	0.2	20.6
Hough algorithm	25.2	398.8
Earth Presence Detection	0.1	0.3
Total	320.6	465.9

---

[5] Required if SPADs are used as detector.

6.3   Expected Performance

The output accuracy of the earth vector determination algorithm is equal to the FOV of one pixel (0.16°). However, supplemental errors in the measurements and the calculations will be introduced by different factors. The worst case error has been determined according to

$$e_{worst\_case} = \sum_i e_i \qquad \text{(where } e_i \text{ is the maximum expected error introduced by the source } i\text{)}$$

TABLE 20: EXPECTED PERFORMANCE AND ERROR SOURCES FOR THE ES INSTRUMENT

Error sources (i)	Maximum Expected Error (e_i)
Optics aberrations and correction for distortion	$1 \cdot FOV_{pixel}$
Algorithm	$1 \cdot FOV_{pixel}$
Smear (pointing stability during measurements)	$1 \cdot FOV_{pixel}$ (LEO) 0.05° (GEO)
Angular incertitude of the airglow	1° (LEO) 0° (GEO)
Oblateness of the earth	1° (LEO) 0° (GEO)
Worst Case Error	$2° + 3 \cdot FOV_{pixel}$ (LEO) $0.05° + 2 \cdot FOV_{pixel}$ (GEO)

For a FOV of 0.16°/pixel, this gives a maximum total error of 2.5 ° in LEO and 0.4 ° in GEO which is perfectly admissible since the targeted XY output accuracy is 5° for LEO and 0.6° for GEO.

7 DEVELOPMENT PLAN

The development plan (DDVP) plan describes the strategy for design, selection of components, manufacturing and verification, which shall lead to a Flight Model (FM) of the earth sensor. This DDVP presents the model philosophy, the engineering logic and verification plan which have to be carried out in the different development phases in order to reach the scope.

Moreover planning and preliminary cost estimate up to EQM Test Review and FM design update are provided.

7.1 Product Tree and Specification Tree

The schematic product tree given in Figure 74 can be assigned to the earth sensor.
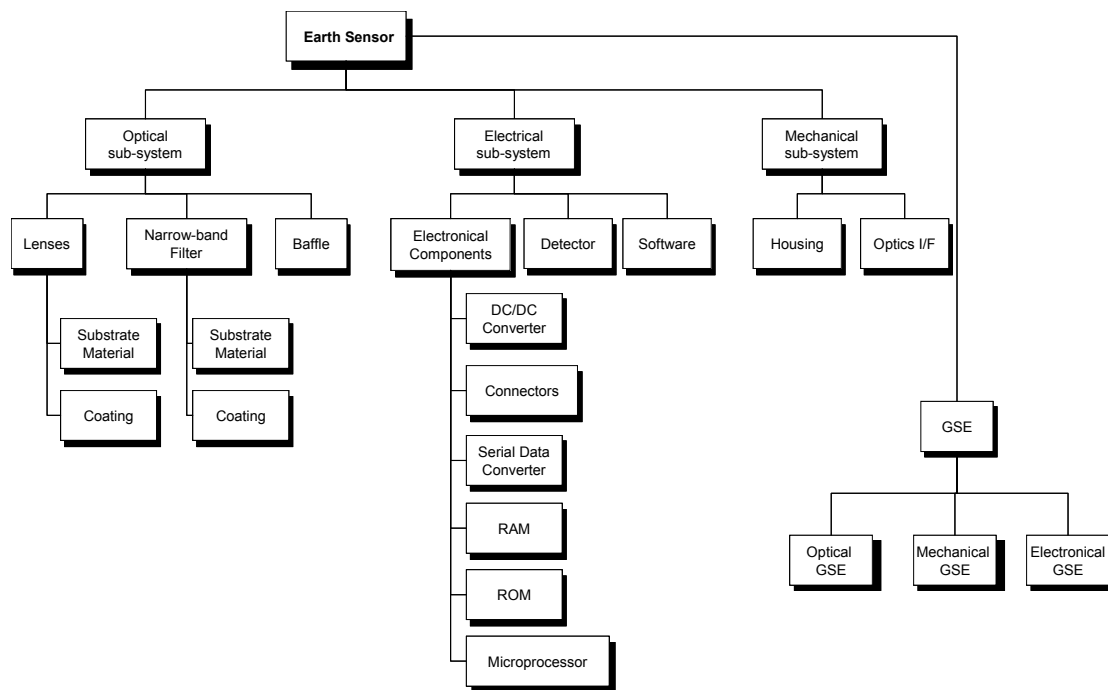
Figure 74: Preliminary ES product tree.

7.2 Design and Development Philosophy

7.2.1 Model Philosophy

The first model for the ES instrument shall be a breadboard (BB) for a preliminary testing of the opto-mechanical functionality. In parallel to the BB activities, an Engineering Model (EM) for the

electrical sub-system is planned for the validation of the electronics layout and the electrical interface and resources. Furthermore, the EM will include activities for the implementation of the detector and the software where it is necessary. For both the BB and the EM, off-the-shelf components shall be used.

After that, an Engineering and Qualification Model (EQM) for the qualification of the optical and electrical sub-systems will be built.

Materials and processes used for the design have thus to fully reflect the flight design. A prototype flight model (PFM) will first be developed, followed by the final Flight Model (FM).

7.2.1.1   Definition of Development Phases
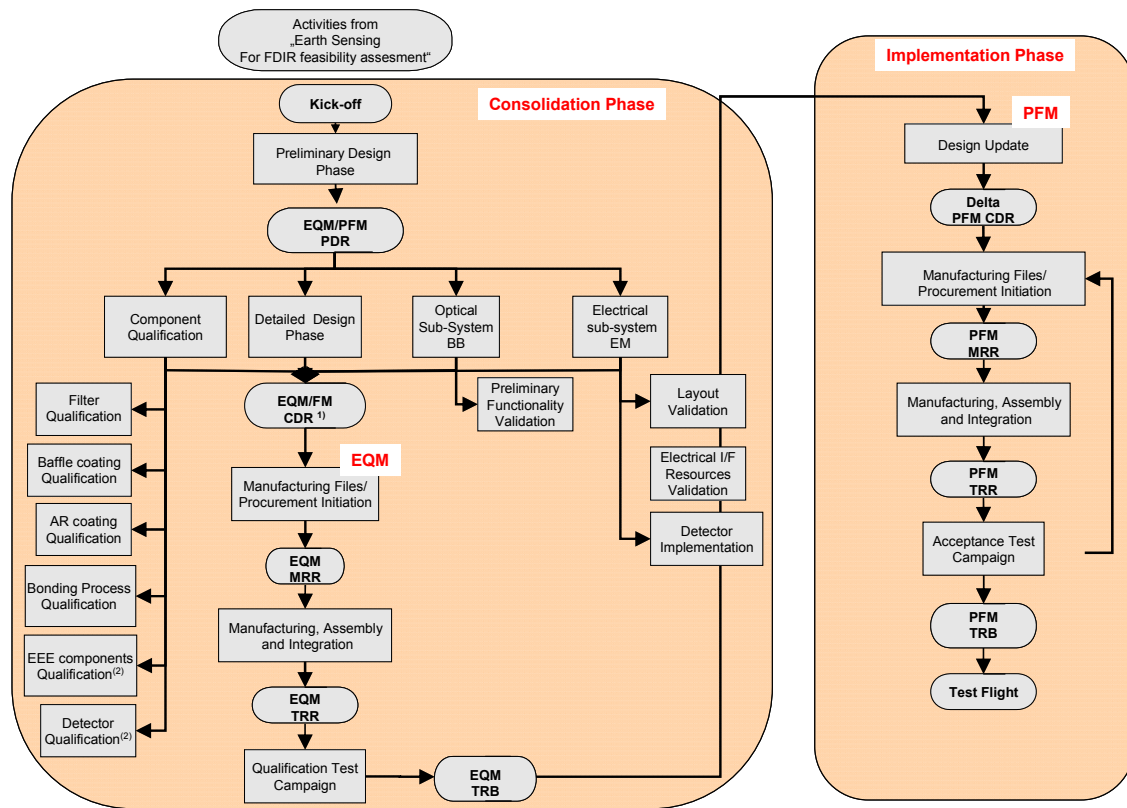
Figure 75: Development phases of the earth sensor. 1) If needed, the procurement of long-lead items should be initiated prior to this step. 2) Qualification campaign for these components is not foreseen in this DDVP but included as a risk factor.

The phases for the development of the ES are depicted in Table 20. These are the general development phases and will be detailed in the subsequent sections. Potential loops have to be avoided. The exact time schedule is detailed in section 7.6.1.

The activities defined in the model philosophy can be divided in two different phases which can be separately funded. A consolidation phase will include the activities planned for the BB, EM and EQM. After the successful development and qualification of the EQM, an Implementation Phase shall follow for the development of the prototype (PFM) and the Flight Model.

7.2.1.2 Development Milestones and Reviews

Reviews of the ES program should take place throughout the DDV life cycle. The format and formality of the reviews still has to be defined. However, the reviews should include

- Design Review (PDR, CDR)

- Manufacturing Readiness Review (MRR)

- Test Readiness Review (TRR)

- Test Review Board (TRB)

- Delivery Review Board (DRB)

Independently of the review format, minutes or a report detailing outstanding actions, RIDS and review status will be made for each review.

7.2.2   Engineering Logic

7.2.2.1 Architecture

The system architecture will be defined after an assessment of the customer requirements and other stakeholder requirements such as ESA requirements or OSZ in-house standards. As soon as the defined system architecture can satisfy all requirements, the sub-unit requirements will be defined.

7.2.2.2 Design

The preliminary design of the opto-mechanical sub-unit will be compared to the specifications and the sub-unit design will be started as soon as the requirements are satisfied. The detailed design includes breadboarding activities for the optical sub-system and an engineering model for the validation of electronics layout. The qualification on component level will be performed in parallel to this phase.

A successful conclusion of the detailed design phase will lead to the manufacturing, assembly and integration (MAI) of the EQM.

The EQM will undergo a proto-qualification test program at unit level, which is completed with the formal verification of the requirements.

7.2.2.3 Verification

With only a few possible exceptions, all requirements verification for the opto-mechanical and electrical sub-units will be performed on unit level using the EQ model.

At component level, the following components will undergo a qualification program versus radiation and stability in thermal environment:

- Narrow-band filter

- AR coating

- Baffle coating

- Bonding Process (where necessary)

7.2.3   Bread-boarding

For the opto-mechanical sub-unit, a breadboard is foreseen. The tests comprise thermal and mechanical tests at unit level. If the coatings are not space qualified yet, a radiation test at component level is also planned.

7.2.4   Development Phases

7.2.4.1 Description of Phases and reviews

The development of the ES will be grouped in the phases as given in Table 20.

TABLE 21: DEVELOPMENT PHASES

Preliminary Design Phase	• Requirement analysis • Assessment of available documents • Architectural design of the ES • Establishment of budgets • Interface definition • Preliminary design of sub-units • Identification of LLI • Procurement Specification for optical subassembly
	EQM/PFM PDR
Detailed Design Phase	• Release of LLI procurement • Qualification process at component level • Detailed design and analysis of sub-units • Bread-boarding activities • EM activities • Update of design according to results of bread-board and to expected tolerances of manufacturers • Generation of procurement specifications • Procurement of long-lead items if approved by the customer
	EQM/PFM CDR
	• Generation of manufacturing files and procurement
	EQM MRR
	• Manufacturing, procurement, assembly and integration of the system
	EQM TRR
	• Qualification test campaign of instrument
	EQM TRB
	• Update FM design according to results of qualification test campaign

PFM Delta CDR
• Manufacturing, procurement, assembly of FM
PFM TRR
• Acceptance test campaign
PFM TRB
• End Item Data Package
PFM DRB

7.3   Qualification Program

The verification programme will be done at unit level for the opto-mechanical sub-system. The filter and the anti-reflection coating will be qualified at component level for radiation and environment tests. The same will be applied on EEE components if needed. Concerning EEE, the strategy will be to use as far as possible already qualified components.

Note: For the filter, the term 'qualification' does not refer to a 'full scale' qualification campaign as foreseen in the ESCC specifications, but rather to a 'lot acceptance test' or a 'validation for the application'.

7.4   Qualification Status

The qualification matrix in Table 21 states the qualification status of the components and processes. The qualification programme is made under the assumption that space qualified electronics components are available. This assumption can be confirmed only at PDR.

TABLE 22: QUALIFICATION MATRIX FOR THE EARTH SENSOR.

Process or Component	Location	Supplier/ Subcontractor	Delta Qualification
Baffle coating	Optical sub-system	e.g.: Thin Film Physics	Qualification to be foreseen
Narrow-band Filter	Optical sub-system	e.g.: Barr Ass, Tafelmeier	Qualification to be foreseen
AR coating	Optical sub-system	e.g.: FISBA	Qualification to be foreseen
Bonding process	TBD	e.g.: OSZ	Qualification to be foreseen
EEE components	Electrical sub-system	e.g.: Varius	No Qualification is foreseen
Detector	Electrical sub-system	e.g.: Perkin Elmer	Qualification not to be excluded

The companies listed under Supplier/Subcontractor are examples of possible suppliers and are not to be considered as a final statement.

7.5   Manufacturing

7.5.1   AIV

The AIV-flow is given in the following chart (Figure 76).
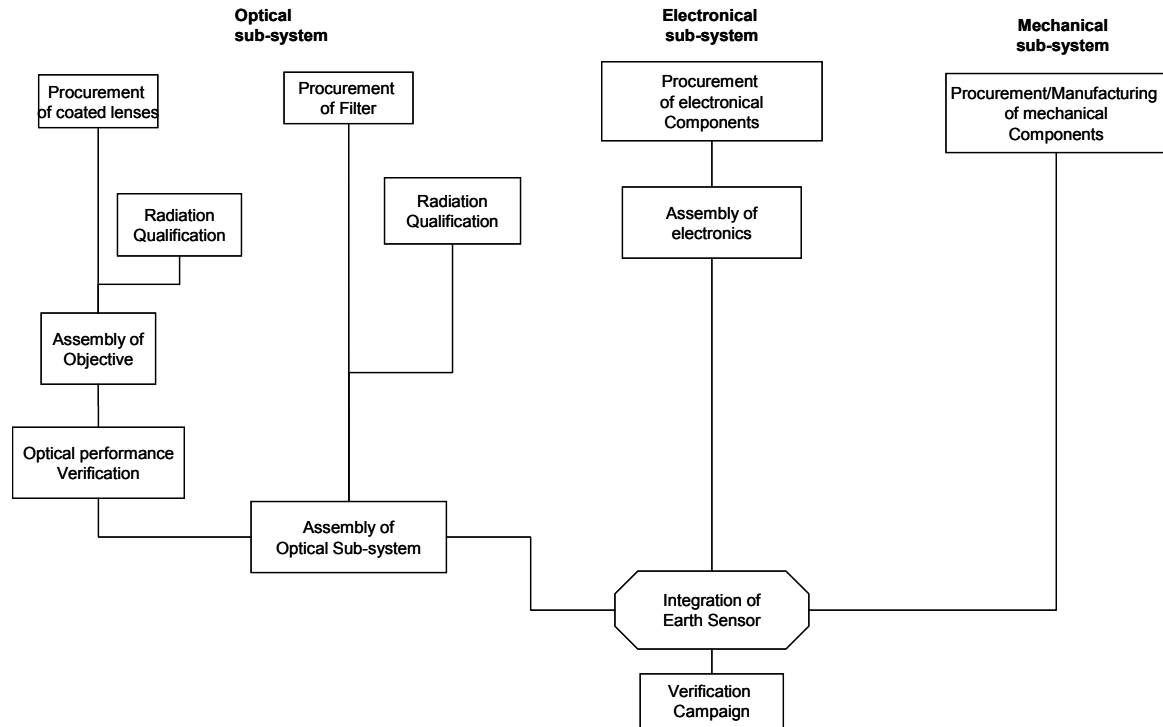

Figure 76: AIV Flow.

7.6   Schedule

7.6.1   Overall Schedule Presentation

A schematic representation of the time schedule for the earth sensor is shown in the following figure. It results in a work of 24 months.
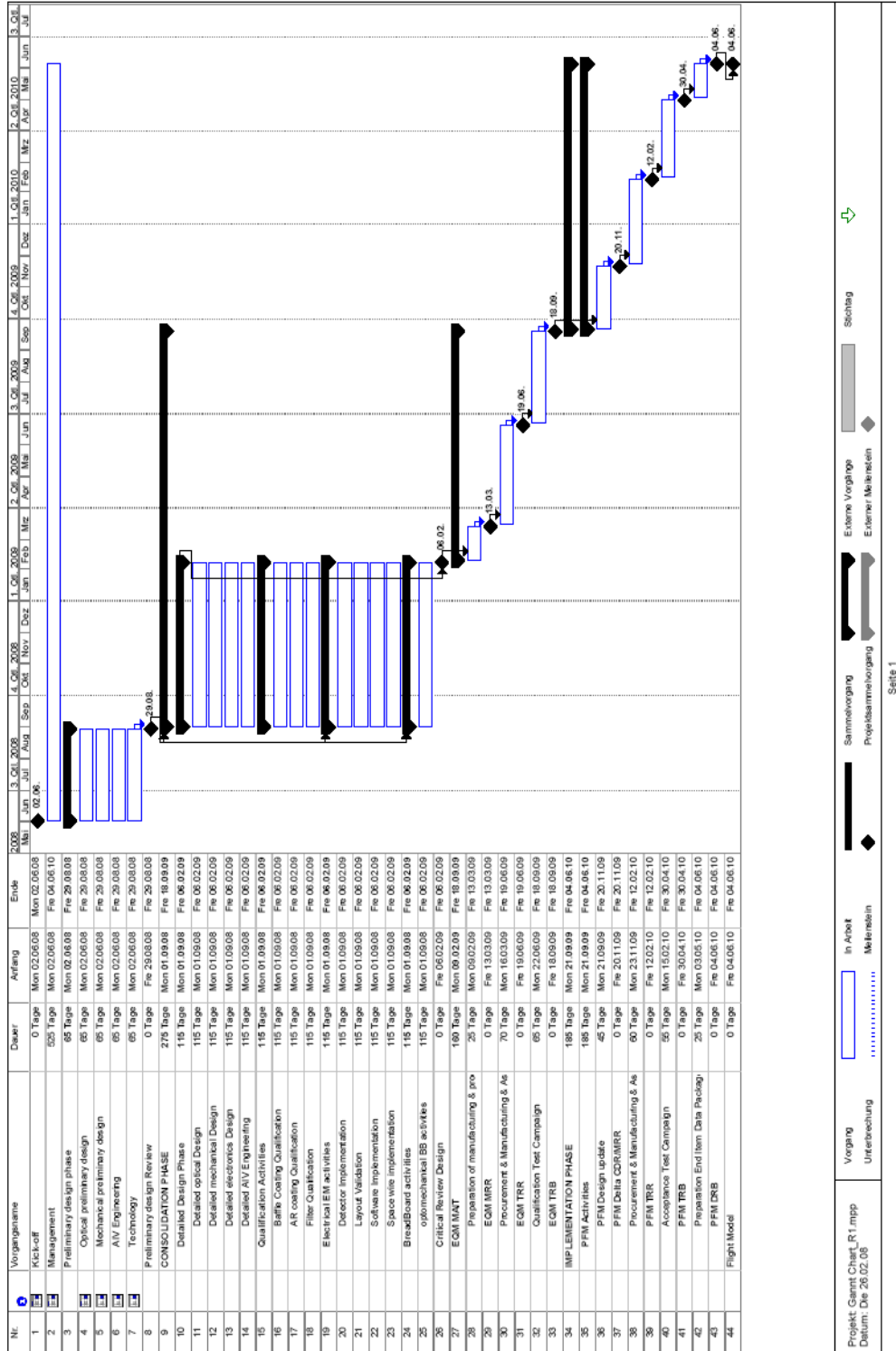
Nr.	●	Vorgangsname	Dauer	Anfang	Ende
1		Kick-off	0 Tage	Mon 02.06.08	Mon 02.06.08
2		Management	525 Tage	Mon 02.06.08	Fre 04.06.10
3		Preliminary design phase	65 Tage	Mon 02.06.08	Fre 29.08.08
4		Optical preliminary design	65 Tage	Mon 02.06.08	Fre 29.08.08
5		Mechanical preliminary design	65 Tage	Mon 02.06.08	Fre 29.08.08
6		AIV Engineering	65 Tage	Mon 02.06.08	Fre 29.08.08
7		Technology	65 Tage	Mon 02.06.08	Fre 29.08.08
8		Preliminary design Review	0 Tage	Fre 29.08.08	Fre 29.08.08
9		CONSOLIDATION PHASE	275 Tage	Mon 01.09.08	Fre 18.09.09
10		Detailed Design Phase	115 Tage	Mon 01.09.08	Fre 06.02.09
11		Detailed optical Design	115 Tage	Mon 01.09.08	Fre 06.02.09
12		Detailed mechanical Design	115 Tage	Mon 01.09.08	Fre 06.02.09
13		Detailed electronics Design	115 Tage	Mon 01.09.08	Fre 06.02.09
14		Detailed AIV Engineering	115 Tage	Mon 01.09.08	Fre 06.02.09
15		Qualification Activities	115 Tage	Mon 01.09.08	Fre 06.02.09
16		Baffle Coating Qualification	115 Tage	Mon 01.09.08	Fre 06.02.09
17		AR coating Qualification	115 Tage	Mon 01.09.08	Fre 06.02.09
18		Filter Qualification	115 Tage	Mon 01.09.08	Fre 06.02.09
19		Electrical EM activities	115 Tage	Mon 01.09.08	Fre 06.02.09
20		Detector Implementation	115 Tage	Mon 01.09.08	Fre 06.02.09
21		Layout Validation	115 Tage	Mon 01.09.08	Fre 06.02.09
22		Software Implementation	115 Tage	Mon 01.09.08	Fre 06.02.09
23		Space wire implementation	115 Tage	Mon 01.09.08	Fre 06.02.09
24		BreadBoard activities	115 Tage	Mon 01.09.08	Fre 06.02.09
25		opto/mechanical BB activities	115 Tage	Mon 01.09.08	Fre 06.02.09
26		Critical Review Design	0 Tage	Fre 06.02.09	Fre 06.02.09
27		EQM MAIT	160 Tage	Mon 09.02.09	Fre 18.09.09
28		Preparation of manufacturing & pro	25 Tage	Mon 09.02.09	Fre 13.03.09
29		EQM MRR	0 Tage	Fre 13.03.09	Fre 13.03.09
30		Procurement & Manufacturing & As	70 Tage	Mon 16.03.09	Fre 19.06.09
31		EQM TRR	0 Tage	Fre 19.06.09	Fre 19.06.09
32		Qualification Test Campaign	65 Tage	Mon 22.06.09	Fre 18.09.09
33		EQM TRB	0 Tage	Fre 18.09.09	Fre 18.09.09
34		IMPLEMENTATION PHASE	185 Tage	Mon 21.09.09	Fre 04.06.10
35		PFM Activities	185 Tage	Mon 21.09.09	Fre 04.06.10
36		PFM Design update	45 Tage	Mon 21.09.09	Fre 20.11.09
37		PFM Delta CDR/MRR	0 Tage	Fre 20.11.09	Fre 20.11.09
38		Procurement & Manufacturing & As	60 Tage	Mon 23.11.09	Fre 12.02.10
39		PFM TRR	0 Tage	Fre 12.02.10	Fre 12.02.10
40		Acceptance Test Campaign	55 Tage	Mon 15.02.10	Fre 30.04.10
41		PFM TRB	0 Tage	Fre 30.04.10	Fre 30.04.10
42		Preparation End Item Data Package	25 Tage	Mon 03.05.10	Fre 04.06.10
43		PFM DRB	0 Tage	Fre 04.06.10	Fre 04.06.10
44		Flight Model	0 Tage	Fre 04.06.10	Fre 04.06.10

Projekt: Gantt Chart_R1.mpp
Datum: Die 26.02.08

Vorgang	In Arbeit	Externe Vorgänge	Stichtag
Unterbrechung	Meilenstein	Externer Meilenstein	
Sammelvorgang	Projektsammelvorgang		

Seite 1

Low Cost Earth Sensor based on Oxygen
Airglow – Final Report
ESA Contract #20267/06/NL/JA
Issue: 1   Review: 5
Date: 29/08/08
Page: 85 of 88

7.6.2   Key Milestones and Delivery

Key milestones are listed in Table 23.

TABLE 23: KEY MILESTONES

Event	Milestone
Kick-off	T0
PDR	T0+3 M
CDR	PDR+5 M
EQM MRR I	CDR+1 M
EQM TRR	MRR +3 M
EQM TRB	TRR+ 3 M
PFM ΔCDR	EQM TRB + 2 M
PFM TRR	FM ΔCDR + 3M
PFM TRB	TRR +3M
PFM DRR	TRR + 1M

7.7   Verification Plan

7.7.1   General Overview

The proposed verification tests for the Earth Sensor are listed below.

- Assembly tests (inspection and verification of sub-assembly dimensions)

- Optical performances (verification of optical transmission and imaging)

- Vibration tests

- Thermal cycling

7.7.2   Verification Logic

7.7.2.1   Test Sequence

The general test sequence is given in Figure 77. The tests will be detailed until the TRR. A draft version of the test plan will be provided for CDR. Hence, test specifications and test procedures will be available at that time.

All environmental tests such as vibration tests, shock tests, thermal cycling tests and thermal-vacuum test will be encompassed by a performance check of the system.
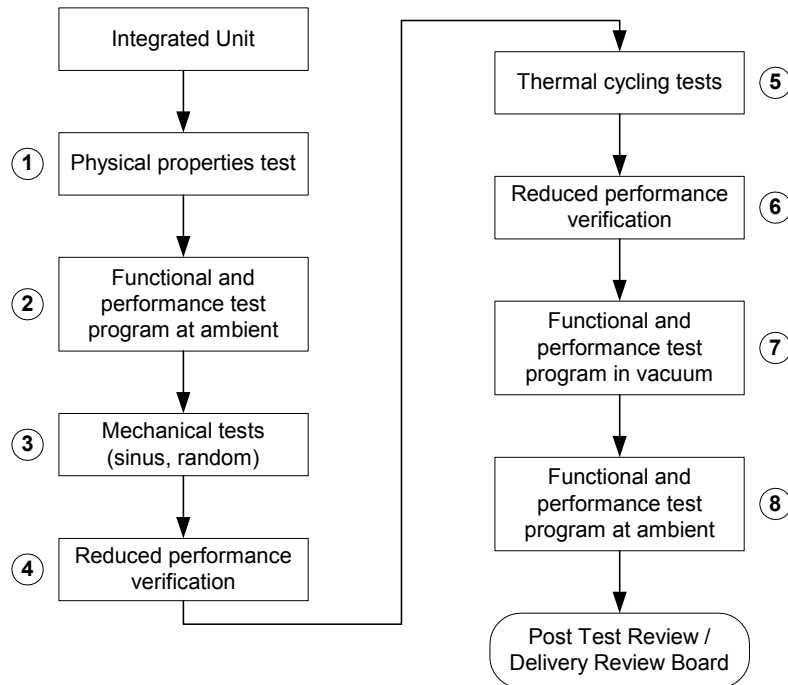
Figure 77: Test sequence.

7.7.3   Verification

7.7.3.1   Mechanical and Thermal

Logic and Critical Parameters

The mechanical and thermal verification will be performed according a test sequence.

Tests

Vibration tests will be split into sinusoidal and random vibration tests. These tests will be performed under ambient conditions. The test plan and the test procedure will define how the cleanliness requirements will be met.

Thermal vacuum and thermal cycling tests will be combined in the vacuum chamber. These tests will be performed according to the conditions given there.

7.7.3.2   Electrical

Logic and Critical Parameters

The hardware for thermal control will be tested for correct functional performance. No critical parameters are expected.

Development Model Used for Verification

Verification of electrical parameters will be undertaken on the EM.

Tests

The proper functioning of the heaters and temperature sensors will be verified in the course of the overall unit tests.

7.8   Cost estimates

The cost is based on 24 months schedule and on the assumptions that the technical information from the present earth sensor study is going to be available for the continuation of the activities.

The costs for the consolidation phase (which includes BB, EM and EQM) are estimated to be about 2'000'000 Euros and for the implementation phase about 720'000 Euros.

The present knowledge of the detailed design of the system is not sufficient to give an accurate estimation of the recurring costs. On the basis of the Earth Sensor layout for GEO application, a range for the recurring costs has been assessed.

Depending mainly on the layout of the electronics, which will have to be design not only for performances but as well for cost optimization, the RC of a unit might varies between about 100 Keuro and 250 Keuro. The cost drivers are components like FPGA, ASIC, possible need of memory. Their use shall be minimized as far as possible.

The costs could be further reduced depending on the number of items and on the amount of the procurement lots.

8 CONCLUSIONS

This project has demonstrated the feasibility of a low-cost compact Earth sensor based on imaging oxygen airglow, allowing 0.4° accuracy from GEO under any illumination condition.

In both night-time and daytime there is continuous emission at 762 nm due to oxygen recombination at altitudes of 80 to 100 km. Low-noise active pixel sensors (APS) or low-light detector based on arrays of single photon avalanche diodes (SPAD) enable the ES to operate at night and day, over a wide temperature range, with a very compact optical system (aperture of 8 mm, focal length of 11 mm) and no scanning elements. A modular design allows designing similar instruments using the same wavelength band, the same detector technology, the same optics, the same power and data interfaces and similar algorithms for GEO and LEO applications, thus reducing the development cost.

We have developed an Earth appearance model at 762 nm, which was used as input for the mechanical, optical and electric design of the Earth Sensor (conceptual design). In order to achieve a low-cost solution, simplicity and reduction of part count was a driving factor in the design trade-offs. Total mass for the GEO design is 845 g with a mean power consumption of 4 W. Algorithms were developed to determine the vector to the Earth from the images. A breadboard was built to display a simulated picture of the Earth under varying conditions, image those pictures at different temperatures with a radiation tolerant APS (LCMS), and verify the correct operation of the algorithms.

The earth vector determination algorithm performed well on the targeted test images captured with the LCMS. The targeted precision of 0.6° for images completely within the FOV of the detector, and of 3° for images with the earth partially outside of the FOV can be guaranteed for all images taken from a satellite altitude of 45000 km, except for the minimum airglow signal at a detector temperature of 60°C.

In addition to the conceptual design and breadboard level demonstration of key technologies, a novel detector chip was designed and fabricated: a radiation-tolerant array of single photon avalanche photodiodes (SPAD) build using conventional 0.35 μm CMOS technology. The chip was tested under proton and gamma irradiation, and operated with only minor changes in dark current after 30 krad TID.

Having shown the feasibility of such an Earth Sensor, this work concluded with a development plan to lead to a flight model. Suggestions for improvement include the use of the LCMS detector, which is already space qualified, and a minor redesign of the optical system to make better use full array (e.g. 256 pixels x 256 pixels).